
FİZİKTE İLERİ ARAŞTIRMALAR

Editör: Dr.Öğr.Üyesi Murat Metehan TÜRKOĞLU

yaz
yayınları

Fizikte İleri Araştırmalar

Editör

Dr. Öğr. Üyesi Murat Metehan TÜRKOĞLU

yaz
yayınları

2024

Fizikte İleri Araştırmalar

Editör: Dr. Öğr. Üyesi Murat Metehan TÜRKOĞLU

© YAZ Yayınları

Bu kitabın her türlü yayın hakkı Yaz Yayınları'na aittir, tüm hakları saklıdır. Kitabın tamamı ya da bir kısmı 5846 sayılı Kanun'un hükümlerine göre, kitabı yayınlayan firmannın önceden izni alınmaksızın elektronik, mekanik, fotokopi ya da herhangi bir kayıt sistemiyle çoğaltılamaz, yayınlanamaz, depolanamaz.

E_ISBN 978-625-6171-36-7

Aralık 2024 – Afyonkarahisar

Dizgi/Mizanpaj: YAZ Yayınları

Kapak Tasarım: YAZ Yayınları

YAZ Yayınları. Yayıncı Sertifika No: 73086

M.İhtisas OSB Mah. 4A Cad. No:3/3
İscehisar/AFYONKARAHİSAR

www.yazyayinlari.com

yazyayinlari@gmail.com

info@yazyayinlari.com

İÇİNDEKİLER

A Preliminary Study On Uncertainties In Fading Studies.....1

Tamer DOĞAN

**A View Of Coherent Elastic Neutrino-Nucleus Scattering And
Beyond Standard Model: The New Light Mediators17**

Mehmet DEMİRÇİ, M. Fauzi MUSTAMİN

**Nörodejeneratif Hastalıklarda Kan Örneklerinin Fourier
Dönüşüm Infrared (FTIR) Spektroskopisi İle İncelenmesi37**

Çisem ALTUNAYAR ÜNSALAN

Random Lazerler55

Ekrem YARTAŞI

**Recent Developments In The Application Areas Of Low
Temperature Superconductor MgB₂71**

Özge ERDEM

**Bulk Type Magnetic Field Production Methods And
Applications89**

Murat ABDİOĞLU, Ufuk Kemal ÖZTÜRK

**Coil Type Magnetic Field Production Methods And
Applications111**

Ufuk Kemal ÖZTÜRK, Murat ABDİOĞLU

**Steroid İçeren Bir Bileşigin Moleküler Modelleme
Çalışması..... 125**

Gonca ÖZDEMİR TARI

"Bu kitapta yer alan bölümlerde kullanılan kaynakların, görüşlerin, bulguların, sonuçların, tablo, şekil, resim ve her türlü içeriğin sorumluluğu yazar veya yazarlarına ait olup ulusal ve uluslararası telif haklarına konu olabilecek mali ve hukuki sorumluluk da yazarlara aittir."

A PRELIMINARY STUDY ON UNCERTAINTIES IN FADING STUDIES

Tamer DOGAN¹

1. INTRODUCTION

Electromagnetic radiation resulting from the phenomenon of luminescence, an umbrella term used for Electromagnetic radiation resulting from the phenomenon of luminescence, an umbrella term used for objects that emit light upon energetic excitation without heating, can be classified into two different forms, fluorescence and phosphorescence, depending on the characteristic time (τ_c) between excitation and light release (McKeever, 1985). The technique known as thermoluminescence (TL) is broadly used in geology, mineralogy, and the dating of anthropological and archaeological samples. It measures the luminescence intensity of a sample as a function of temperature when exposed to UV, X-ray, γ -ray, or electron beam radiation (Abraham et al., 2018).

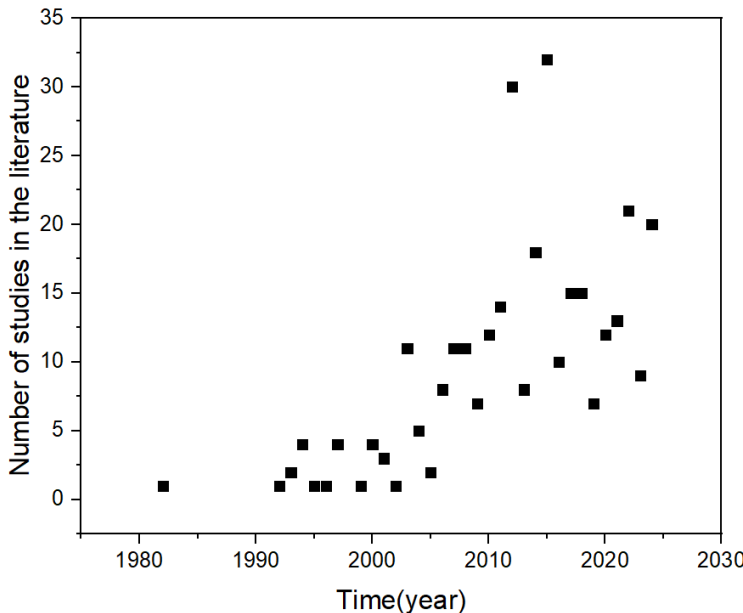
In the literature, in order to evaluate whether a material is dosimetric in TL studies, a judgment can be reached by evaluating the results of dose response, heating rate, reusability and fading studies.

Dosimetric phosphors exposed to radiation exhibit a reduction in TL intensity even at room temperature after being stored in a non-irradiated environment. This phenomenon, commonly known as "fading," results from the gradual depletion of trapped charge carriers over time.

In this study, a detailed historical background on the terms fading and anomalous fading will be organized and presented to the readers. Although this issue has been widely covered in the literature (Figure 1), there is still debate on the uncertainties.

Figure 1. Number of fading studies in the literature by years (based on the number of articles published in Web of Science)

¹ Assoc.Prof.Dr.Tamer Dogan, Çukurova University, Vocational School of Imamoglu, Department of Computer Technologies, tdogan@cu.edu.tr, ORCID: 0000-0002-0633-8470.



2. THEORETICAL FUNDAMENTALS OF FADING AND ANOMALOUS FADING

The first work that is thought to have laid the foundation for understanding anomalous fading was the work carried out by Hoogenstraaten in 1958, where he observed thermally independent fading of TL in ZnS:Cu,Co and demonstrated loss of trapped charge even at low temperatures. When the charge carriers are released from traps more quickly than anticipated in TL investigations, a phenomenon known as "anomalous fading" occurs. This can cause problems for TL dating. This quick fading might make estimated ages underestimate the actual age, particularly when dating volcanic lava. Without subsequent dating studies, it was difficult to detect the gradual decrease in luminescence following the initial rapid signal loss. Since charge carriers escape by tunneling rather than heat activation process, the phenomena has been attributed to quantum tunneling mechanisms (Wintle, 1977).

The first paper that aimed to establish a common principle linking the time dependence of the decay of luminescence in a large range of materials was written by Jonscher and de Polignac (1984). They noted that upon excitation, an electron trap in a defect usually undergoes a power-law decay; where $I \propto t^k$ as the density; and k typically varied

between 1 and 1.5, but can also vary between less than 1 and 2, but they did not provide a precise mechanism. Non-exponential decays such as retrapping during optical stimulation of electrons (McKeever et al., 1997) cannot be explained by their proposed extended power-law decay. Huntley (2006) stated that the tunneling process of trapped electrons as time progresses affects the intensity of luminescence depending on the energy distribution of the traps and the distance to the recombination centers. Luminescence intensity is proportional to the tunneling rate of trapped electrons, which decreases over time and is expressed as $I \propto t^k$, where k typically ranges from 1 to 1.5.

During the observation of the TL signal following irradiation, considerable signal fading takes place when the trap depth E is relatively small. As a result, a TL curve with a peak at 200-250°C (which supports $E > kT$) is more desirable for users to utilize the detector in dosimetry applications (McKeever, 1985).

While studying the rapid energy loss, it was realized that charge carriers escape from the traps through quantum tunneling instead of classical thermal processes. Instead of the slow release predicted by thermal activation, this mechanism led to faster decay of luminescence. In the first 12-17 days the energy decreases rapidly (about 50%), then a slowdown of the signal occurs up to 5 times the initial time (about 15-20%). This process exhibited a similar behavior in all samples, regardless of dose, and can be fitted to a general mathematical formula as follows:

$$Y = a + bx + c\sqrt{x} + dF(x)$$

where Y is the TL signal's intensity, x is the post-irradiation time, $F(x)$ is a time-dependent function and a , b , c and d are the constants of the mathematical function. It was observed that the decay curve in this case offers a good approximation by first-order kinetic equations (McKeever 1985).

Quantum tunneling of charges from deep traps to local recombination centers is the established hypothesis for anomalous TL fading. Templer created a model in 1986 that allowed charge recombination via an excited state shared by a luminescence center and a trap. This concept was tested for anomalous fading in pumice and zirconium as a function of temperature and time. For naturally occurring minerals that exhibit anomalous fading, their anomalies are typical of TL due to the continuity of their nearby traps. It is rarely observed in

luminescence measurements of an isolated peak associated with a single trap state. Therefore, during the determination of fading in a given TL measurement, a decrease is observed due to different trap depths. The results showed that tunneling becomes more prevalent at low temperatures, whereas local transitions predominate above room temperature.

When it comes to optical dating, quartz and K-feldspar provide distinct advantages. K-feldspar can be evaluated selectively by infrared excitation, has a low heat transfer effect, saturates at larger radiation doses, and performs better on young samples because of its high luminescence intensity. On the other hand, quartz is more common, more resilient than feldspar, suitable for dating samples with less exposure to sunshine, and does not fade anomalously. K-feldspar's primary drawback is its anomalous fading, which may have an impact on dating outcomes (Huntley and Lamothe, 2001).

Significant research have concentrated on using feldspars because of a number of important benefits, despite the difficulties presented by anomalous fading in feldspar luminescence dating:

- Greater intrinsic luminescence brightness: Because feldspars are more luminous than quartz, it is simpler to detect lower doses of radiation.
- Internal potassium contribution: The potassium in feldspars contributes significantly to the overall radiation dosage, and this internal dose contribution remains stable over time, lowering uncertainty brought on by external variables such as water content.
- Infrared stimulation sensitivity: The sensitivity of feldspars to infrared stimulation (IRSL) enables the selective monitoring of feldspar signals even when other minerals are present.
- Range of extended dose-response: Compared to quartz OSL, feldspar IRSL signals typically exhibit better dose-response characteristics. Additionally, they may be able to expand the dating range past the saturation point of quartz OSL, which is reached at doses of a few hundred Gy.

Although the stability of the feldspar luminescence signal in aged samples due to anomalous fading, problems related to determining the age of the sample have not been solved yet. (Kang et al., 2010).

Numerous studies of fading have proposed the tunneling recombination of opposing charges. According to Dexter (1954), F-center electrons can tunnel from an excited state at higher temperatures or from the ground state of traps to positive hole centers without heat. At low temperatures, Hoogenstraaten (1958) also explained the presence of a decrease in signal in the TL curve of ZnS:Cu exposed to Co irradiation by the existence of escape from the temperature-independent tunneling trap. Tunneling in ZnS afterglow was proven by Riehl's et al. (1970) at 6 K. While Kieffer (1974) noted tunneling behavior in organic glasses and adenine, Delbecq et al. (1966) discovered a comparable tunneling-induced afterglow in KCl. Tunneling also explained Cunningham's (1971) observation of a temperature-independent afterglow in calcite. In a study of thermoluminescence (TL) and isothermal decay in calcite synthetic single crystals, Visocekas et al. (1976) showed that there was a weak emission of light at low temperature before the '360 K' (related with Mn) TL glow peak. This emission had the same light spectrum as the luminescence peak, but the TL intensity decreased with time and was not affected by temperature over a wide temperature range (from LNT to 180 K). They suggested that the two realizable states between the emission, one observed at 360 K and the other at low temperature, the traps and the Mn centers, could be explained by the tunneling process.

In the localized transition model, an excited state above the trapping barrier but below the conduction band can be shared by a trapped charge near a recombination center. Tunneling transitions, however, cannot use this transition. To calculate the time variation of the number of trapped electrons, the electron loss rate was measured assuming that the trapped electrons were associated with a single recombination center, i.e. there were no nearby recombination or re-trapping centers (Templer, 1986).

3. METHODS

3.1. Single Grain Dating

The simplest method for determining the equivalent dose (D_e) value in age calculation is to average the D_e values obtained from aliquots. It is known that aliquots consist of hundreds of grains, however, partially bleached samples in each aliquot cause highly irregular distributions in age. Therefore, single grain dating has been widely used

in the literature to overcome this problem. The following approaches were implemented to solve the fading problem.

3.1.1. Fading Correction

Based on the findings of a 2001 study by Huntley and Lamothe, it was stated that anomalous fading rates are related to geological origin and may reflect the geological age of the feldspar. Their proposed correction approach uses the parameter ‘g’ to describe the fading loss of luminescence to calculate the loss of luminescence over geological time. For this purpose, the formula $I_f/I_0 = T_f/T$ is recommended to make the correction by comparing the observed luminescence intensity (I_0) with the fading corrected intensity (I_f). The technique is limited to immature samples and the linear portion of the growth curve, but has the advantage of correcting fading in a single aliquot.

3.1.2. Fadia Method

In 1999, Lamothe and Auclair introduced several methods to correct the observed fading using feldspar IRSL to determine the true dates of geological or archaeological events. For this purpose they developed the Fadia technique (Lamothe and Auclair, 1999) based on data from the same sample using differential weathering of individual grains or aliquots. Thus, if feldspar grains are given the same dose in the natural environment, the equivalent dose for a non-fading feldspar can be calculated and the true paleodose can be determined. This is the first technique to provide possible adjustments for fading in sediment samples. However, Lamothe et al. (2003) noted that problems arise when there is quite variation in anomalous fading rates or when there are several grain populations.

3.1.3. Isochron Dating Method

Lamothe et al. (2012) selected 48 bright and dim grains for analysis, the first 24 of which were measured with the single aliquot regeneration (SAR) protocol with equivalent dose, while the others were measured with the equivalent dose value by exposing them to light under the unfiltered lamp. It was stated that the measured dose values of the first group of samples showed a small deviation, while the second group showed a wide distribution due to L_n/T_n anomalous fading. The natural luminescence intensity (L_n) is the product of the total accumulated dose in the natural environment and the luminescence sensitivity to the dose.

Since the dose rate was assumed to be equal for each grain, the variation in the luminescence intensity (Ln) was a result of the variable sensitivity to the natural dose due to the difference in the fading rates among individual feldspar grains. Lamothe suggested that future studies should focus on non-fading bright grains, as these are likely to be the most stable. He recommended caution when dealing with partially bleached sediments, as bright grains may contain residual doses. It was suggested that large numbers of non-fading bright grains be extracted and measured, which would clearly allow them to be treated in a similar manner to quartz. However, it was noted that this approach may be more challenging in samples with severe fading.

It was proposed to extract and measure a large number of non-fading bright grains, which would clearly allow them to be treated similarly to quartz. However, it has been realized that this approach may cause more problems in samples with severe fading.

3.2. Time Resolved Luminescence

On the basis of the far-red emission in the TL of feldspars, several strategies for avoiding anomalous fading had been suggested. Bos et al. (1994) have proposed far-red emission in the TL of feldspars, with a center around 710 nm and a width of approximately 120 nm, as a solution to anomalous fading. This emission, which was ascribed to impurities, is found at lower temperatures during the tunnel afterglow as well as throughout the TL glow curve (Visocekas, 1993). Because of its limited spectrum sensitivity beyond 750 nm, it was more consistently seen than typical TL emissions in feldspars and cannot be measured with standard TL equipment. Visocekas et al. (1994) and Blanc (2000) recommended using cathodoluminescence (CL) at room temperature to prevent interference from thermal background emission (Visocekas and Guerin, 2006).

In order to avoid interference, Visocekas and Guerin (2006) set up TL detection to simultaneously capture two broad bands: the blue from 400 to 570 nm and the far-red from 630 to 750 nm. They left out the 570 to 630 nm area since stable and fading emissions overlap there.

This emission has enabled dating with TL and has been extended to the IRSL method. Comparison of immediate TL and stored TL measurements in 'blue' and far-red bands reveals that the important characteristic of feldspar's far-red emission is its stability during storage.

Tsukamoto et al., (2006) investigated whether distinct lifetime components fade at different rates by analyzing the luminescence features of the long-lived part of feldspars. In order to assess the relative contributions of natural and reconstructed IR-OSL signals, including delayed and rapid components, the study involved monitoring the signals. The behavior of the signals under various excitation techniques was also examined by comparing continuous wave (CW) results with pulsed excitation data. The main findings regarding the luminescence properties of K- and Na-feldspar samples from the study were as follows (Table 1.):

Table 1. Results regarding the luminescence properties of K- and Na-feldspar samples as a result of his study by Tsukamoto (2006). tabulated by me

<i>Property</i>	<i>K-Feldspar</i>	<i>Na-Feldspar</i>
Relative Contribution of Long Lifetime Components	Greater (~20 μ s)	Lower
Signal Stability	More stable long lifetime components	Less stable long lifetime components
Pulsed vs. Continuous Wave (CW) D_e Values	Higher pulsed D_e values	Lower pulsed D_e values
Anomalous Fading	May not exhibit anomalous fading	Potentially more affected by fading
Signal Rise and Decay Rate	Slower rise and decay	Faster rise and decay

According to Tsukamoto et al.(2006), K-feldspars with long-lived components (around 20 μ s) were substantially more stable than those with shorter-lived, which were more susceptible to anomalous fading. This finding, which was derived from comparing fast/delayed and natural/reconstructed time-resolved IR-OSL signals, implies that long-lived components were more resilient and may yield more reliable and accurate age estimates, enhancing the dependability of luminescence dating methods.

In terms of chemical bonding, Riedesel et al. (2021) described how aluminum (Al) and silicon (Si) atoms in feldspars were arranged in the crystal structure and the relationship between TL emission spectra and IRSL fade rates. When atoms form an ordered structure, chemical bonds are more stable and there are fewer defects and dislocations in the crystal structure. This reduces energy loss (fading). However, the chemical bonds of disordered structures are less stable and contain more defects, which affects energy transfer and increases the fading rate. Especially in perthites formed from a mixture of potassium feldspar (K-feldspar) and sodium feldspar (Na-feldspar) minerals, where two different

mineral phases are formed during the cooling process and sodium and potassium are transported to different regions, the arrangement of Al-Si bonds is affected by defects and dislocations at the lamella interfaces, which leads to weakening of chemical bonds and an increase in fading rates.

4. COMPARISON OF PROTOCOLS FOR THE SOLUTION OF ANOMALOUS FADING

Numerous fading mitigation techniques have been developed as a result of the explanation of the mechanism behind anomalous fading in terms of quantum mechanical tunneling (Zink et al., 1995). Sanderson and Clark (1994) used a nitrogen dye laser set at 470 nm to observe pulsed optically stimulated luminescence (OSL) on K-feldspars. Using 850 nm laser stimulation, Clark et al. (1997) and Clark and Bailiff (1998) showed that the recombination lifetimes of feldspars ranged from tens of nanoseconds to several microseconds (Tsukamoto, 2006).

4.1. Post IR-IRSL

Buylaert (2009) tested a dating protocol based on a post-IR elevated temperature IR signal and compared the results with those obtained from the more generally used standard IR signal measured at 323 K. In this study data were obtained from dose response, performance at SAR, fading rate and bleaching. Thiel et al. (2011) also increased the preheat step in the Buylaertin protocol to 593 K and steps 4 and 8 to 563 K. However, it was observed that residual doses gradually increased in parallel with both the increment of the preheat and the excitation temperature (Zhang et al., 2015). On the other hand, Reiman et al. (2011) carried out a study that significantly reduced the residual dose (Zhang and Li, 2020).

4.2. Multielevated-temperatures post-IR IRSL (MET-pIRIR)

Compared to quartz OSL, the IRSL signal from feldspars saturates at greater doses, providing a broader dating range. Additionally, its stronger signal enables more sensitive (Li et al., 2007b) and consistent observations (Li and Li, 2011). Fading rates were reduced by increasing the infra red excitation temperature (Thomsen et al., 2008) or by using multiple-high-temperature protocols (MET) by Li and Li (2011) . Li and Li (2011) proposed a protocol using post-IR IRSL signals to reduce the effects of anomalous fading in K-feldspar dating. In this method, IRSL

signals were recorded at progressively higher excitation temperatures. To further minimize anomalous fading, this technique, named MET-pIRIR (multiple elevated temperature post-IR infrared stimulated luminescence), was developed, allowing more stable equivalent dose (D_e) values to be obtained at higher temperatures (473–523 K). As a result, more accurate age estimations were obtained, which were found to be consistent with the independent dating methods such as quartz OSL. In addition, a wide range of sedimentary samples were successfully dated using this method, highlighting its broad applicability and reliability for luminescence dating without requiring fading corrections. The MET-pIRIR technique follows a systematic protocol: sediment samples, like K-feldspar, are irradiated and preheated (e.g., 573 K for 10 seconds). Luminescence signals are measured by progressively increasing the stimulation temperature from 323 to 523 K, recording IRSL signals at each step. These signals are normalized using a test dose and analyzed to calculate the equivalent dose (D_e) values, which increase with temperature, indicating stable, non-fading signals. This method has been tested on a wide range of sedimentary samples with ages from 0 to 120 ka, demonstrating its versatility and applicability across different geological contexts.

Here's a step-by-step breakdown of the methods used to measure time-resolved infrared optically stimulated luminescence (IR-OSL) signals in the study:

- Sample Preparation: In order to conduct analysis, samples of K- and Na-feldspar were taken out of sediments. The samples were prepared for luminescence testing by preheating them for 60 seconds at 523 K before to each measurement.
- Source of Stimulation: An LED (Vishay TSHA650) that emits pulsed infrared light with a wavelength of about 875 nm was used to stimulate IR-OSL signals. Luminescence readings were collected at predetermined intervals owing to this pulsed stimulation.
- Fast Photon Counter: A fast photon counter was used to find the luminescence signals produced by the feldspar samples throughout the stimulation procedure.

Time-resolved luminescence data might be effectively captured using this configuration. Red, blue, and UV detection windows were

among the various wavelengths at which luminescence signals were detected.

5. CONCLUSIONS

In this study, I have compiled methodologies proposed by many authors to improve the results of studies on fading, which is a very important component of luminescence studies. Of course, the problems will be reduced by the development of methods such as single-grain laser luminescence systems, as proposed by the authors, or by the choice of the right protocols to be applied at different ages. As can be seen in this review of approximately 40 articles on the subject, studies on fading have been increasing over the years. This review is a guide for interested authors.

REFERENCES

- Abraham J., Mohammed A. P., Ajith Kumar M.P., George S. C., Thomas S. (2018). Chapter 8 - Thermoanalytical Techniques of Nanomaterials, *Characterization of Nanomaterials*, 213-236.
- Bo Li, Sheng-Hua Li, (2011). Luminescence dating of K-feldspar from sediments: A protocol without anomalous fading correction. *Quaternary Geochronology*, 6, 5, 468-479.
- Bos, A.J.J., Piters, T.M., Ypma P.J. (1994). Thermoluminescence emission spectra and optical bleaching of oligoclase, *Radiation Measurements*, 23, 349-353.
- Buylaert, J.P., Murray, A.S., Thomsen, K.J., Jain, M. (2009). Testing the potential of an elevated temperature IRSL signal from K-feldspar. *Radiation Measurements*, 44, 560–565.
- Clark, R.J., Bailiff, I.K., Tooley M.J. (1997). A preliminary study of time-resolved luminescence in some feldspars, *Radiation Measurements*, 27, 211-220.
- Clark, R.J., Bailiff I.K. (1998). Fast time-resolved luminescence emission spectroscopy in some feldspars, *Radiation Measurements*, 29, 553-560.
- Cunningham, J. (1971). Luminescence from calcite single crystals irradiated at 4· 2 K. *International Journal for Radiation Physics and Chemistry*, 3, 467.
- Delbecq, C.J., Ghosr A. K. and Yuster, P. H. Trapping and annihilation of electrons and positive holes in KCl-TlCl. *Physical Review*, 1966, 161, 599.
- Dexter, D. L. (1954). X-Ray Coloration of Alkali Halides, *Physical Review*, 93, 985.
- Hoogenstraaten, W. (1958). Philips Res. Rep. 13, 515 (Thesis).
- Huntley, D.J. (2006). An explanation of the power-law decay of luminescence, *Journal of Physics Condensed Matter*, 18, 1359-1365.
- Huntley, D.J.; Lamothe, M. (2001). Ubiquity of anomalous fading in K-feldspars and the measurement and correction for it in optical dating. *Canadian Journal Earth Science*, 38, 1093–1106.

- Jonscher A.K. and Anne de Polignac, (1984). The time dependence of luminescence in solids, *Journal Physics C: Solid State Physics*, Printed in Great Britain, 17, 6493-6519.
- Jonscher, A.K. and de Polignac, A. (1984). The Time Dependence of Luminescence in Solids. *Journal of Physics C: Solid State Physics*, 17, 6493-6520.
- Kang, S.G., Wang, X.L., Li, X.N., Lu, Y.C. (2010). Anomalous fading of the IRSL signal of polymineral grains in Chinese loess. *Radiation Measurements*, 45, 1, 22-28
- Kieffer, F., Lapersonne-Meyer C., and Rigaut, J. (1974). Deferred Isothermal Luminescence in organic glasses at 4° 2 and 77 K: Tunnelling and thermal detrapping. *Internat. Journal Radiation Physics Chemistry*, 6, 79.
- Lamothe, M., Auclair, M. (1999). A solution to anomalous fading and age shortfalls in optical dating of feldspar minerals. *Earth and Planetary Science Letters*, 171, 319-323.
- Lamothe, M., Auclair, M., Hamzaoui, C., Huot, S. (2003). Towards a prediction of long-term anomalous fading of feldspar IRSL. *Radiation Measurements*, 37, 493-498.
- Lamothe, M., Barré, M., Huot, S., Ouimet S. (2012). Natural luminescence and anomalous fading in K-feldspar. *Radiation Measurements*, 47, 9, 682-687.
- Li, S.H., Chen Y.Y., Li, B., Sun, J.M., Yang L.R. (2007). OSL dating of sediments from desert in northern China. *Quaternary Geochronology*, 2, 23-28.
- Li, B., Li, S.-H. (2011). Luminescence dating of K-feldspar from sediments: A protocol without anomalous fading correction. *Quaternary Geochronology*, 6, 468-47.
- McKeever, S.W.S. (1985). *Thermoluminescence of Solids*, Cambridge University Press, London, 1-376.
- McKeever, S.W.S., Bøtter-Jensen, Agersnap Larsen, N., Duller G.A.T. (1997). Temperature dependence OF OSL decay curves experimental and theoretical aspects. *Radiation Measurements*, 27, 161-170.

- Michel L., Magali B., Sébastien H., Stéphanie O. (2012). Natural luminescence and anomalous fading in K-feldspar. *Radiation Measurements*, 47, 9, 682-687.
- Reimann, T.; Tsukamoto, S.; Naumann, M.; Frechen, M. (2011). The potential of using K-rich feldspars for optically dating of young coastal sediments—A test case from Darss-Zingst peninsula (southern Baltic Sea coast), *Quaternary Geochronology*, 6, 207–222.
- Riedesel, S., Bell, A.M.T., Duller, G.A.T., Finch, A.A., Jain, M., King, G.E., Pearce, N.J., Roberts, H.M. (2021). Exploring sources of variation in thermoluminescence emissions and anomalous fading in alkali feldspars, *Radiation Measurements*, 141, 106541.
- Riehl, N. (1970). Tunnel luminescence and infrared stimulation, *Journal of Luminescence*, 1, 1.
- Sanderson, D.C.W., Clark, R.J. (1994). Pulsed photostimulated luminescence of alkali feldspars. *Radiation Measurements*, 23, 633-639.
- Templer, R.H. (1986). The Localised Transition Model of Anomalous Fading. *Radiation Protection Dosimetry*, 17, 493-497.
- Thomsen, K.J., Murray, A.S. Jain, M., Bøtter-Jensen L. (2008). Laboratory fading rates of various luminescence signals from feldspar-rich sediment extracts, *Radiation Measurements*, 43, 1474-1486.
- Tsukamoto, S., Denby, P.M., Murray, A.S. Bøtter-Jensen, L. (2006). Time-resolved luminescence from feldspars: New insight into fading. *Radiation Measurements*, 41, 7–8, 790-795.
- Visocekas, R., Ceva, T., Marti, C., Lefaucheux, F., Robert M. C. (1976). Tunneling processes in afterglow of calcite, *Physica status solidi (A)*, 35, 315-327.
- Visocekas R. (1993). Tunneling radiative recombination in K-feldspar sanidine, *Nuclear Tracks Radiation Measurements*, 21, 175-178
- Visocekas, R., Spooner, N.A., Zink, A., Blanc P. (1994). Tunnel afterglow, fading and infrared emission in thermoluminescence of feldspars, *Radiation Measurements*, 23, 377-385.

- Visocekas, R., Guérin, G. (2006). TL dating of feldspars using their far-red emission to address anomalous fading. *Radiation Measurements*, 2006, 41, 942-947.
- Wintle, A.G. (1977). Detailed study of a thermoluminescent mineral exhibiting anomalous fading, *Journal of Luminescence*, 15, 385-393.
- Zhang, J.R., Tsukamoto, S., Nottebaum, V., Lehmkühl, F., Frechen, M. (2015). De plateau and its implications for post-IR IRSL dating of polycrystalline fine grains. *Quaternary Geochronology*, 30, 147–153.
- Zhang, J., Li, S-H. (2020). Review of the Post-IR IRSL Dating Protocols of K-Feldspar. *Methods and Protocols*, 3, 1, 7.
- Zink, A.J.C., Visocekas, R., Bos, A.J.J. (1995). Comparison of ‘Blue’ and ‘Infrared’ emission bands in thermoluminescence of alkali feldspars. *Radiation Measurements*, 24 (4), 513-518.

A VIEW OF COHERENT ELASTIC NEUTRINO-NUCLEUS SCATTERING AND BEYOND STANDARD MODEL: THE NEW LIGHT MEDIATORS

Mehmet DEMİRÇİ¹

M. Fauzi MUSTAMİN²

1. INTRODUCTION

Coherent elastic neutrino-nucleus scattering (CEvNS) is a standard model (SM) process in which neutrinos scatter off a nucleus as a whole [1]. It is well described in the SM by the neutral current interaction of neutrinos and quarks, in which its cross section is proportional to the square of the neutron number. The CEvNS cross-section is larger than other neutrino interaction observables at the same regime of neutrino energy. The challenge of observing this process is sourced from its nuclear recoil energy which is located in the low keV scale. This quantity is the only observable signature of the process and its low energy recoil property is the required criterion to ensure coherency as neutrinos interact with the nucleus.

The developments of very sensitive detector technologies allow us to observe this magnificent achievement. The CEvNS process was first observed by the COHERENT collaboration in 2017 [2], more than 40 years after its first theoretical description. The collaboration has been able to uncover small recoil energy criteria of the CEvNS in a neutron source facility. They used neutrinos emerging from pion decay at rest (π -DAR) at a Spallation Neutron Source (SNS) with a CsI[Na] scintillating crystal detector in their first measurement and then performed another attempt using a liquid argon detector [3]. They have recently updated the CsI data analysis with higher statistics along with an improved understanding of experiment systematics [4].

¹ Assoc. Prof., Karadeniz Technical University, Department of Physics, Trabzon 61080, Türkiye, mehmetdemirci@ktu.edu.tr, ORCID: 0000-0003-2504-6251.

² PhD, Karadeniz Technical University, Department of Physics, Trabzon 61080, Türkiye, mfmustamin@ktu.edu.tr, ORCID: 0000-0003-3996-4651.

Many other works have been actively investigating the CE ν NS phenomena following the achievements of COERENT. The Dresden-II collaboration [5], working at the nuclear power reactor, recently reported an event spectrum compatible with expectations of a CE ν NS signal in the SM. Similar experiments such as CONNIE [6] and CONUS [7] are still running towards observing their first CE ν NS signals and so far have been able to obtain upper limits that are compatible with the SM prediction. Direct detection (DD) experiments of dark matter (DM) also play a significant role in measuring the CE ν NS from astrophysical sources, since the process contributes significantly in the background and it has a very similar prediction with the proposed weakly interacting massive particle (WIMP). The PandaX [8] and XENON [9] experiments are some examples of such works that utilize Xenon as the target nuclei. Both experiments have recently reported their results on CE ν NS signals induced by ${}^8\text{B}$ neutrino flux [10, 11]. It is worth mentioning that there are other planned or under-construction CE ν NS-related experiments, such as NUCLEUS [12] and the European Spallation Source [13]. These developments have triggered many scientific activities, both theoretical and experimental, and will continue in the near future.

The CE ν NS process provides an alternative point of view to investigate SM predictions and new physics beyond the SM (BSM). It has been widely used to study the weak mixing angle at low energy [14, 15]. As for BSM proposals, it has also been utilized to investigate the neutrino electromagnetic properties [16, 17], the effective generalized interactions [18], the non-standard neutrino interactions (NSI) [19, 20], dark matter (DM) research [21], and the light mediators [22, 23, 24]. Furthermore, the CE ν NS process provides useful information on the nuclear structure, particularly on the nucleus neutron density distribution that is still unknown for most nuclei [25]. Moreover, it can be used to investigate the Migdal effect, an effect in which the ionization process of an atom follows a nuclear recoil [26], that potentially plays a role in direct-detection of dark matter experiments. In most experiments, the only signal of a CE ν NS event is a nuclear recoil energy deposition. In principle, future experiments with more advanced detector technologies could detect both nuclear recoil and angular distribution simultaneously. Such capabilities are already being explored in some DM experiments and will significantly increase the physics capabilities of future CE ν NS experiments [27].

The work aims to highlight the wide implications of the CE ν NS process. We discuss the SM formulation of CE ν NS in the Section 2, including description of form factor and quenching factor effects. In Section 3, we explain the application for CE ν NS to BSM physics, focusing on light mediators. We finally summarize this paper in the Section 4.

2. STANDARD FORMULATION OF CE ν NS

The CE ν NS process is well formulated in the framework of the SM. It occurs as neutrinos with initial energy E_ν scatter off a nucleus target. The scattered nucleus carries a kinetic recoil energy T_{nr} in a few keV. The process is a pure quantum effect where the initial neutrino has a small enough energy so that it is unable to see the nucleon structure. This generally happens when the transfer momentum $\vec{q} \lesssim R$, where R represents the typical nuclear size. The process hence provides enhancement of cross-section in low energy nuclear recoil region.

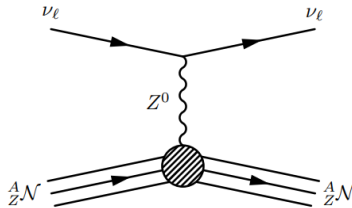


Figure 1. Representative Feynman diagram for SM CE ν NS process

The Feynman diagram of CE ν NS in the SM is shown in Fig. 1. The factor ${}^A_Z N$ represents a nucleus with A nucleons (Z protons and N neutrons) and Z^0 is the SM neutral vector boson. The subscript ℓ denotes the neutrino flavor e , μ or τ . As neutrino interacts with the nucleus as a whole in CE ν NS, the cross-section is much larger than those of other processes such as charged-current (CC) neutrino interactions or neutrino-induced neutron (NIN), inverse beta decay (IBD), and elastic scattering of ν_e on electrons [28]. The differential cross section for CE ν NS in the SM with respect to the nuclear recoil energy is given by

$$\left[\frac{d\sigma}{dT_{nr}} \right]_{\text{SM}} = \frac{G_F^2 m_N}{\pi} Q_{\text{SM}}^2 \left(1 - \frac{m_N T_{nr}}{2 E_\nu^2} \right) |F(|\vec{q}|^2)|^2. \quad (2.1)$$

The term G_F represents the Fermi constant, m_N is the nucleus mass, and $F(|\vec{q}|^2)$ is the weak nuclear form factor. We define the weak nuclear charge as $Q_{\text{SM}} = g_V^p Z + g_V^n N$, where the vector couplings are given by $g_V^p = (1 - 4\sin^2\theta_W)/2$ $g_V^n = -1/2$ for proton and neutron, respectively. We use $\sin^2\theta_W = 0.23863$ [29] for the weak-mixing angle, which is obtained at low-momentum transfer in the $\overline{\text{MS}}$ scheme. The SM cross section of CE ν NS is N^2 dependent due to the small prefactor associated with Z in Q_{SM} , and flavor blind at the tree level. Note that the cross-section Eq. (2.1) is valid for both neutrino and anti-neutrino cases.

The weak nuclear form factor $F(|\vec{q}|^2)$ contains the complex structure of the target nucleus. The form factor difference for proton and neutron is generally considered to be negligible, hence both form factors are taken to be equal, namely $F_p \simeq F_n \simeq F$. The basic properties of nucleus structure in the form factor are captured by different parameterizations, such as the Klein-Nystrand [30], the symmeterized Fermi [31], and the Helm [32] parameterization. The Helm parameterization is widely used for CE ν NS, given by

$$F(|\vec{q}|^2) = 3 \frac{j_1(|\vec{q}|R_0)}{|\vec{q}|R_0} e^{-\frac{1}{2}|\vec{q}|^2 s^2}, \quad (2.2)$$

where the function $j_1(x) = \sin x / x^2 - \cos x / x$ is the first-order Spherical Bessel function. The three-momentum transfer is $|\vec{q}| = \sqrt{2m_N T_{nr}} / 197.3 \text{ fm}^{-1}$. The diffraction radius is defined by $R_0^2 = \frac{5}{3} R^2 - 5s^2$, where $R = 1.23A^{1/3}$ is the nuclear radius and $s = 0.9 \text{ fm}$ is the surface thickness.

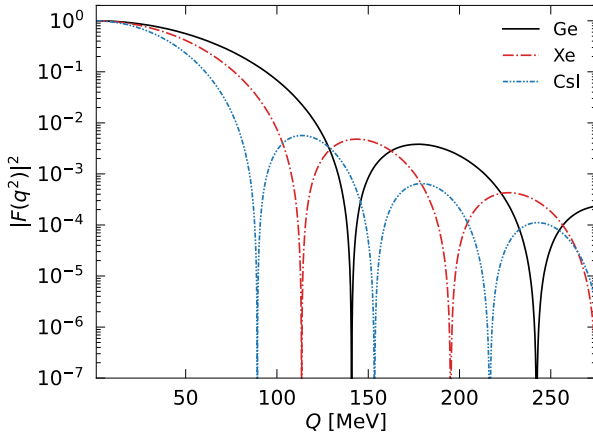


Figure 2. Form factor behavior for Helm parametrization as a function of momentum transfer for several nuclei.

In Fig. 2, we plot the behavior of the Helm form factor for several nuclei as a function of momentum transfer with relation $Q^2 = -q^2$. Notice that in the coherence limit $q^2 \rightarrow 0$ the form factor is normalized to $F(0) = 1$.

Any deviation from the predicted SM CEvNS event rate may indicate new contributions to the interaction cross section, either by a change in the total event rate or by a change in the shape of the recoil spectrum. The CEvNS event rate is calculated in terms of nuclear recoil energy as

$$\frac{dR}{dT_{nr}} = N_T \int_{E_\nu^{\min}}^{E_\nu^{\max}} \frac{d\Phi(E_\nu)}{dE_\nu} \frac{d\sigma(E_\nu, T_{nr})}{dT_{nr}} dE_\nu, \quad (2.3)$$

where N_T is the number of nuclei in the detector per unit mass and $d\Phi(E_\nu)/dE_\nu$ is the neutrino flux per cm^2 per second from a particular source. The integration is taken from the minimum neutrino energy E_ν^{\min} to the maximum neutrino energy E_ν^{\max} . The minimum neutrino energy is given by

$$E_\nu^{\min} = \frac{T_{nr}}{2} \left(1 + \sqrt{1 + \frac{2m_N}{T_{nr}}} \right). \quad (2.4)$$

It is important to note that in the detector, the observed energy is in the electron-equivalent recoil energy T_{ee} . To transform this into the nuclear recoil T_{nr} when calculating the predicted CEvNS rate, we need to use the following relation

$$T_{ee} = f_Q(T_{nr})T_{nr}. \quad (2.5)$$

In this relation, f_Q represents the quenching factor. This dimensionless quantity is defined as the ratio of the ionization energy generated by nuclear recoils over the one generated by electron recoils of the same energy. As a function of the electron equivalent energy, the differential rate is given by

$$\frac{dR}{dT_{ee}} = \frac{dR}{dT_{nr} f_Q + T_{nr} \times df_Q/dT_{nr}}. \quad (2.6)$$

In this conversion process, most of the initial energy is lost in dissipative processes and, thus, not accessible. The quenching factor has been extensively measured for nuclear recoils in a few tens of keV range where it follows the energy dependence

$$f_Q(T_{nr}) = \frac{kg(\epsilon)}{1 + kg(\epsilon)}, \quad (2.7)$$

which is known as the Lindhard quenching factor [33]. In this equation $\epsilon = 11.5Z^{-7/3}T_{nr}$ and $k = 0.133Z^{2/3}A^{-1/2}$ while $g(\epsilon) = 3\epsilon^{0.15} + 0.7\epsilon^{0.6} +$. It is observed that the Lindhard quenching factor is well used for energy $T_{nr} \gtrsim 1$ keV [34]. However, for sub-keV nuclear recoils, the quenching factors are not well predicted by this model due to uncertainties in nuclear scattering. Precise measurements of this factor at these energies are still lacking and the Lindhard theory is not valid anymore. Because of this, there are various quenching factors in the literature that could effect the measured results. For example, one proposes modification of the Lindhard theory [35] and other uses experimental data of detector calibration which called the Iron-filtered [36] quenching factor. Therefore, the determination of this quenching factor in this range is tremendously important to improve experimental sensitivity and to precisely measure the CEvNS signals in the future.

3. BEYOND THE STANDARD MODEL: LIGHT MEDIATORS

Empirical results of neutrino oscillation phenomena show that neutrinos are massive [37, 38, 39]. The discovery leads to the activity of searching for the true nature of neutrinos. The lack of significant signals from high-energy experiments opens a new perspective to search for new physics in the low-energy scale. Below the electroweak symmetry breaking, other types of neutrino interactions with other fundamental particles may come into consideration for new physics phenomena. Along with vector and axial-vector types, other Lorentz invariant bilinear combinations may also be introduced at this low scale. From these spirits, an extension to the SM Lagrangian is needed for accommodating the new mediators.

We are interested in light mediators from a simplified model and also from $U(1)'$ anomaly-free theory. Both extend the SM with a proposed BSM scenario of new particles. This extension may lead to deviation from the standard theory in the framework of CEvNS.

A simplified model in general is an alternative type of model in high-energy physics to relate theoretical prediction with experimental data from measurements. Experimental parameters from this kind of model consider only new masses and cross-sections as well as branching ratios, while the common full extensions of BSM involve plenty of particles with decay chains accordingly. Hence, it is important to note that simplified models do not represent the actual physics beyond the SM [40]. Nevertheless, explaining simplified models is still worth consideration as it can be embedded into the standard theory to see their effect.

We consider general new neutrino interactions, namely scalar, vectorial [41], and tensor [42]. Each of these is considered to carry light masses and hence couple to neutrinos and quark constituents of the nucleus. The following corresponds to Lagrangian for scalar cases:

$$\mathcal{L}_\phi \supset -\phi \left[\sum_q g_\phi^q \bar{q} q + g_\phi^{v_\ell} \bar{v}_{\ell R} v_{\ell L} + h.c. \right]. \quad (3.1)$$

The scalar coupling constant g_ϕ^q is for q-quark and $g_\phi^{v_\ell}$ for neutrino. The label ℓ refers to lepton flavor e , μ , and τ . Meanwhile, for the vector case, we have

$$\mathcal{L}_{Z'} \supset Z'_\mu \left[\sum_{q=u,d} Q'_q g_{Z'}^q \bar{q} \gamma^\mu q + Q'_\ell g_{Z'}^{v_\ell} \bar{\nu}_{\ell_L} \gamma^\mu \nu_{\ell_L} \right]. \quad (3.2)$$

The $g_{Z'}^q$ and $g_{Z'}^{v_\ell}$ are vector coupling constants for q -quark and neutrino, respectively. Finally, for the tensor case, the Lagrangian is

$$\mathcal{L}_T \supset \left[\sum_q g_T^q \bar{q} \sigma^{\mu\nu} q - g_T^{v_\ell} \bar{\nu}_{\ell_R} \sigma^{\mu\nu} \nu_{\ell_L} \right] T_{\mu\nu}. \quad (3.3)$$

The g_T^q and $g_T^{v_\ell}$ are tensor coupling constants for quarks and neutrinos, respectively. Note that $\sigma_{\mu\nu} = i(\gamma_\mu \gamma_\nu - \gamma_\nu \gamma_\mu)/2$. To obtain the physical observable, we need to match the quark level current to the nucleus level. It is performed by first connecting the quark Lagrangian to the nucleon Level, and then the obtained nucleon case to the nucleus level. After that, we calculate the amplitudes for each case.

The differential cross-section calculation from each case is straight forward. Differential cross-section for the light scalar mediator is

$$\left[\frac{d\sigma}{dT_{nr}} \right]_\phi = \frac{Q_\phi^2 T_{nr} m_N^2 |F(|\vec{q}|^2)|^2}{4\pi (m_\phi^2 + 2m_N T_{nr})^2 E_v^2}. \quad (3.4)$$

The scalar charge of the nucleus Q_ϕ is defined as

$$Q_\phi = \left[Z \sum_q g_\phi^q \frac{m_p}{m_q} f_{Tq}^p + N \sum_q g_\phi^q \frac{m_n}{m_q} f_{Tq}^n \right] g_\phi^{v_\ell}, \quad (3.5)$$

where we set the hadronic structure parameters as $f_{T_u}^p = 0.0208$, $f_{T_u}^n = 0.0189$, $f_{T_d}^p = 0.0411$, and $f_{T_d}^n = 0.0451$ [43]. The parameters m_p , m_n , and m_q are masses for proton, neutron, and quark, respectively. This scalar interaction does not interfere with the SM. Hence, the new scalar mediator

contribution adds incoherently to the SM CE ν NS cross-section. In the case of vector mediator, contribution to the CE ν NS cross-section is

$$\left[\frac{d\sigma}{dT_{nr}} \right]_{Z'} = \frac{Q_{Z'}^2 m_N |F(|\vec{q}|^2)|^2}{2\pi(m_{Z'}^2 + 2m_N T_{nr})^2} \left(1 - \frac{m_N T_{nr}}{2E_\nu^2} \right), \quad (3.6)$$

where $Q_{Z'}$ is the weak vector charge of the nucleus. Vector current conservation implies that only valence quarks contribute by simply adding their charges, so we have

$$\begin{aligned} Q_{Z'} &= \left[Z \sum_q Q'_q g_{Z'}^q + N \sum_q Q'_q g_{Z'}^q \right] Q'_\ell g_{Z'}^{v_\ell} \\ &= [Z(2Q'_u + Q'_d) + N(Q'_u + 2Q'_d)] g_{Z'}^q g_{Z'}^{v_\ell} Q'_\ell. \end{aligned} \quad (3.7)$$

We give the above relation on $Q_{Z'}$ in the general form in terms of charges Q'_u , Q'_d , and Q'_ℓ . However, in the framework of the universal mediator, the vector mediator couples universally to all the SM fermions. Accordingly, we set $Q'_u = Q'_d = Q'_\ell = 1$ in Eq. (3.7) for this model. Since both the SM and the Z' interactions are of vector type, they contribute coherently to the CE ν NS cross-section. The Z' mediator has an interference term with the SM case, so we have the complete cross-section as follows

$$\left[\frac{d\sigma}{dT_{nr}} \right]_{SM+Z'} = \left[1 + \frac{Q_{Z'}}{\sqrt{2}G_F Q_{SM}(m_{Z'}^2 + 2m_N T_{nr})} \right]^2 \left[\frac{d\sigma}{dT_{nr}} \right]_{SM}. \quad (3.8)$$

For the tensor case, the cross-section contribution to CE ν NS is

$$\left[\frac{d\sigma}{dT_{nr}} \right]_T = \frac{2Q_T^2 m_N |F(|\vec{q}|^2)|^2}{\pi(m_T^2 + 2m_N T_{nr})^2} \left(1 - \frac{m_N T_{nr}}{4E_\nu^2} \right). \quad (3.9)$$

In this relation, the charge is

$$Q_T = \left[Z \sum_q g_T^q \delta_q^p + N \sum_q g_T^q \delta_q^n \right] g_T^{v_\ell}. \quad (3.10)$$

The parameters in the relation above are $\delta_u^p = \delta_d^n = 0.54$, and $\delta_d^p = \delta_u^n = -0.23$ [43]. Note that this mediator does not interfere with the SM case.

There are many studies of SM extensions with the addition of a $U(1)'$ gauge group with an associated neutral gauge boson Z' . A necessary condition is that the theory is anomaly-free. Anomaly-free models can be constructed by expanding the SM with three right-handed neutrinos. Such expansion simultaneously explains the smallness of neutrino mass through the see-saw mechanism [44]. Such models can explain some unsolved puzzles in the SM such as the grand unified theory [45], nature of DM [46], and anomalies from experiments [47]. Some models coming from an additional vector Z' mediator with an associated $U(1)'$ gauge group are $U(1)_{B-L}$ [48, 49, 50, 51] $U(1)_{B-3L_e}$, $U(1)_{B-3L_\mu}$, and $U(1)_{B-3L_\tau}$ [52, 53, 54]. In these models, B stands for the baryon number and L is for the lepton number. The models differ in terms of the charges of the fermions with the associated gauge group. We list the $U(1)'$ charges of quarks and leptons in Table 1 for each model. It is seen that the vector Z' mediator couples to the quarks and neutrinos with different charges. This difference determines the contributions of each model to CEvNS. Accordingly, the corresponding differential cross-sections are obtained from Eq. (3.8) by substituting these charges to Eq. (3.7).

Table 1. The gauge charges of quarks and leptons for each considered model

Model	Q'_u	Q'_d	Q'_e	Q'_μ	Q'_τ
universal	1	1	1	1	1
$B - L$	1/3	1/3	-1	-1	-1
$B - 3L_e$	1/3	1/3	-3	0	0
$B - 3L_\mu$	1/3	1/3	0	-3	0
$B - 3L_\tau$	1/3	1/3	0	0	-3

Hence, these contributions add coherently to the weak neutral current of the SM which is mediated by the Z vector boson. The effects are quantified by additional terms in the nucleus weak charge.

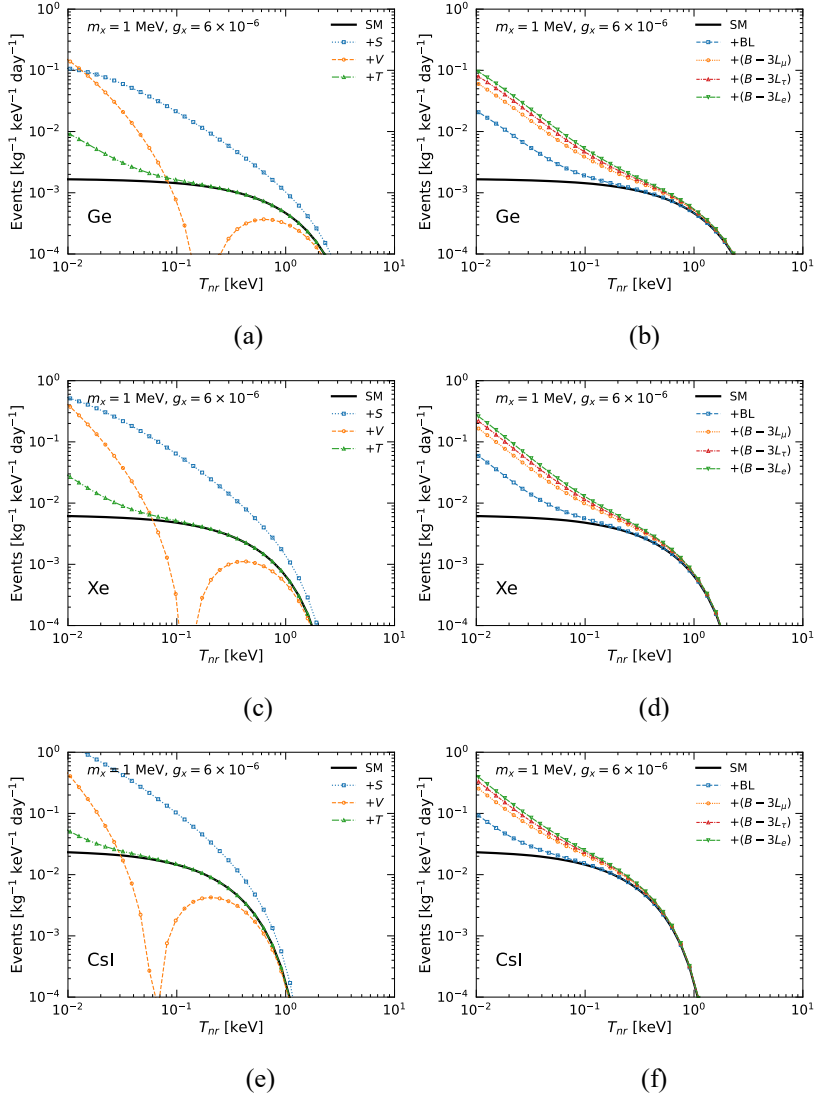


Figure 3. Predicted event rate for the universal light mediators (left) and $U(1)'$ vector mediators (right). Here, we take three different target nuclei of Ge (top), Xe (middle), and CsI (bottom)

We present the predicted event rates for each contribution of light mediators from universal and $U(1)'$ models to CEvNS in Fig. 3. using three different targets. These are Ge (top), Xe (middle), and CsI (bottom). The black solid lines represent the SM spectrum. Note that the neutrino oscillation probability is included to address flavor dependency in the $B - 3L_e$, $B - 3L_\mu$, and $B - 3L_\tau$ cases. The contribution of each light mediator is embedded with the SM prediction. We consider benchmarks of light

mediator mass $m_x = 1$ MeV and coupling constant $g_x = 6 \times 10^{-6}$ for each case.

The vector mediator contribution is generally observed when $T_{nr} < 1$ keV. It shows smaller effects as the recoil energy is around the interference region. It is seen that the interference effect reduces the spectrum of the universal vector case. The significant enhancement is seen after the interference effect is surpassed in lower energy. Concerning the light scalar mediator, it enhances the SM spectrum in all energy region. This is anticipated from the cross-section that is proportional to inverse of nuclear recoil. The differential cross section scales as T_{nr} for small energy region, before cutting off at high energy due to a loss of coherency. Meanwhile, the contribution of the light tensor mediator is significant in the low nuclear recoil region of $T_{nr} \lesssim 1$ keV for each target. It shows similar behavior with the vector case, where the tensor case has a relatively lower contribution that comes from the difference in the kinematic factor. For the $U(1)'$ cases, their appearance have observable effects at small recoil energy region in all nuclear target. The $B - L$ effects generally occur as $T_{nr} < 1$ keV while the others, $B - 3L_e$, $B - 3L_\mu$, and $B - 3L_\tau$ occur in a few keVs higher energy due to the oscillation effect. In high T_{nr} scale, their contributions are hardly distinguished from the SM case. These $U(1)'$ models give a higher spectrum than the universal vector case due to the different charges of the fermions. In general, the light mediator contributions significantly enhance the predicted rate as the recoil energy becomes smaller. These types of light mediators are then a universal way to improve measurements of low energy events. Hence, the enhanced behavior in low nuclear recoil energy is a strong indication to search for new physics in the lower energy region.

We show the 90% C.L excluded region on the coupling-mass plane from previous works in Fig.4(a), Fig.4(b), and Fig.4(c) for the universal light scalar, vector, and tensor mediator models, respectively.

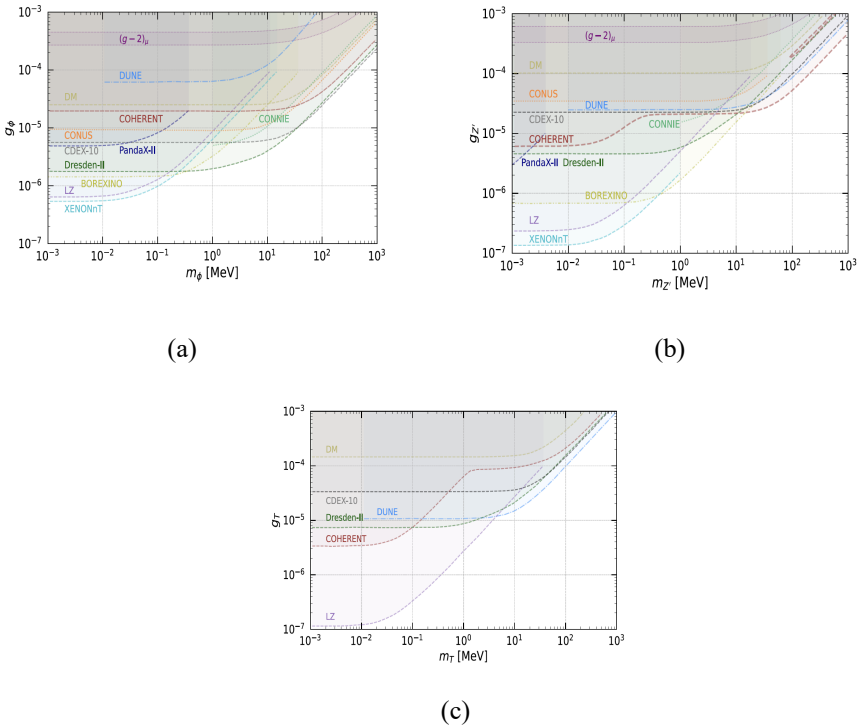


Figure 4. 90% C.L. (2 d.o.f) exclusion regions in the mass-coupling plane of the universal light (a) scalar, (b) vector, and (c) tensor mediator models

These limits are from stopped-pion (COHERENT [3, 4]), solar neutrino (BOREXINO [55]), DD (XENONnT [56], PandaX-II [57], LZ [58], CDEX-10 [59]), neutrino beam (DUNE [60]), nuclear reactor (CONNIE [6], CONUS [7], Dresden-II [61]), and collider experiments. The COHERENT limits are derived in Refs. [22, 62] with CsI and Ar targets. As for nuclear reactors, the CONNIE limit is from Ref. [63], the CONUS limit is from [64], and the Dresden-II (2σ with iron-filter quenching factor) limits are derived in [65]. We also show the limits obtained from investigating CEvNS at dark-matter experiments such as XENONnT and LZ derived in Refs. [23, 66, 67], PandaX-II derived in Ref. [68], and CDEX-10 derived in Ref. [24]. Moreover, we include limits from neutrino beam experiments from DUNE derived in Ref. [69] and from solar neutrino experiment at BOREXINO, as well as the limits of projected dark matter studies which are derived in Ref. [70] and the 2σ allowed region of the muon anomalous magnetic moment $(g-2)_\mu$ [71].

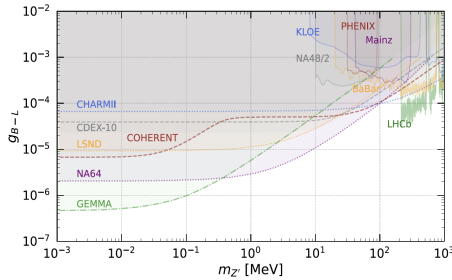


Figure 5. 90% C.L. (2 d.o.f) exclusion regions in the mass-coupling plane of the $B - L$ model

We also show available constraints in the literature on the coupling-mass plane of the $B - L$ model in Fig. 5. In addition to the previously mentioned sources, there are additional experiments regarding neutrino beam (LSND [72], CHARM-II [73], NA64 [74]), nuclear reactor (TEXONO [75], GEMMA [76]), collider (BaBar [77], LHCb [78], KLOE [79], Mainz [80], PHENIX [81]), rare-meson decay NA48/2 [82], neutrino trident (CCFR [83]), and Neutron-Lead scattering [84] experiment. The COHERENT limits are derived in Ref. [22], while the DD of dark matter of the CDEX-10 limit is derived in Ref. [24]. The LSND and CHARM-II limits are derived in Ref. [85].

We also list some of the most significant limits with 90 % C.L. for each light mediator for completeness in Table 2. Apart from the previously mentioned results, other limits listed in this

Table 2. Upper limits on the coupling constants for the light mediator models

Coupling	Experiment	Limit	Ref.
g_ϕ	COHERENT	$\lesssim 1.90 \times 10^{-5}$	[22]
	CDEX-10	$\lesssim 5.68 \times 10^{-6}$	[24]
	PandaX-II	$\lesssim 4.90 \times 10^{-6}$	[68]
	Dresden-II	$\lesssim 1.80 \times 10^{-6}$	[65]
	XENONnT	$\lesssim 5.00 \times 10^{-7}$	[66]
$g_{Z'}$	COHERENT	$\lesssim 6.08 \times 10^{-6}$	[22]
	Dresden-II	$\lesssim 4.50 \times 10^{-6}$	[65]
	PandaX-II	$\lesssim 3.20 \times 10^{-6}$	[68]
	CDEX-10	$\lesssim 2.28 \times 10^{-6}$	[24]
	XENONnT	$\lesssim 1.30 \times 10^{-7}$	[23]
g_T	CDEX-10	$\lesssim 3.35 \times 10^{-5}$	[24]
	Dresden-II	$\lesssim 6.00 \times 10^{-6}$	[65]
	COHERENT	$\lesssim 3.37 \times 10^{-6}$	[22]
	LZ	$\lesssim 1.10 \times 10^{-7}$	[66]

g_{B-L}	CDEX-10	$\lesssim 3.93 \times 10^{-5}$	[24]
	LSND	$\lesssim 9.65 \times 10^{-6}$	[72]
	COHERENT	$\lesssim 6.90 \times 10^{-6}$	[22]
	NA64	$\lesssim 2.10 \times 10^{-6}$	[74]
	GEMMA	$\lesssim 4.90 \times 10^{-7}$	[76]
	XENONnT	$\lesssim 1.60 \times 10^{-7}$	[67]
g_{B-3L_e}	COHERENT	$\lesssim 4.34 \times 10^{-5}$	[62]
	CDEX-10	$\lesssim 3.06 \times 10^{-5}$	[24]
	TEXONO	$\lesssim 2.95 \times 10^{-6}$	[86]
g_{B-3L_μ}	CCFR	$\lesssim 2.85 \times 10^{-4}$	[83]
	COHERENT	$\lesssim 2.76 \times 10^{-5}$	[62]
	CDEX-10	$\lesssim 2.76 \times 10^{-5}$	[24]
g_{B-3L_τ}	$Z_{\tau\tau}$	$\lesssim 1.00 \times 10^{-2}$	[86]
	Neutron-Lead	$\lesssim 1.00 \times 10^{-4}$	[84]
	CDEX-10	$\lesssim 2.84 \times 10^{-5}$	[24]

table are from TEXONO (for g_{B-3L_e}), from CCFR (for g_{B-3L_μ}), as well as from Neutron-Lead scattering process and one-loop vertex correction to the $Z_{\tau\tau}$ coupling (for g_{B-3L_τ}), all derived in Ref. [86]. It is clear that the neutrino-electron scatterings in the solar neutrino experiment of BOREXINO and DD dark matter experiments of XENONnT and LZ dominate the low mass region as $m_x \lesssim 0.1$ MeV. For the DD experiment, bound from the neutrino-nucleus process (CDEX-10) has approximately two orders of magnitude less tight constraint than those from neutrino-electron scattering. This is due to larger pp flux and to the kinematic constraint in which electron mass is much smaller than nucleus mass, allowing for higher recoil energies. Meanwhile, other limits from reactors (CONNIE, CONUS, and Dresden-II), neutrino beam (DUNE), and stopped-pion (COHERENT) neutrino sources dominate in the high-mass region due to higher neutrino energy. The development of next-generation experiments will provide updates regarding the current limits.

4. CONCLUSION

We reviewed the process of CEvNS in the SM and possible BSM extensions of light mediator models. We explained the standard differential cross-section of the process with the form factor effect. The role of the quenching factor in obtaining the differential event rate has also been discussed. We further reviewed the new physics of light mediator models from universal scalar, vector, and tensor, as well as possible $U(1)'$ extensions. For some benchmark points, we showed the predicted effects of the light mediators on the CEvNS concerning solar neutrino flux with

different nucleus targets. Finally, we provided various limits derived from previous works. Results from DM direct detection experiments indicate stringent constraints on the light mediator parameters due to their lower recoil energy thresholds, originated from the low energy of the detected neutrino. In summary, CEvNS is currently one of the most active subjects in particle physics subjects and can be used as a testing ground for the SM weak physics as well as in searching for the BSM signatures. Further astounding breakthroughs concerning this topic might be ahead in the upcoming years.

REFERENCES

- [1] D. Z. Freedman, Phys. Rev. D 9, 1389 (1974).
- [2] D. Akimov et al. (COHERENT), Science 357, 1123 (2017).
- [3] D. Akimov et al. (COHERENT), Phys. Rev. Lett. 126 012002, (2021).
- [4] D. Akimov et al. (COHERENT), Phys. Rev. Lett. 129, 081801 (2022).
- [5] J. Colaresi, et al. Phys. Rev. Lett. 129, 211802 (2022).
- [6] A. Aguilar-Arevalo et al. [CONNIE], JINST 11 (2016), P07024.
- [7] H. Bonet et al. (CONUS), Phys. Rev. Lett. 126, 041804 (2021).
- [8] D. Huang et al. (PandaX), Phys. Rev. Lett. 131, 191002 (2023).
- [9] E. Aprile et al. (XENON), Phys. Rev. Lett. 131, 041003 (2023).
- [10] Z. Bo et al. (PandaX), arXiv:2407.10892 [hep-ex] (2024).
- [11] E. Aprile et al. (XENON), arXiv:2408.02877 [nucl-ex] (2024).
- [12] G. Angloher et al. (NUCLEUS), Eur. Phys. J. C 79, 1018 (2019).
- [13] D. Baxter, et al., JHEP 02, 123 (2020).
- [14] M. Cadeddu, et al., Phys. Rev. D 101, 033004 (2020).
- [15] M. Atzori Corona et al., Eur. Phys. J. C 83 (2023), 683.
- [16] C. Giunti and A. Studenikin, Rev. Mod. Phys. 87, 531 (2015).
- [17] A. N. Khan, Nucl. Phys. B 986, 116064 (2023).
- [18] L. J. Flores, N. Nath and E. Peinado, Phys. Rev. D 105, 055010 (2022).
- [19] C. Giunti, Phys. Rev. D 101, 035039 (2020).
- [20] M. F. Mustamin and M. Demirci, Braz. J. Phys. 51, 813-819 (2021).
- [21] C. Boehm, D. G. Cerdeno, M. Fairbairn, P. A. N. Machado and A. C. Vincent, Phys. Rev. D 102, 115013 (2020).
- [22] V. De Romeri, et al., JHEP 04, 035 (2023).
- [23] A. N. Khan, Phys. Lett. B 837, 137650 (2023).

- [24] M. Demirci and M. F. Mustamin, Phys. Rev. D 109, 015021 (2024).
- [25] P. Coloma, et al., JHEP 08, 030 (2020).
- [26] G. Herrera, JHEP 05, 288 (2024).
- [27] M. Abdullah, D. Aristizabal Sierra, B. Dutta, and L. E. Strigari, Phys. Rev. D 102, 015009 (2020).
- [28] K. Scholberg (COHERENT), PoS NuFact2017, 020 (2018).
- [29] S. Navas et al. (PDG), Phys. Rev. D 110, 030001 (2024).
- [30] S. Klein and J. Nystrand, Phys. Rev. C 60 (1999), 014903.
- [31] J. Piekarewicz et al., Phys. Rev. C 94 (2016), 034316.
- [32] R. H. Helm, Phys. Rev. 104, 1466-1475 (1956).
- [33] J. Lindhard, et al., Kgl. Danske Videnskab., Selskab. Mat. Fys. Medd. 33, 1, (1963).
- [34] A. Bonhomme, et al., Eur. Phys. J. C 82, 815 (2022).
- [35] Y. Sarkis, A. Aguilar-Arevalo and J. C. D'Olivo, Phys. Rev. D 101 (2020), 102001.
- [36] J. I. Collar, A. R. L. Kavner and C. M. Lewis, Phys. Rev. D 103 (2021), 122003.
- [37] Y. Fukuda et al. (Super-Kamiokande Collaboration), Phys. Rev. Lett. 81, 1562-1567 (1998).
- [38] Q. R. Ahmad et al. (SNO Collaboration), Phys. Rev. Lett. 87, 071301 (2001).
- [39] Q. R. Ahmad et al. (SNO Collaboration), Phys. Rev. Lett. 89, 011301 (2002).
- [40] C. D. McCoy, and M. Massimi, Euro. J.Phil. Sci. 8, 99–123 (2018).
- [41] D. G. Cerdeño, et al., JHEP 05, 118 (2016) [JHEP 09, 048 (2016)].
- [42] J. Barranco, et al., Int. J. Mod. Phys. A 27, 1250147 (2012).
- [43] M. Cirelli, E. Del Nobile and P. Panci, JCAP 10, 019 (2013).
- [44] R. Harnik, J. Kopp and P. A. N. Machado, JCAP 07 (2012), 026.
- [45] W. Buchmuller, C. Greub and P. Minkowski, Phys. Lett. B 267, 395-399 (1991).

- [46] A. Alves, et al., Phys. Rev. D 92, 083004 (2015).
- [47] B. Allanach and A. Mullin, JHEP 09, 173 (2023).
- [48] R. N. Mohapatra and J. C. Pati, Phys. Rev. D 11, 566-571 (1975).
- [49] R. N. Mohapatra and J. C. Pati, Phys. Rev. D 11, 2558 (1975).
- [50] A. Davidson, Phys. Rev. D 20, 776 (1979).
- [51] R. N. Mohapatra and R. E. Marshak, Phys. Rev. Lett. 44, 1316-1319 (1980) [erratum: Phys. Rev. Lett. 44, 1643 (1980)].
- [52] E. Ma, Phys. Lett. B 433, 74-81 (1998).
- [53] E. Ma and U. Sarkar, Phys. Rev. Lett. 80, 5716-5719 (1998).
- [54] L. N. Chang, et al., Phys. Rev. D 63, 074013 (2001).
- [55] G. Bellini et al. (Borexino), Phys. Rev. D 82, 033006 (2010).
- [56] E. Aprile et al. (XENON), Phys. Rev. Lett. 129, 161805 (2022).
- [57] X. Zhou et al. (PandaX-II), Chin. Phys. Lett. 38, 011301 (2021).
- [58] D. S. Akerib et al. (LZ), Phys. Rev. D 101, 052002 (2020).
- [59] X. P. Geng et al. (CDEX), Phys. Rev. D 107, 112002 (2023).
- [60] B. Abi et al. (DUNE), Eur. Phys. J. C 80, 978 (2020).
- [61] J. Colaresi, et al., Phys. Rev. D 104, 072003 (2021).
- [62] M. Atzori Corona, et al., JHEP 05, 109 (2022).
- [63] A. Aguilar-Arevalo et al. (CONNIE), JHEP 04, 054 (2020).
- [64] H. Bonet et al. (CONUS), JHEP 05 (2022), 085.
- [65] D. A. Sierra, V. De Romeri and D. K. Papoulias, JHEP 09, 076 (2022).
- [66] S. K. A. et al., Phys. Lett. B 839, 137742 (2023).
- [67] V. De Romeri, D. K. Papoulias and C. A. Ternes, JHEP 05, 165 (2024).
- [68] A. N. Khan, Phys. Lett. B 819, 136415 (2021).
- [69] P. Melas, D. K. Papoulias and N. Saoulidou, JHEP 07, 190 (2023).
- [70] A. Majumdar, D. K. Papoulias and R. Srivastava, Phys. Rev. D 106, 013001 (2022).

- [71] D. P. Aguillard et al., Phys. Rev. Lett. 131, 161802 (2023).
- [72] L. B. Auerbach et al. (LSND), Phys. Rev. D 63, 112001 (2001).
- [73] P. Vilain et al. (CHARM-II), Phys. Lett. B 345, 115-118 (1995).
- [74] Y. M. Andreev et al. (NA64), Phys. Rev. Lett. 129, 161801 (2022).
- [75] M. Deniz et al. (TEXONO), Phys. Rev. D 81, 072001 (2010).
- [76] A. G. Beda, et al., Phys. Part. Nucl. Lett. 7, 406-409 (2010).
- [77] J. P. Lees et al. (BaBar), Phys. Rev. Lett. 113, 201801 (2014).
- [78] R. Aaij et al. (LHCb), Phys. Rev. Lett. 124, 041801 (2020).
- [79] B. Abelev et al. (ALICE), Phys. Lett. B 720, 52-62 (2013).
- [80] H. Merkel et al. (A1), Phys. Rev. Lett. 106, 251802 (2011).
- [81] A. Adare et al. (PHENIX), Phys. Rev. C 91, 031901 (2015).
- [82] J. R. Batley et al. (NA48/2), Phys. Lett. B 746, 178-185 (2015).
- [83] S. R. Mishra et al. (CCFR) Phys. Rev. Lett. 66, 3117-3120 (1991).
- [84] R. Barbieri and T. E. O. Ericson, Phys. Lett. B 57, 270-272 (1975).
- [85] W. Altmannshofer, S. Gori, M. Pospelov and I. Yavin, Phys. Rev. Lett. 113, 091801 (2014).
- [86] J. Heeck, M. Lindner, W. Rodejohann and S. Vogl, SciPost Phys. 6, 038 (2019).

NÖRODEJENERATİF HASTALIKLarda KAN ÖRNEKLERİNİN FOURIER DÖNÜŞÜM INFRARED (FTIR) SPEKTROSKOPİSİ İLE İNCELENMESİ

Çisem ALTUNAYAR ÜNSALAN¹

1. GİRİŞ

Nörodejeneratif hastalıklar insan sağlığı için büyük bir tehdit oluşturmaktadır. Yaşa bağlı bu bozukluklar, kısmen yaşlı nüfusun son yıllarda artması nedeniyle giderek daha yaygın hale gelmektedir. Nörodejeneratif hastalıklara örnek olarak Alzheimer hastalığı, Parkinson hastalığı, Huntington hastalığı, amyotrofik lateral skleroz, frontotemporal demans ve spinoserebellar ataksi verilebilir. Bu hastalıklar patofizyolojilerinde çeşitlilik gösterir; bazıları hafiza ve bilişsel bozukluklara neden olurken diğerleri kişinin hareket etme, konuşma ve nefes alma yeteneğini etkiler (Gitler vd., 2017).

Neredeyse tüm nörodejeneratif hastalıkların ortak bir özelliği, sonuçlarının genellikle yıkıcı olması ve ciddi zihinsel ve fiziksel etkilere sahip olmasıdır. Bu büyük ölçüde nöronların kaybı veya işlev bozukluğundan kaynaklanır. Bir nöron bir kez kaybedildiğinde, ilişkili işleviyle birlikte genellikle sonsuza dek kaybolur (Cannon ve Greenamyre, 2011).

Şu anda nörodejeneratif hastalıklar tedavi edilemez durumdadır ve mevcut tedaviler yalnızca semptomları yönetir veya hastalığın ilerlemesini durdurur. Bu nedenle, Dünya Sağlık Örgütü'nün motor fonksiyonunu etkileyen nörodejeneratif hastalıkların öümüzdeki 20 yıl içinde ikinci en yaygın ölüm nedeni olacağını öngörmesi nedeniyle bu tür hastalıklar için yeni tedavilere acil ihtiyaç bulunmaktadır (Duræs vd., 2018).

Hastalıkların varlığını doğrulamak ve ayrıca uygun yönetim ve tedaviyi sağlamak için doğru, ancak aynı zamanda ucuz ve minimal invaziv bir tanı testine acilen ihtiyaç duyulmaktadır (Paraskevaidi vd.,

¹ Arş. Gör. Dr., Ege Üniversitesi, Fen Bilimleri Enstitüsü, cisemaltunayar@gmail.com, ORCID: 0000-0001-6479-4223.

2017). Kan bazlı testler büyük olasılıkla nörodejeneratif hastalık riski taşıyan büyük popülasyonların gelecekte hassas bir şekilde taraması için bir ön koşul ve buna yönelik teşhis yaklaşımında bir temel oluşturacağından, mevcut yöntemleri kullanarak bu tür klinik örneklerin analizine odaklanmak gereklidir (Habartová vd., 2019).

Spektroskopik yaklaşımlar kullanılarak kolayca toplanan biyosıvıların örneklenmesi, tanı prosedürlerini entegre etmek ve iyileştirmek için tıbbi alanda giderek daha fazla ilgi görmektedir (Condino vd., 2023). Fourier dönüşüm infrared (FTIR) spektroskopisi, hastalık teşhisinde sıkılıkla kullanılan, yüksek oranda tekrarlanabilir, gerçekleştirilmesi kolay ve küçük örnek hacimleriyle çalıştırılması mümkün bir tekniktir. Elde edilen infrared spektrum, aynı anda karbohidratlar, nükleik asitler, proteinler ve lipitler hakkında metabolik bilgi sağlar ve özellikle kanser ve nörodejeneratif durumlar gibi çok faktörlü hastalıklar için faydalıdır (Martins vd., 2024).

Bu çalışmanın amacı, bazı nörodejeneratif hastalıklarda ayrımları aracı olarak kan örneklerinin Fourier dönüşüm infrared (FTIR) spektroskopisi ile incelenerek tanısal potansiyelini karşılaştırmak ve değerlendirmektir.

2. GENEL BİLGİLER

2.1. Nörodejeneratif Hastalıklar

Nörodejenerasyon nöronal yapı ve işlev kaybını tanımlar. Yaklaşık olarak son 100 yılda, nörodejenerasyon ve nörolojik bozukluklar arasındaki bağlantı kapsamlı bir şekilde tanımlanmıştır. 1892 gibi erken bir tarihte, Bloq ve Marinesco, yakın zamanda keşfedilen karmin boyasını kullanmış ve yaşlı bir epileptik hastada plaklarda bilinmeyen bir maddenin anormal bir şekilde birliğini bulmuşlardır. 1900'lerin başında nöronal yapı ve işlev kaybını nörolojik bozukluklarla ilişkilendiren iki önemli bulgu elde edilmiştir. 1907'de Fischer, 16 yaşlılık bunaması vakasının 12'sinde nöropatolojik değişiklikler bularak plak oluşumunu kapsamlı bir şekilde tanımlamış, ancak 45 ilerleyici felç vakasında, 19 fonksiyonel psikoz vakasında ve 10 normal kontrol deneklerinde bu değişiklikleri bulamamıştır. Aynı yıl tek bir vakada, Alman hekim ve patolog Alois Alzheimer, 51 yaşında ciddi şekilde bunamış bir kadının beynindeki nöronlarda nörofibriler düğümlerin varlığını ayrıntılı olarak tanımlamıştır. Alzheimer ayrıca Fischer tarafından gözlemlenen plakları da kaydetmiştir. Yaklaşık on yıl sonra,

belirli bölgesel nöronal hücre kaybı nörolojik sekellere bağlanmıştır. Parkinson hastalığında 1919'da hastalarda titreme ve rijiditenin substantia nigra'daki hücre kaybıyla ilişkili olduğu bulunmuştur (Cannon ve Greenamyre, 2011).

Nörodejeneratif hastalıklar klinik olarak sinsi başlangıcıları ve kronik ilerlemeleriyle karakterize edilir ve patolojik olarak sıklıkla belirli sinir sistemini etkileyen ilerleyici işlev bozukluğu ve hücre ölümüyle karakterize edilir. Morfolojik olarak nöronal kayıp gliyozisle ve sıklıkla proteinlerin yanlış katlanması ve kümelenmesiyle ilişkilidir ve bu da belirli hücre tiplerinde anormal ekstraselüler ve intraselüler filamentli birikintilerin durmaksızın birikmesine yol açar ve birçok nörodejeneratif bozukluğun temel özelliklerini/ayırt edici özelliklerini temsil eder (Chen vd., 2012).

Alzheimer hastalığı (AD), Parkinson hastalığı (PD), frontotemporal demans (FTD) ve amyotrofik lateral skleroz (ALS), kaçınılmaz olarak ciddi sakatlığa ve ölüme ilerleyen yıkıcı nörodejeneratif bozukluklardır. Birçok kişide bu nörodejeneratif bozuklukların net bir genetik nedeni olmasa da, alan bu bozuklukları kesin olarak yönlendiren mutasyona uğramış genlerin ve riski değiştiren genetik varyantların keşfiyle yönlendirilmiştir. Bu genetik kılavuzlar, amiloid- β (A β), α -sinüklein, tau ve TDP-43 gibi bu hastalıkların patolojik özelliklerini tanımlayan proteinlerin biyokimyasal olarak tanımlanmasıyla birlikte, nörodejeneratif bozuklukların patofizyolojisi hakkında temel bilgiler sağlamıştır (Dawson vd., 2018).

Oksidatif stres yaşlanma ve çeşitli nörolojik bozukluklarda düzenleyici bir unsur olarak önerilmektedir. Oksidanların fazlalığı antioksidanların azalmasına neden olur ve bu da organizmalarda oksidasyon-redüksiyon dengesizliği üretir. Antioksidan sisteminin yetersizliği, reaktif türlerin (oksijen, hidroksil serbest radikalı vb.) yüksek seviyeleriyle karakterize edilen oksidatif strese neden olur. Mitokondriler, oksidatif fosforilasyon yoluyla hücrelere ATP tedarikinde ve temel biyolojik moleküllerin sentezinde önemli bir rol oynar. Oksidatif fosforilasyon sürecinde enzimler tarafından katalize edilen çeşitli redoks reaksiyonları gerçekleşir. Verimsiz bir oksidatif fosforilasyon, mitokondriyal disfonksiyona yol açan reaktif oksijen türleri (ROS) üretebilir. Mitokondriyal redoks metabolizması, fosfolipit metabolizması ve proteolitik yolların serbest radikallerin başlıca ve potansiyel kaynağı

olduğu bulunmuştur. Normal hücresel sinyalleme için düşük ROS konsantrasyonu gereklidir, oysa ROS'un yüksek konsantrasyonu ve uzun süreli maruziyeti DNA, lipitler ve proteinler gibi hücresel makromoleküllere zarar vererek sonuçta nekroz ve apoptotik hücre ölümüne yol açar. Merkezi sinir sisteminin (CNS) normal ve düzgün çalışması tamamen beynin kimyasal bütünlüğüne bağlıdır. Beynin büyük miktarda oksijen tükettiği ve lipit içeriği bakımından oldukça zengin olduğu ve oksidatif stresre yatkın hale geldiği iyi bilinmektedir. Yüksek oksijen tüketimi aşırı ROS üretimine yol açar. Bunun dışında nöronal zarların ROS'a oldukça duyarlı olan çoklu doymamış yağ asitleri bakımından zengin olduğu bulunmuştur. Parkinson hastalığı (PD), Alzheimer hastalığı (AD), Huntington hastalığı (HD) ve amyotrofik lateral skleroz (ALS) gibi çeşitli nörodejeneratif hastalıklar, biyomoleküler bileşenlerde biyokimyasal değişimin (oksidatif stres nedeniyle) sonucu meydana gelebilmektedir (Singh vd., 2019).

2.2. Fourier Dönüşüm Infrared (FTIR) Spektroskopisi

Fourier Dönüşüm Infrared (FTIR), kıızılıötesi radyasyonun absorbansını, geçirgenliğini veya yansımاسını kullanan bir titreşim spektroskopisi biçimidir. İşık, numune tarafından farklı frekanslarda farklı miktarlarda emilir; bu frekanslar, numunedeki bağların titreşim frekanslarına karşılık gelir. FTIR dipol momentindeki değişime bağlıdır ve bir numunenin radyasyonu emdiği mutlak frekansları ölçer. Ayrıca, FTIR hetero nükleer fonksiyonel grup titreşimlerine ve polar bağlara, özellikle suda OH gerilmesine duyarlıdır (Lopes vd., 2016).

IR spektral bölgesi, yaklaşık olarak 780 nm'deki görünür spektrumun kırmızı ucundan (dalga sayısı: 12820 cm^{-1}) 1 mm'lik bir dalga boyundaki mikrodalga bölgesinin başlangıcına (10 cm^{-1}) kadar uzanır. IR aralığı ayrıca yakın kıızılıötesi (NIR), orta kıızılıötesi (MIR) ve uzak kıızılıötesi (FIR) bölgelerine ayrılır. MIR, $4000\text{-}400 \text{ cm}^{-1}$ aralığını kapsar ve özellikle $1500\text{-}600 \text{ cm}^{-1}$ 'de (parmak izi bölgesi) genellikle moleküler türlerin parmak izi özelliklerini sağlayan bölgedir (Lopes vd., 2016).

Fourier Dönüşüm Infrared (FTIR) spektroskopisi, kıızılıötesi ışıkla etkileşime girdiğinde örneklerdeki kimyasal bağların titreimsel geçişlerine dayalı olarak biyolojik örneklerin moleküler parmak izlerini sağlayan umut verici bir tekniktir. Parmak izi bölgesi (IR spektrumunun 1500 cm^{-1} 'in altındaki bölümü), hastalığın başlangıcı ve ilerlemesi

sırasında meydana gelen metabolik değişiklikler hakkında çok miktarda değerli bilgi içeren, bir örneğe özgü karakteristik bir emilim desenini içeren karmaşık bir alandır (Tkachenko vd., 2022).

FTIR, tanı aracı olarak potansiyeli konusunda önemli ve devam eden bir araştırma geçmişine sahiptir ve çok çeşitli örnek tiplerinin son derece hızlı, yüksek verimli ve tahribatsız analizine olanak tanır. Ayrıca, minimum miktarda örnek hazırlama ile karbohidratları, amino asitleri, yağ asitlerini, lipitleri, proteinleri, nükleik asitleri ve polisakkaritleri aynı anda analiz edebildiği için metabolik parmak izi için değerli bir araç olarak kabul edilmiştir. Ayrıca, FTIR diğer yöntemlere göre daha az maliyetli ve daha doğrudur (Lopes vd., 2016).

IR, kan gibi vücutun çeşitli fizyolojik fonksiyonlarını yansitan ve kolayca elde edilebilen insan biyosivlarını analiz etmek için özellikle uygundur. Kan, tüm organizma boyunca metabolitlerin birincil taşıyıcısıdır ve esas olarak proteinler, lipitler ve şekerler olmak üzere çeşitli biyolojik materyallerden oluşur. Bunların hepsi kıızılıotesi aralıktı aktiftir ve her biyomolekül kendine özgü yapısıyla belirlenir. İzole edilmiş moleküller incelemek yerine kimyasal yapılarındaki değişiklikler eş zamanlı olarak araştırılabilir. Böylece, FTIR tarafından biyolojik bir numuneden kaydedilen spektrum, özgüllüğünü yansitan benzersiz bir IR spektral imza üretir. Dahası, plazmanın IR spektral modları organizmanın mevcut durumunu yansıtabilir ve hastalığın varlığı veya yokluğuyla doğrudan ilişkilendirilebilir (Tkachenko vd., 2022).

Kan gibi biyosivların FTIR spektrumu zengin bir biyolojik bilgi içerir ve numunenin/hastanın durumunun parmak izi benzeri biyokimyasal anlık görüntüsü olarak görülebilir. Biyolojik numuneler için IR spektrumundaki en önemli bölgeler, amid I ve II bantlarının görüldüğü bölgeyi ($1700-1500\text{ cm}^{-1}$) ve O-H, S-H, C-H ve N-H bağlarından kaynaklanan gerilme titreşimlerinin görülebildiği daha yüksek dalga sayısı bölgelerini ($3500-2550\text{ cm}^{-1}$) içeren parmak izi bölgeleridir ($1800-900\text{ cm}^{-1}$). Buna ek olarak, FTIR spektrumu biyosivlardaki proteinlerin ikincil yapıları hakkında da bilgi sağlayabilir; örneğin, Amid I ve II bandının konumu, proteinlerin α -helisel veya β -tabaka yapılarını belirlemek için kullanılabilir. Biyosivları nitel ve nicel olarak karakterize etme yeteneği, klinik bir bağlamda son derece değerlidir, çünkü örnekler insan vücudundaki iç organlarla etkileşime giren karbohidratlar, lipitler, nükleik asitler ve proteinler gibi çeşitli

biyomoleküller içerir. Bu biyomoleküller temelde fizyolojik ortamlarından etkilenen bir yapı ve işlevsel ilişkiyi paylaşır ve patolojileri teşhis etmek ve hastalık ilerlemesini ve tedavi terapötiklerini izlemek için kullanılabilen biyobelirteçler olarak ele alınabilir (Theakstone vd., 2021).

Kandan türetilen biyosiviların ve FTIR spektroskopisinin potansiyel bir klinik tanı aracı olarak kullanımı çok çeşitli hastalıklarda araştırılmıştır. FTIR spektroskopisi, küçük hacimli biyolojik örneklerden lipitlerin, proteinlerin ve karbonhidratların spektral imzalarını hızlı, uygulanması kolay ve uygun maliyetli bir şekilde ve yüksek tekrarlanabilirlikle sağlar. Bu nedenle, bu metodoloji, ek klinik değerlendirme testleriyle takip edilecek kişileri belirlemek için ilk tarama yaklaşımı olarak uygulanmaya uygundur (Martins vd., 2020).

3. SONUÇ

3.1. Alzheimer Hastalığı

Habartová ve ark. (2019), demanslı olmayan yaşlı 29 kişi ile Alzheimer hastalığına sahip 35 kişinin kan plazmalarındaki biyomoleküllerin yapısal değişikliklerini tespit etmek ve Alzheimer hastalığı ile ilişkili metabolitleri tanımlamak için Fourier Dönüşüm Infrared (FTIR) spektroskopisi kullanmıştır. IR spektrumları, sırasıyla amid I'deki C=O gerilmesinden ve amid II bölgelerindeki N-H büükümesi ve C_α-N gerilmesinin birlleşiminden kaynaklanan 1647 ve 1545 cm⁻¹'de iki belirgin bant göstermiştir. Protein sekonder yapısının türü ve içeriği, bu iki bandın şiddetini ve şeklini önemli ölçüde etkilemektedir. Daha düşük mutlak şiddetin yanı sıra Alzheimer hastalığına sahip kişiler ile demanslı olmayan yaşlı kişiler arasındaki bu iki spektral bandın göreceli şiddetindeki farkın, plazmatik proteinlerin/peptitlerin içeriğindeki ve sekonder yapısındaki değişikliklere işaret etmektedir. Şiddet azalma eğilimi, örneğin 1456 cm⁻¹ (fosfolipitlerin ve protein yan zincir kısımlarının CH₂ ve CH₃ büükümesi) ve 1240–1400 cm⁻¹ (fosfolipitlerin proteinlerin COO⁻ gerilmesiyle ve kolesterolle örtüşmesi) için de gözlemlenmiştir (Habartová vd., 2019).

Martins ve ark. (2024), Alzheimer hastalığında (AD) tanı potansiyeli olarak, serum veya plazmadan izole edilen kandan türetilen hücre dışı veziküler (EV) FTIR spektroskopisi ile incelenmiştir. Kontrol ve Alzheimer hastalarının serum ve plazmalarından türetilen hücre dışı vezikülerinin spektrumları üç FTIR spektral bölgesinde (1200–900 cm⁻¹, 1720–1490 cm⁻¹ ve 3050–2800 cm⁻¹) analiz edilmiştir. Analiz edilen

FTIR spektroskopik bölgeleri göz önüne alındığında, esas olarak 1200–900 cm⁻¹ bölgesi karbohidratlara ve nükleik asitlere, 1720–1490 cm⁻¹ bölgesi proteinlerdeki içerik ve konformasyona ve 3000–2800 cm⁻¹, 1770–1720 cm⁻¹ ve 1490–1430 cm⁻¹ bölgeleri ise esas olarak lipitlere karşılık gelmiştir. Serum ve plazmadan elde edilen hücre dışı veziküllerinin spektrum profilleri birbirine benzer ve aynı piklere sahiptir. Ancak, kontrol ve AD vakalarının spektrumları arasındaki absorbanslar karşılaşıldığında, farklı spektrum bölgelerinde (1200–900 cm⁻¹, 1720–1490 cm⁻¹, 3050–2800 cm⁻¹) bazı farklı desenler bulunmuştur. 1200–900 cm⁻¹ bölgesi daha detaylı analiz edildiğinde, plazmadan türetilen hücre dışı veziküllerin spektrumlarının ikinci türevi elde edilmiş ve 4 pikin alanı hesaplanmıştır. Bunlar, 1011 cm⁻¹ (osidik ve protein yapılarında v(C=O); dianyonik fosfat monoesterinin (nükleik asitler, DNA) v_s'si), 1039 cm⁻¹ (v(C=O) RNA'daki ribozda), 1064 cm⁻¹ (ester (fosfolipitler) simetrik gerilme titresimi (v_s) (C—O—C); ribozdaki (nükleik asitler) v(C=O)) ve 1146 cm⁻¹ (Glikojen; gerilme titresimi (v)(C=O) ve v(C—C); C—O—H deformasyonu (karbonhidratlar)) karşılık gelmektedir. Öte yandan, 3 pikin alanı (1039 cm⁻¹, 1064 cm⁻¹ ve 1146 cm⁻¹) AD vakalarının plazmadan türetilen hücre dışı veziküllerinin spektrumlarında ölçüde azalmıştır. Kontrollerin serumdan türetilen hücre dışı veziküller ile karşılaşıldığında AD vakaları için 1146 cm⁻¹ pik alanında önemli bir azalma bulunmuştur (Martins vd., 2024).

Paraskevaidi ve ark. (2017), AD'yi ve erken AD hastalarını sağlıklı kontrol (HC) bireylerden ayırmak ve daha kesin bir klinik tanıya yardımcı olacak anlamlı biyobelirteçler belirlemek amacıyla, zayıflatılmış toplam yansımı FTIR (ATR-FTIR) spektroskopisini kullanarak kan plazması örneklerini incelemiştir. 1800–900 cm⁻¹ parmak izi bölgesi ve 3700–2800 cm⁻¹ bölgesi göz önüne alınmıştır. Parmak izi bölgesinde, AD grubu 1650–1630 cm⁻¹'de [(C=O)'nun gerilme titresimi (v), Amid I, proteinler] ve 1540–1530 cm⁻¹'de [(N-H)'ın eğilme titresimi (δ), Amid II, proteinler], 1750–1735 cm⁻¹'de daha düşük pikler [lipitlerin v(C=O)], 1590–1580 cm⁻¹ [Amid II'nin δ(N-H), proteinler], 1470–1430 cm⁻¹ [lipitlerin δ(CH₃) ve δ(CH₂)'si ve proteinler], 1220–1160 cm⁻¹ [karbohidratlar, DNA/RNA'nın PO₂⁻ asimetrik gerilmesi (v_{as})] ve 1150–1040 cm⁻¹ [karbonhidratlar ve DNA/RNA'nın PO₂⁻'sının simetrik gerilmesi (v_s)] gözlenmiştir. AD grubu için 2950–2850 cm⁻¹'de daha düşük pikler [lipitlerin vs(CH₂)'si] ve 3550–3450 cm⁻¹'de biraz daha yüksek pikler [v(–OH)] gözlenmiştir (Paraskevaidi vd., 2017).

Martins ve ark. (2020), iki ayrı grubun kontrol ve AD vakalarından elde edilen serumdan türetilen ekzosomları FTIR spektroskopisi ile araştırmıştır. FTIR analizi için, serum ve serumdan türetilen ekzosomlar iki ayrı kohorttan (UA-Kohortu ve UMG-Kohortu) kontrollerden ve AD vakalarından izole edilmiştir. Serum ve serumdan türetilen ekzosomların spektrum profili her iki kohortta da benzer olarak gözlenmiştir. Serum ve serumdan türetilen ekzosomlar, $4000-600\text{ cm}^{-1}$ bölgelerinde analiz edilmiştir. Her fonksiyonel grup, farklı bir dalga boyunda kızılıtesi radyasyonu emmesi sonucu proteinler, amino asitler, lipitler, karbonhidratlar ve DNA/RNA gibi farklı bileşiklerin varlığına karşılık gelen ana spektroskopik bölgeler tanımlanmıştır. $1700-1472\text{ cm}^{-1}$ aralığındaki protein katkılara ilişkin olarak, $1636-1634\text{ cm}^{-1}$ (amid I) ve $1534-1526\text{ cm}^{-1}$ 'deki (amid II) emilim pikleri serum örneklerinde serumdan türetilen ekzosomlara göre daha belirgindir ve bu, ilkindeki daha yüksek protein miktarını yansıtır. Bununla birlikte, ekzosom spektrumları, fenil halkalarının düzlemsel büükümesi arasında düzlemsel N-H büükümesine ve amid II'nin aminoasitlerinin C-N gerilmesine atanabilen 1509 cm^{-1} 'de ek bir pik göstermiş ve bu, yüksek konsantrasyonlarda serbest amino asitlerin varlığını yansıtmıştır. Her iki numunenin lipitleriyle ilişkili spektroskopik sinyaller $3000-2800\text{ cm}^{-1}$, $1760-1720\text{ cm}^{-1}$, $1483-1423\text{ cm}^{-1}$ ve $1469-1404\text{ cm}^{-1}$ aralığındadır. Ekzosomlar, $3000-2800\text{ cm}^{-1}$ ve $1483-1423\text{ cm}^{-1}$ lipidik bölgelerinde serum spektrumlarından daha yüksek absorbansa sahiptir ve bu, ekzosomlardaki lipidik bileşimi yansıtır. Bununla birlikte, serum ve serumdan türetilen ekzosomların absorbans spektrumlardaki temel fark, nükleik asitlerin ve karbohidratların varlığıyla ilişkili olan $1200-900\text{ cm}^{-1}$ bölgесindedir; burada ekzosom spektrumlarda belirgin bir pik 1064 cm^{-1} 'de gözlemlenmiştir; ester C-O-C fosfolipitlerin simetrik gerilmesine ve/veya riboz C-O gerilmesine (nükleik asitler) karşılık gelmektedir (Martins vd., 2020).

Carmona ve ark. (2012) Alzheimer hastalığına sahip hastalardan alınan periferik kan mononükleer lökositleri FTIR spektroskopisi ile analiz etmiş ve spektroskopik özellikleri sağlıklı kontrollerle karşılaştırmıştır. Sağlıklı kontrollerin ve orta şiddette AD'den etkilenen hastaların amid I bant ortalama spektrumlarını göz önüne alındığında, en belirgin spektral farkın protein β yapısının genellikle göründüğü yaklaşık $1640-1625\text{ cm}^{-1}$ aralığında meydana geldiği belirtilmiştir. Amid I konturu altındaki örtüsen bant bileşenlerini belirlemek için, karşılık gelen ikinci

türev spektrumları hesaplanmıştır. AD spektrumunda, sağlıklı kontrollere göre 1631 cm^{-1} 'in daha yüksek şiddetli olması, AD beyin dokusundan alınan infrared spektrumlarına dayanarak amiloid β -tabaka yapılarının oluşumunu göstermektedir. AD sırasında 1638 cm^{-1} bandının artan şiddeti ise, $1641\text{--}1625\text{ cm}^{-1}$ aralığında kümelenen amid I titreşim modları üreten β -tabaka proteinlerine karşılık gelmektedir. AD durumunda 1638 ve 1631 cm^{-1} şiddet artışı, farklı frekansları β -tabaka yapılarının farklı özelliklerine özgü olan β -tabaka proteinlerine ve amiloid peptitlerine karşılık gelmektedir. Tüm bu sonuçlar AD lökositlerine özgü ortaya çıkan bantların AD için potansiyel biyobelirteçleri olabileceği ortaya konulmuştur (Carmona vd., 2013).

3.2. Parkinson Hastalığı

Ahmed ve ark. (2010) Parkinson hastalığının (PD)'nin izlenmesi ve tanımlanması için biyobelirteç görevi gören spektral parametreleri tespit etmek amacıyla 69 sağlıklı ve 61 ilaçsız PD hastasının insan plazma örneklerini analiz etmek için Fourier dönüşüm infrared (FTIR) mikro spektroskopı analizi uygulamıştır. 1078 , 1169 , 1244 ve 3060 cm^{-1} 'deki bantlar kontrol grubuya karşılaştırıldığında evre 1 PD'de değişmiş ve 689 , 1078 , 1169 ve 1244 cm^{-1} 'deki spektral bölgelerdeki değişimler evre 2 PD'de tanımlanmıştır. Benzer şekilde, bant şiddetlerindeki fark evre 3 PD için kontrolleriyle karşılaştırıldığında 1078 , 1169 , 1244 , 1542 , 2930 , 2953 , 3293 ve 3296 cm^{-1} 'de fark edilmiştir. 1078 , 1169 ve 1244 cm^{-1} 'deki örtüşmesi, hastalık evre 1 'den 3 'e ilerledikçe emilim şiddetlerinde sistematik bir artış göstermiştir. Bu spektral bölgeler, karbohidrat bantlarının C–O büükülme moduna karşılık gelmektedir ve PD örneklerinin plazma karbohidratlarındaki değişiklikleri ortaya koymaktadır. FTIR spektrumlarındaki bu karbonhidrat anormallikleri, evrelerden bağımsız olarak PD'nin tespiti için bir temel olarak kullanılmaktadır. Aşama 1 PD'de, 3060 cm^{-1} 'deki absorbans, kontrol ve diğer iki aşama PD örneğiyle karşılaştırıldığında azalmıştır. Bu bant, erken PD'de doymamış yağ asidi türevlerinde anormallik olduğunu gösteren doymamış yağ asidine karşılık gelmektedir. Bu durum, PD'nin erken tespiti için spektral belirteç görevi görmektedir. Evre 2 PD'de, spektrumlar kontrol ve diğer hastalık gruplarıyla karşılaştırıldığında 689 cm^{-1} 'de artan bir şiddet göstermektedir. Amino asitlerin C–C büükülmesi, C–C gerilmesi ve C–S gerilme moduna karşılık gelen bu bölge, evre 2 PD örneklerinde varyasyonlarını göstermektedir. Dahası, evre 3 PD örneklerinin 1542 , 2930 , 2953 , 3293 ve 3296 cm^{-1} 'de benzersiz spektral

varyasyonlar gözlemlenmiştir. 1542 cm^{-1} deki bant, evre 3 örneklerinde kontrol ve diğer PD evreleriyle karşılaştırıldığında şiddette önemli bir artış göstermektedir. Bu bölge, lipitlerin C=C titreşiminin gerilmesine karşılık gelmektedir. 2930 ve 2953 cm^{-1} deki bantlar, doymuş lipitlerin C-H'sinin gerilme titreşimlerine katkıda bulunarak önemli ölçüde artmıştır. Ayrıca, evre 3 PD örneklerinde 3293 ve 3296 cm^{-1} de absorbans artışı gözlemlenmiştir. Bu bölgeler proteinlerin amid I bandına karşılık gelmektedir. Bu bölgelerdeki varyasyonlar evre 3 PD örneklerinde proteinlerin anormallliğini düşündürmektedir. Bu nedenle, kümülatif analiz bu bölgelerin hastalığın evre 3 tanısı için nispeten önemli olduğunu göstermektedir (Ahmed vd., 2010).

Wang ve ark. (2020) PD hastalarının ve sağlıklı kişilerin serumlarını FTIR spektroskopisi kullanarak karşılaştırmıştır. Pik alanı oranlarındaki ve protein sekonder yapısındaki değişiklikler analiz edilmiştir. Lipitle ilgili bantları (yaklaşık 2958, 2930, 2872, 1738, 1451 ve 1399 cm^{-1}), proteinle ilgili bantları (yaklaşık 3294, 3067, 1652, 1545, 1399, 1313 ve 1169 cm^{-1}) ve nükleik asitle ilgili bantları (yaklaşık 1243 ve 1080 cm^{-1}) içeren ana bantların atamaları yapılmıştır. PD grubu ile kontrol grubu arasında pik pozisyonunda belirgin bir fark gözlemlenmemiştir çünkü kaymadaki tüm farklar 8 cm^{-1} den (spektral çözünürlük) düşüktür. A3294, A3067, A1652, A1545, A1451, A1399, A1313 ve A1243 gibi pik alanları ölçülmüştür. Daha sonra A3294/A3067, A1652/A1545, A1399/A1451, A1243/A1313 gibi pik alan oranları hesaplamıştır ve PD grubu ile kontrol grubu arasındaki farklar karşılaştırılmıştır. A3294/A3067 için 3294 ve 3067 cm^{-1} civarındaki bantlar sırasıyla amid A ve amid B'nin N-H gerilme titreşiminden katkı sağlamaktadır. Bunların değişimi, proteinlerdeki hidrojen bağının biçimini ve derecesinin değişimini yansımaktadır. PD grubunun A3294/A3067'si kontrol grubunkinden önemli ölçüde düşüktür. A1652/A1545 için 1652 ve 1545 cm^{-1} civarındaki bantlar sırasıyla amid I ve amid II olarak bilinmektedir. A1652/A1545, proteinlerin konformasyonel değişimlerini tanımlamak için kullanılmaktadır. PD grubu ile kontrol grubu arasında A1652/A1545'de önemli bir fark bulunmamaktadır. A1399/A1451 için 1451 cm^{-1} civarındaki bant lipitlerin metilen deformasyonundan kaynaklanırken, 1399 cm^{-1} civarındaki bant lipitlerin (ve bazı proteinlerin) metil büükülmesinden kaynaklanmaktadır. A1399/A1451 serumdaki lipitlerdeki değişiklikleri yansımaktadır. PD grubunun A1399/A1451'i kontrol grubundan önemli ölçüde düşüktür.

A1243/A1313 için 1313 cm^{-1} civarındaki bant, amid III'ün α -heliksinden katkı sağlarken, 1243 cm^{-1} civarındaki bant, amid III'ün β -tabakasından ve nükleik asitlerin asimetrik PO_2^- gerilmesinden katkı sağlamaktadır. A1243/A1313, amid III ve nükleik asitler bölgesindeki değişiklikleri yansımaktadır. PD grubunun A1243/A1313'ü, kontrol grubundan önemli ölçüde daha yüksektir. Sonuç olarak, tüm bu farklar esas olarak lipitlerin, proteinlerin ve nükleik asitlerin içeriğindeki ve yapısındaki değişikliklerden kaynaklamıştır. A3294/A3067 (amid A/amid B), PD oluşumunun proteinlerdeki hidrojen bağlarının değişmesine yol açtığını göstermiştir. A1399/A1451 (metil bükülmesi/metilen deformasyonu), ana zincirin uzunluğu ve dallanmış zincirlerin sayısı gibi lipit yapısındaki değişiklikleri yansımıştır. A1243/A1313 (amid III/ PO_2^- asimetrik gerilme), proteinlerin ve nükleik asitlerin göreceli içeriğindeki değişiklikleri göstermiştir. Amid I, esas olarak peptit omurgasının C=O gerilmesinden katkı sağlamaktadır ve sıkılıkla proteinlerin ikincil yapılarındaki değişiklikleri belirlemek için kullanılmaktadır. PD'nin neden olduğu serum proteinlerindeki değişikliği daha fazla analiz etmek için, Gauss formülü kullanılarak $1725\text{--}1593\text{ cm}^{-1}$ bölgesinde eğri uydurma gerçekleştirılmıştır. İkinci türev IR spektrumları, eğri uydurma eğrilerini elde etmek için kullanılmış ve bunlardan $1725\text{--}1593\text{ cm}^{-1}$ bölgesinde yaklaşık 1686 cm^{-1} ve 1656 cm^{-1} 'de iki pik gözlenmiştir. 1686 ve 1656 cm^{-1} civarındaki pikler, proteinlerin sırasıyla β -tabaka yapısı ve α -heliks yapısından kaynaklanmaktadır. Eğri uydurmadan, A1656/A1686'yı hesaplamak için A1686 ve A1656 olarak pik alanları elde edilmiştir. PD grubunun A1656/A1686'sı kontrol grubunkinden önemli ölçüde düşüktür, bu da α -heliks ve β -tabakasının göreceli içeriğinin sağlıklı kişilerde PD hastalarına göre daha yüksek olduğunu göstermektedir (Wang vd., 2020).

3.3. Amyotrofik Lateral Skleroz (ALS)

Tkachenko ve ark. (2024), infrared spektroskopisini kemometrik analizle birleştirerek amyotrofik lateral skleroz (ALS) hastalarından alınan kan örneklerinden hastalık profillerini etkili bir şekilde tanımlayıp tahmin edebileceğini araştırmıştır. Farklı hasta grupları arasında ayrim yapılmasına olanak sağlayan spektral bölgenin, aminoasitler, lipitler, fosfolipitler ve karbohidratlar gibi farklı biyokimyasal bileşikleri karakterize eden çok sayıda banttan oluşan parmak izi bölgesinde yer aldığı belirtilmiştir. $1450\text{--}1400\text{ cm}^{-1}$ 'deki bölgenin asimetrik ve simetrik metil bükülme modları ile karakterize edilmiştir. $1500\text{--}1350\text{ cm}^{-1}$ bölgesinde

lipit asil zincirlerinden gelen $-\text{CH}_2$ ve $-\text{CH}_3$ titreşimlerine ve 1270–1000 cm^{-1} bölgesi fosfolipitteki $-\text{PO}_2^-$ 'nin asimetrik ve simetrik titreşimlerine karşılık gelmektedir. C–O/C–C gruplarının gerilme titreşimleri 1200 ile 800 cm^{-1} arasında bulunan bantlara ait iken karbohidrat spektrumlarının CH_3/CH_2 deformasyon modları 1500–1200 cm^{-1} bantlarına karşılık gelmiştir. Nükleik asitlerin spektrumları farklı spektral bölgeleri, 1550 ile 1270 cm^{-1} arası şeker titreşimleriyle birleşen bazların deformasyon titreşimlerini ve 1270–1000 cm^{-1} bölgesi $-\text{PO}_2^-$ titreşimleri veya şeker-fosfat omurgası titreşimlerini içermektedir (Tkachenko vd., 2024).

Khoury ve ark. (2019), ALS hastalarının serumlarının infrared spektroskopik imzalarını elde etmek için 2,5 μL serum örneği kullanmış ve bunları sağlıklı kontrollerle karşılaştırmıştır. 3700–2700 ve 1800–700 cm^{-1} bölgelerindeki tüm sağlıklı kontrol ve ALS hastalarının serum örneklerinin spektrumları, lipitlerin, proteinlerin, karbohidratların ve nükleik bazların emiliminden gerçekleştiği ortaya konulmuştur. Her bir popülasyonun ortalama spektrumları, farklı popülasyonlar arasındaki küçük farklılıkların daha iyi gözlenmesine olanak tanımıştır. En yoğun bantlar esas olarak proteinlerin amid modlarından kaynaklanmıştır. Bu bantlarda, bir popülasyondan diğerine önemli bir fark göstermemiştir ve bu durum serum örneklerindeki diğer proteinlerle karşılaşıldığında insan serum albümin proteininin bolluğuundan kaynaklanmıştır. Bu farklılıklar, ortalama spektrumların ikinci türevlerinde daha iyi görülmüştür. 3700–2700 cm^{-1} aralığı hastalıklardan en az etkilenen aralıktır ve anlamlı bir fark gözlenmemiştir. 1700–1200 cm^{-1} spektral aralığı protein ve lipitlerden gelen emilimler tarafından domine edilmiş ve üç serum grubu arasında hafif farklılıklar göstermiştir. En belirgin farklar karbohidratlar, DNA ve RNA'dan gelen emilimler tarafından domine edilen 1200–1000 cm^{-1} spektral aralığında gözlenmiştir. Buna göre, ALS hastalığı serumdaki DNA ve RNA'nın bileşimini veya yapısını değiştirmiştir. Aynı zamanda, karbohidratların etkilenen imzası glikolipitlerde, glikoproteinlerde ve kolajende değişiklikleri yansımıştır (El Khoury vd., 2019).

3.4. Multipl Skleroz (MS)

Kołodziej ve ark. (2022), Multipl Skleroz (MS) hastalarından ve sağlıklı bireylerden toplanan kan plazması ve serum örneklerini zayıflatılmış toplam yansımı Fourier dönüşüm infrared (ATR-FTIR) spektroskopisi ile incelemiştir. Plazma ve serumun ortalama spektrumları

parmak izi bölgesinde ($1700\text{-}900\text{ cm}^{-1}$) alınmıştır. 1690 , 1140 , 1078 ve 945 cm^{-1} deki piklerin esas olarak β -tabakalı protein yapısına, nükleik asitlere, C-O kısımları içeren biyomoleküllere karşılık gelirken, 1652 , 1541 , 1169 , 1124 ve 923 cm^{-1} deki pikler sırasıyla α -helisel proteinlere, fosfolipitlere ve RNA'ya karşılık gelmiştir. Plazmayı serumdan ayıran en belirgin ayırcı faktör, α -heliks yapıya sahip proteinlerle ilişkili olan 1652 cm^{-1} deki piktir. Bu, serumda yaklaşık % 68 α -heliks ve β -tabaka zincirleri içermeyen en bol protein olan albüminkle ilişkili olduğu ortaya konulmuştur. Ayrıca, plazma örnekleri için en iyi farklılaşma $1360\text{-}900\text{ cm}^{-1}$ bölgesinde gözlenmiştir. Sağlıklı kontrol en belirgin bant (1270 cm^{-1}) MS için 1276 cm^{-1} e kaymıştır ve bunun, MS sırasında parçalanmaya uğrayan kan plazmasında bulunan kolajen benzeri proteinlerdeki değişikliklerle ilişkili olduğu saptanmıştır. Plazmanın aksine, serum örnekleri için parmak izi bölgesindeki sağlıklı kontrol ve MS arasında daha iyi farklılaşma göstermiştir. Bu durum ikincil protein yapılarının güçlü bir etkisi olduğunu göstermektedir. Sağlıklı kontrolden türetilen serum durumunda, α -heliks proteinin baskınlığı mevcuttur (1652 cm^{-1}), ancak, MS sırasında β -tabaka yapısı proteinleri esas olarak gözlenmektedir (1625 cm^{-1}). Bu, multipl sklerozda da gözlenen nörodejenerasyon göstergesi olduğuna inanılan amiloid- β 'nin varlığıyla ilişkili olmaktadır. Bu farklılıklar, serumda bulunmayan büyük pihtlaşma proteinleri nedeniyle plazmaya yansıtılmamış olabilir. Ayrıca, amid III bantlarında değişiklikler fark edilebilir (1265 cm^{-1} sağlıklı kontrole karşı 1284 cm^{-1} MS). Sonuç olarak, protein yapısı hakkında bilginin elde edilebildiği parmak izi bölgesinde serum örnekleri için daha iyi bir ayrımla gözlemlenmiştir. Serum örneklerinde gözlemlenen değişikliklerin yanı sıra, her iki biyosivirda da amid III için bant pozisyonunda önemli değişiklikler gözlemlenmiştir. Serumda 1265 cm^{-1} bandı $\sim 19\text{ cm}^{-1}$ maviye kaymıştır. Bu eğilim plazma spektrumlarda da gözlemlenmiştir; bant kayması yaklaşık 6 cm^{-1} dir ve aynı anda 916 cm^{-1} deki bant kaybolmuştur. Bu tür değişiklikler, tirozin kalıntılarını içeren proteinlerin önemli ölçüde azalmasıyla tetiklenebilecek amid III konformasyonel değişikliklerini temsil etmektedir (Kołodziej vd., 2022).

Condino ve ark. (2023), sağlıklı kontrol (HC) deneklerinin ve MS hastalarının kan plazması örneklerinin ATR-FTIR spektrumlardan türetilen bir dizi spektral biyobelirteci bir araya getirerek, iki grup birey arasında ayrımla yapmaya çalışmıştır. MS hastalarının ve sağlıklı kontrollerin en önemli iki bölgedeki ATR-FTIR spektrumları, CH_2 ve

CH_3 'ün simetrik ve asimetrik gerilme titreşimlerini içeren 3050–2800 cm^{-1} ve en belirgin piklerin proteinlerin emilim bandından kaynaklanan amid I ve amid II pikleri olduğu 1800–900 cm^{-1} aralığındaki parmak izi bölgesinde incelenmiştir. İki birey grubu arasındaki farkları ortaya çıkarmak için, plazmada bulunan moleküler bileşenlerle ve moleküler fonksiyonel gruplarla ilgili spesifik piklerle ilişkili bir dizi spektral göstergesi belirlenmiştir: (1) 3050 ile 2800 cm^{-1} arasındaki bölgeye karşılık gelen alan, A_{HR} ; amid I ve amid II piklerine karşılık gelen alan, $A_{\text{HR}}/A_{\text{amidI+amidII}}$; A_{HR} üzerindeki olefinik $\text{C}=\text{CH}$ pikinin alanı, $A_{\text{olefinik}}/A_{\text{HR}}$; CH_2 'nin asimetrik gerilme titreşim pik alanı, $A_{\text{CH2as}}/A_{\text{HR}}$ ve $A_{\text{amidI}}/A_{\text{amidII}}$ olarak belirlenen lipid/proteinler gibi moleküler bileşenlerin alan oranları (2) fonksiyonel grupların spesifik piklerinin şiddet oranı, I_{1453}/I_{1650} , I_{1739}/I_{1468} (3) amid I ve 1739 cm^{-1} 'deki ester $\text{C}=\text{O}$ pikinin bant genişliği ve (4) MS'nin HC'den ayırt edilmesi için önemli dalga sayıları olarak 1320, 1510, 2860 ve 3016 cm^{-1} 'deki şiddetler seçilmiştir (Condino vd., 2023).

Crocco ve ark. (2023), MS hastalarını sağlıklı kontrol bireylerden ayırmak ve hızlı bir noninvaziv kan testiyle tanıya yardımcı olan potansiyel spektral biyobelirteçleri belirlemek için plazma örneklerini analiz etmek amacıyla zayıflatılmış toplam yansımış Fourier dönüşüm infrared (ATR-FTIR) spektroskopisi kullanmıştır. Çalışma grubu, 45 MS hastası ve 40 sağlıklı kontrol (HC) olmak üzere 85 kişiden oluşturulmuş ve infrared spektrumları hem parmak izi bölgesinde (1800–900 cm^{-1}) hem de 3050–2800 cm^{-1} bölgesinde alınmıştır. Yüksek şiddetteki iki pik amid I'ye (1650 cm^{-1} , $\text{C}=\text{O}$ gerilme titreşimi) ve amid II bandına (1547 cm^{-1} , N–H büükülmesi ve C–N gerilmesi) karşılık gelmektedir. Kan plazmasının proteomik profili oldukça karmaşık olduğundan plazmada daha fazla bolluğa sahip proteinler insan serum albümünü (HSA ~ %60 ağırlıkça), immünonoglobulin (IgG ~ %14), transferin (%6) ve fibrinojendir (%4). HSA yaygın bir α -heliks sekonder yapıya sahiptir ve 1650 cm^{-1} 'deki pikten sorumludur, IgG yaklaşık 1633 cm^{-1} 'de emilen bir β -tabaka proteinidir. Parmak izi bölgesinde, lipitler 1740 ve 1453 cm^{-1} 'de merkezlenen bantlara ana katkıda bulunmuştur. ATR-FTIR spektrumunun 3050–2800 cm^{-1} bölgesi esas olarak lipitler ve proteinlerdeki CH_3 ve CH_2 gruplarının asimetrik (sırasıyla 2960 ve 2927 cm^{-1}) ve simetrik (sırasıyla 2872 ve 2852 cm^{-1}) gerilme titreşimlerine karşılık gelmektedir. Bu bölgeye ayrıca N–H (NH_3^+) gerilme titreşimleri de katkı sağlamıştır. Hem parmak izi hem de 3050–2800 cm^{-1} bölgelerinde, HC ve MS ortalama spektrumlarının spektral özelliklerinin

çok benzer olduğu ve yalnızca görsel incelemeden sağlık durumıyla ilişkili olabilecek belirli farklılıklarını tespit etmenin zor olduğu belirtilmiştir. Lipitlerin ester C=O gerilme bandına atanan 1750–1725 cm^{-1} bölgesi MS grubunda daha şiddetlidir ve ayrıca amid I pikinin şiddeti azalmıştır. Bu sonuç lipit ve protein konsantrasyonunda/metabolizmasında bir değişikliğe işaret etmektedir. 1468 cm^{-1} 'deki CH_2 emilim pikinin şiddetine göre C=O bandının şiddetindeki artış (I_{1739}/I_{1468}), multipl sklerozun patogenezinde rol oynadığı varsayılan serbest radikaller tarafından üretilen oksitlenmiş lipitlerin varlığıyla ilişkilendirilmiştir. ATR-FTIR spektrumlarında 3050–2800 cm^{-1} bölgesinde pik şiddetine hafif değişiklikler meydana gelmiştir. Özellikle, olefinik C=CH gerilme titresimine atanan ~3013 cm^{-1} 'deki bant, doymamış lipidin tipik bir örneği olmaktadır ve MS hastalarında artmaktadır. Ayrıca, MS hastalarında CH_2 asimetrik gerilmenin şiddeti ~2927 cm^{-1} 'de sağlıklı kontrol bireylere kıyasla artmıştır. Önemli spektral bantların olası hastalık kaynaklı farklılıklarını daha ayrıntılı olarak incelemek için, belirli fonksiyonel grupların şiddet oranını ve moleküler bileşenlerin alan oranını da belirlenmiştir. Özellikle, lipit/protein oranı iki farklı şekilde: 1453 cm^{-1} ve amid I'deki (1650 cm^{-1}) piklerin şiddet oranını alınarak veya 3050–2800 cm^{-1} bölgesinin altındaki alanların oranını olarak (AHR) ve amid I ve amid II bantlarının altındaki alanların toplamı olarak saptanmıştır. Her iki belirleme de MS hastalarında lipit/protein oranında kontrol grubuna kıyasla bir artış olduğunu göstermiştir (Crocco vd., 2023).

KAYNAKÇA

Ahmed, S.S.S.J., Santosh, W., Kumar, S., Christlet, T.H.T. (2010), Neural network algorithm for the early detection of Parkinson's disease from blood plasma by FTIR micro-spectroscopy, *Vibrational Spectroscopy*, 53, 181–188.

Cannon, J.R., Greenamyre, J.T. (2011), The Role of environmental exposures in neurodegeneration and neurodegenerative diseases, *Toxicological Sciences*, 124(2), 225–250.

Carmona, P., Molina, M., Calero, M., Bermejo-Pareja, F., Martínez-Martín, P., Toledano, A. (2013), Discrimination analysis of blood plasma associated with Alzheimer's disease using vibrational spectroscopy, *Journal of Alzheimer's Disease*, 34, 911–920.

Chen, X., Guo, C., Kong, J. (2012), Oxidative stress in neurodegenerative diseases, *Neural Regeneration Research*, 7(5), 376–385.

Condino, F., Crocco, M.C., Pirritano, D., Petrone, A., Del Giudice, F., Guzzi, R. (2023), A linear predictor based on FTIR spectral biomarkers improves disease diagnosis classification: An application to multiple sclerosis, *J. Pers. Med.*, 13, 1596.

Dawson, T.M., Golde, T.E., Lagier-Tourenne, C. (2018), Animal models of neurodegenerative diseases, *Nature Neuroscience*, 21, 1370–1379.

Durães, F., Pinto, M., Sousa, E. (2018), Old drugs as new treatments for neurodegenerative diseases, *Pharmaceuticals*, 11(44), 1–21.

El Khoury, Y., Collongues, N., De Sèze, J., Gulsari, V., Patte-Mensah, C., Marcou, G., Varnek, A., Mensah-Nyagan, A.G., Hellwig, P. (2019), Serum-based differentiation between multiple sclerosis and amyotrophic lateral sclerosis by Random Forest classification of FTIR spectra, *Analyst*, 144, 4647–4652.

Gitler, A.D., Dhillon, P., Shorter, J. (2017), Neurodegenerative disease: models, mechanisms, and a new hope, *Disease Models & Mechanisms*, 10, 499–502.

Habartová, L., Hrubešová, K., Syslová, K., Vondroušová, J., Fišar, Z., Jirák, R., Raboch, J., Setnička, V. (2019), Blood-based molecular signature of Alzheimer's disease via spectroscopy and metabolomics, *Clinical Biochemistry*, 72, 58–63.

Kołodziej, M., Chrząszcz, K., Pięta, E., Piergies, N., Rudnicka-Czerwiec, J., Bartosik-Psujeć, H., Paluszkiewicz, C., Cholewa, M., Kwiatek, W.M. (2022), Spectral signature of multiple sclerosis. Preliminary studies of blood fraction by ATR FTIR technique, *Biochemical and Biophysical Research Communications*, 593, 40–45.

Lopes, J., Correia, M., Martins, I., Henriques, A.G., Delgadillo, I., da Cruz e Silva, O., Nunes, A. (2016), FTIR and Raman spectroscopy applied to dementia diagnosis through analysis of biological fluids, *Journal of Alzheimer's Disease*, 52, 801–812.

Martins, T.S., Magalhães, S., Rosa, I.M., Vogelsgang, J., Wiltfang, J., Delgadillo, I., Catita, J., da Cruz e Silva, O.A.B., Nunes, A., Henriques, A.G. (2020), Potential of FTIR spectroscopy applied to exosomes for Alzheimer's disease discrimination: A pilot study, *Journal of Alzheimer's Disease*, 74, 391–405.

Martins, T.S., Ferreira, M., Magalhães, S., Leandro, K., Almeida, L.P., Vogelsgang, J., Breitling, B., Hansen, N., Esselmann, H., Wiltfang, J., da Cruz e Silva, O.A.B., Nunes, A., Henriques, A.G. (2024), FTIR spectroscopy and blood-derived extracellular vesicles duo in Alzheimer's disease, *Journal of Alzheimer's Disease*, 98, 1157–1167.

Paraskevaidi, M., Morais, C.L.M., Lima, K.M.G., Snowden, J.S., Saxon, J.A., Richardson, A.M.T., Jones, M., Mann, D.M.A., Allsop, D., Martin-Hirsch, P.L., Martin, F.L. (2017), Differential diagnosis of Alzheimer's disease using spectrochemical analysis of blood, *PNAS*, 114(38), E7929–E7938.

Richardson, A.M.T., Jones, M., Mann, D.M.A., Allsop, D., Martin-Hirsch, P.L., Martin, F.L. (2017), Differential diagnosis of Alzheimer's disease using spectrochemical analysis of blood, *PNAS*, 114(38), E7929–E7938.

Singh, A., Kukreti, R., Saso, L., Kukreti, S. (2019), Oxidative stress: A key modulator in neurodegenerative diseases, *Molecules*, 24, 1583.

Theakstone, A.G., Rinaldi, C., Butler, H.J., Cameron, J.M., Confield, L.R., Rutherford, S.H., Sala, A., Sangamnerkar, S., Baker, M.J. (2021), Fourier-transform infrared spectroscopy of biofluids: A practical approach, *Translational Biophotonics*, 3(2), e202000025.

Tkachenko, K., Espinosa, M., Esteban-Díez, I., González-Sáiz, J.M., Pizarro, C. (2022), Extraction of reduced infrared biomarker signatures for the stratification of patients affected by Parkinson's disease: An untargeted metabolomic approach, *Chemosensors*, 10, 229.

Tkachenko, K., González-Sáiz, J.M., Calvo, A.J., Lunetta, C., Osta, R., Pizarro, C. (2024), Comparative Blood Profiling Based on ATR-FTIR spectroscopy and chemometrics for differential diagnosis of patients with amyotrophic lateral sclerosis—Pilot study, *Biosensors*, 14, 526.

Wang, X., Wu, Q., Li, C., Zhou, Y., Xu, F., Zong, L., Ge, S. (2020), A study of Parkinson's disease patients' serum using FTIR spectroscopy, *Infrared Physics and Technology*, 106, 103279.

RANDOM LAZERLER¹

Ekrem YARTAŞI²

1. GİRİŞ

Çevremizdeki ışık, etkileşimde bulunduğu yüzeyler tarafından saçılma, yansıtma veya soğurma özellikleri sayesinde nesneleri görünür kılar ve dünyayı algılamanın temel yollarından biridir. ışık, serbest uzayda doğrusal bir yol izler, ancak ışık ışınlarının herhangi bir tür saçılma veya soğurma olmaksızın, örneğin doğrudan gözüümüze ulaşması oldukça nadirdir. Bu bağlamda, dalgaların (kuantum parçacıkları ya da klasik dalgalar) rastgele dağılmış bir ortamda yayılması, 20. yüzyıldan itibaren araştırmacıların büyük ilgisini çekmiştir.

İşığın rastgele yayılmasını içeren düzensiz hareketin ilk bilimsel tanımının Robert Brown'a ait olduğu kabul edilir. Brown, su üzerindeki polen hareketi ile ilgili çalışmasıyla bu olguyu ortaya koymuştur. Robert Brown'in anısına Brown hareketi olarak adlandırılan rastgele yürüyüşün matematiksel ve fiziksel açıklaması, ilk kez Einstein tarafından 1905 yılında ünlü difüzyon denklemi ile verilmiştir. Çoklu saçılma, günlük yaşamda neredeyse opak malzemeler için yaygın bir olgudur ve ışığın nesnelerin içine nüfuz etmesi ve ortamdan çıkmadan önce çok sayıda saçılma yaşamıyla nesnelerin görünümünü belirler. Bu durum, bulutlar, insan derisi veya herhangi bir tür toz gibi malzemelerde gözlemlenebilir. Çoklu saçılma, ortalama serbest yol (l_s) ve difüzyon katsayısı (D) olmak üzere iki ana parametreyle tanımlanır. Bunlardan ilki İki ardışık saçılma olayı arasındaki mesafe veya rastgele yürüyüsteki ortalama adım boyudur, ikincisi ise, bir maddenin belirli bir ortamda ne kadar hızlı hareket ettiğini veya bir kesit alanından ne kadar hızlı geçtiğini ölçer ve birimi m^2/s (alan/zaman) şeklindedir. Lazer ışın demeti pürüzlü bir yüzeye düşürüldüğünde lazer lekeleri (speckles) olarak bilinen desenler oluşur. Bu parlak noktalar, koherent ışığın yüzeyde yapıcı ve yıkıcı girişimlerin meydana gelmesi ile oluşur. Eğer fotonlar sık ve güclü saçılma olaylarına maruz kalırsa, ortamda serbestçe hareket etme yeteneklerini kaybeder.

¹ Yartaş, E., Fibre optic wedge type cavity random laser, PhD Thesis, 2019.

² Dr. Öğr. Üyesi, Sivas Bilim ve Teknoloji Üniversitesi, Mühendislik ve Doğa Bilimleri Fakültesi, Mühendislik Temel Bilimleri Bölümü, ekrem.yartasi@sivas.edu.tr, ORCID: 0000-0003-0071-951X

Konvansiyonel bir lazerden farklı olarak, bir rastgele lazer (RL), temel olarak aynasız bir uyarılmış (stimulated) ışık kaynağıdır. Işığın uyarma mekanizması, kazanç ortamında güçlü bir saçılma mekanizması bulunmasına dayanır, bu sayede kavitasyon verimliliği, kazanç ortamı ve saçılma dinamiklerine bağlı olarak RL'ler, neredeyse tutarlı lazer ışığı üretebilir. Işığın difüzyonunun lazer yayılmasını elde etmek için kazanç sağlamak amacıyla kullanılması fikri ilk kez Letokhov tarafından teorik olarak öngörlülmüştür (Letokhov, 1967). Letokhov, difüzyon yoluyla ışığın güçlendirilmesinin hacimle orantılı, kayıpların ise saçılma ortamının yüzeyiyle orantılı belirtmiştir. Başka bir ifadeyle kavite hacmi lazer ışığı elde etmek için net foton kazancı sağlayacak kadar büyüğe buradan sürdürülebilir bir lazer spektrumu elde edilebilir. Letokhov'un çalışmasından farklı olarak, güçlü saçılma rejiminde lazer amplifikasyonunun dinamikleri özel malzeme konfigürasyonları ile araştırılmıştır (Gouedard vd., 1993; Lawandy vd., 1994). Bazı malzemelerde yoğun saçılma, bilindik, tasarlanmış bir rezonatöre sahip lazerlerde olduğu gibi yapıcı girişim yoluyla lazer oluşumuna sebep olabilir (Lagendijk vd., 1987). Eğer ışık ortamda serbestçe yayılma yeteneğini kaybeder ve çoklu saçılma yaşarsa, l_s , dalga vektörünün (k) tersine eşit ya da daha küçük hale gelir. Bu durum matematiksel olarak aşağıdaki gibi verilir:

$$kl_s \leq 1 \quad (2.1.1)$$

Bu şekilde, ışık, sınırlı bir hacimde güçlü saçılma nedeniyle kendi kendine oluşan bir döngüye girer ve rezonatörlü geleneksel lazerler gibi belli bir kritik kazanç değerine ulaştığında lazer atımı elde edilir. Bu şekilde çalışabilen ilk RL'de hem emisyon kaynağı hem de saçılma merkezi olarak ZnO parçacıkları kullanılmış ve güçlü saçılma yoluyla rezonant kavite oluşumu sağlanmıştır (Cao vd., 1999).

2. RANDOM LASER

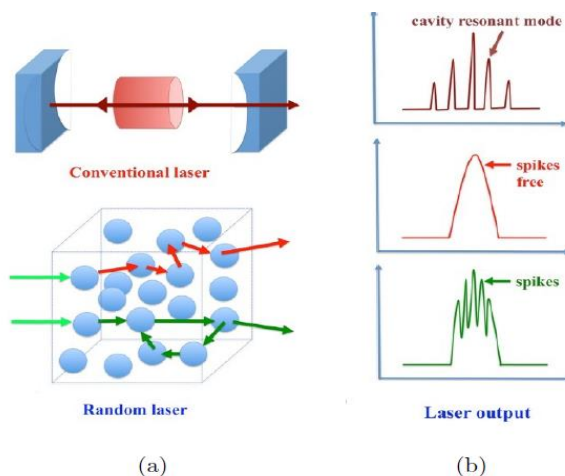
Elektromanyetik dalgaların saçılması iki farklı model ile incelenebilir. Birincisi, dağılma merkezinin boyutunun ışığın dalga boyutundan çok daha küçük olduğu durumlar için geçerli olan Rayleigh modelidir. İkincisi ise, dağılma merkezinin boyutunun ışığın dalga boyutuna yakın olduğu durumları ele alan, Gustav Mie tarafından geliştirilen Mie modelidir. Düzensiz bir ortamın saçılma düzeyini belirleyen iki ana faktör $l_s = (\rho\sigma_s)^{-1}$ ve l_t olarak verilir. l_t ışığın düzensiz

ortam içinde rastgele saçılmağa başladığı minimum mesafeyi temsil eder. Burada ρ ve σ_s sırasıyla, yoğunluk ve saçılma kesit alanını ifade etmektedir. l_s ve l_t arasındaki ilişki aşağıdaki gibi verilir

$$l_t = \frac{l_s}{1 - <\cos\theta>} \quad (2.1.1)$$

Burada θ saçılma açısıdır ve dikkat edilirse dik açı değerinde $l_s=l_t$ olur. Diğer bir faktör de RL ortamının kazanç mesafesidir ve ışığın lazer ortamında e sayısı kadar güçlendiği mesafeyi ifade eder. ışığın düzensiz bir ortamda yayılımı, lokalize ($kl_s \leq 1$), difüzif dağılım ($\lambda \leq l_s \leq L$) ve zayıf dağılım ($l_s \leq L$) olmak üzere üç farklı ölçekte tanımlanabilir. Burada λ ve L , sırasıyla, dalgaboyu ve kazanç ortamının boyutudur.

Optik aktif bir ortamda, örneğin random nano yapılar içeren bir dye çözeltisinde, ışık kazanç ortamından çıkmadan önce şiddetli şekilde saçılmalara uğrar. Ortamındaki radyasyon optik pozitif geri beslemeye yol açacak kadar içerisinde hapsolur ve RL'in temelini oluşturan bu durum lazer ışığının elde edilmesiyle sonuçlanır. İlk kez Wiersma tarafından ortaya atılan bu kavram (Wiersma, 2008; Wiersma vd., 1995), geleneksel lazerlerin aksine, düzensiz bir ortamda yoğun saçılma yoluyla optik geri besleme sağlamak amacıyla kullanılan bir cihaz olarak tanımlanır. RL'ler non-rezonant ve rezonant olmak üzere iki ana başlık altında sınıflandırılır. Rasgele lazerlerin geleneksel lazerlerden ayırcı özelliği, lazerin işletim dalgaboyunun, fotonların çoklu saçılma maruz kaldığı düzensiz ortam tarafından belirlenmesidir; bu, belirli bir rezonatör boşluğunun olmadığı anlamına gelir. Ortam içindeki ışık için optik geri besleme sağlayan bir yol olması ve bu yolu, pompa gücünün lazer eşğini aştığı anda durağan durumdaki fotonların etkileşimde olduğu ortam tarafından belirlenmesi, rasgele lazerin dalga boyunun belirlenmesinde rol oynar.



Sekil 2-1 a) geleneksel ve RL şematiği b) spektrumları

Non-Rezonant RL'de, pik dalgaboyları, belirgin şekilde daralmış emisyon spektrumunun merkezi frekansıyla belirlenir. Kendiliğinden yayılan fotonlar, kazanç ortamından çıkmadan önce şiddetli saçılmasına maruz kalır ve radyasyon hapsolur. Bu arada, uyarılmış emisyonla ek fotonlar üretilir ve optik kazanç, daha fazla uyarılma süreciyle büyümeye başlar. Bu rejimde saçılma bir optik rezonatördeki kadar güçlü değildir ve lazer spektrumu nispeten genişdir. Bu durum, Şekil 2-1a'da kırmızı oklarla gösterilmiştir. Görülebileceği gibi lazer modları genellikle birbirleriyle örtüşür, çünkü kapalı bir döngü yoktur. Diğer yandan yeterince yoğun bir ortamda ışık şiddetli saçımalarla ortamda bir döngü oluşturabilir (yeşil oklar), bu durumda Şekil 2-1b'deki gibi bir lazer spektrumu oluşur.

2.1. Non-Rezonant Karakterli (İnkoherent) Random Lazerler

Konvansiyonel bir lazerin en önemli özelliği, içindeki osilatör modlarının dalga vektörlerinin lazerin kabul edilebilir katı açısı içinde olmasıdır. Bu modlar enerji ve faz bilgisini kaybetmeden "izin verilen modlar" olarak adlandırılır. Daha önce belirtildiği gibi, rezonanssız geri besleme sisteminde, yalnızca saçılmanın şiddetli fotonların hapsolmasına yol açarsa belirgin bir lazer modu elde edilebilir. Bu durum yüksek kayıplı ve difüzif bir kazanç ortamının sonucudur. Düzensiz ortamda oluşturulan ışık yüksek düzeyde saçılmasına uğrar ve yönü sürekli değişir ve rezonatördeki gibi belirgin bir turu tamamlayamaz. Bunun doğal bir sonucu olarak düşük Q-faktörü, zayıf bir frekans seçimi vardır ve lazer frekansları birbirleri ile örtüşür. Optik geri besleme frekansa bağlı değildir, çünkü saçılan fotonlar arasında faz ilişkililiği yoktur ve kazanç ortamında

spektral seçim bulunmaz; pozitif geri besleme yalnızca yoğunluk tarafından sağlanır, rezonanslı boşlukta faz ilişkililiği dominant değildir.

Letokhov, non-rezonant RL için ortalama saçılma mesafesinin l_s , sistemin ortalama boyutunun L 'den çok daha küçük ve lazer dalga boyunun çok daha büyük olduğunu varsayıarak $\lambda \ll l_s \ll L$ şeklinde bir model önermiştir. Fotonların düzensiz ortamda saçılmasını ışığın fazını ihmal ederek difüzyon denklemiyle modellenebileceğini göstermiştir. Aktif bir ortamda toplam kazanç, ortamın hacmiyle orantılıdır, ancak toplam kayıp yüzeyle orantılıdır. Saçılmanın gerçekleştiği aktif ortamın hacmi aşağıda verilen kritik değeri aşarsa optik kazanç, kayıpları aşip lazer modu elde edilebilir.

$$V_{critical} \approx L^3 \approx \left(\frac{l_t l_s}{3} \right)^{3/2} \quad (2.1.2)$$

Kararlı hal durumundaki tipik bir non-rezonant RL için kazanç ortamının foton akısı veya enerji yoğunluğu aşağıdaki gibi verilebilir.

$$\frac{\partial W(\vec{r}, t)}{\partial t} = \left[D \nabla^2 + \frac{\nu}{l_g} \right] W(\vec{r}, t) \quad (2.1.3)$$

Burada ν ışığın kazanç ortamındaki hızını, $D = \nu l_t / 3$ difüzyon katsayısını ve l_g optik kazancın mesafesini belirtmektedir. Genel çözüm denk. (2.1.4) ile verilir.

$$W(\vec{r}, t) = \sum_n a_n \psi_n(\vec{r}) \exp \left[-\left(DB_n^2 - (\nu/l_g) \right) t \right] \quad (2.1.4)$$

Ψ_n ve B_n sırasıyla denk. (2.1.5)'in öz fonksiyon ve öz değerleridir

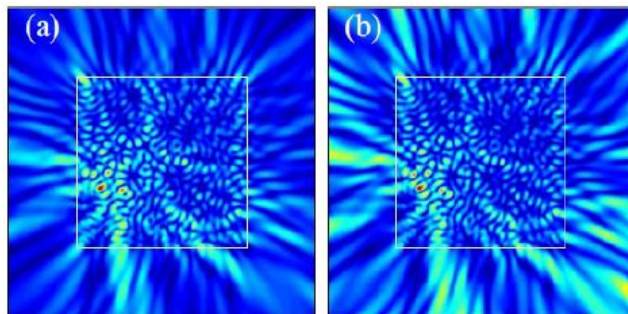
$$\nabla^2 \psi_n(\vec{r}) + B_n^2 \psi_n(\vec{r}) = 0 \quad (2.1.5)$$

ve denk. (2.1.4) içindeki üstel terime dikkat edilirse lazer eşik değeri aşağıdaki gibi olur.

$$DB_n^2 - (\nu/l_g) = 0 \quad (2.1.6)$$

Şekil 2-2'de non-rezonant RL için düşük Q-faktöre ve zayıf saçılma etkileşimine sahip bir kazanç ortamının simülasyonu yapıldığında lazer

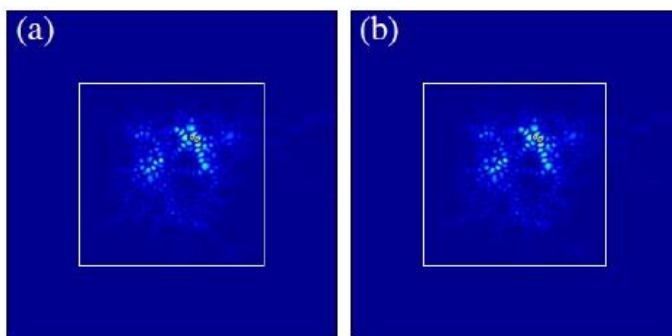
ortamındaki radyasyonun optik uyarılma duruktan hemen sonra hızla ortamı terk ettiği görülebilir.



Şekil 2-2 non-rezonant RL ortamında a) optik uyarılma sırasında b) sonrasında radyasyonun yayılmış profili (Andreasen vd., 2011)

2.2. Rezonant Karakterli Random Lazerler

Elektromanyetik dalgaların yapıçı girişimi (constructive interference) gerçekleşebilmesi için dalgaların fazlarının eşleşmesi (phase matching) gereklidir ve bu girişimin optik genlik geri beslemesi sağlayarak yapıçı bir şekilde gerçekleşmesi, genellikle konvansiyonel lazerlerde olduğu gibi uygun bir rezonatör gerektirir. RL'de ise, ışık saçılma ortamında rastgele bir şekilde oluşan kapalı bir döngüde hapsolup salınım yapabiliyorsa, koherent bir ışık elde etmek için konvansiyonel lazerin rastgele oluşan bir benzerinin işaret eder. Bu bağlamda, rezonant bir RL, aslında konvansiyonel lazerler gibi rezonans kavitesi kullanır. Tek fark, bu boşlukların materyal içinde rastgele oluşmasıdır, konvansiyonel lazerlerde ise rezonatörler, belirli bir dalga boyunda çalışacak şekilde özenle tasarlanmıştır.



Şekil 2-3 rezonant RL'de güçlü saçılma ortamında optik uyarılmanın durdurulmasının ardından ışık rezonansa girmektedir (Andreasen vd., 2011).

Bu konuda başı çeken çalışma, 1998 yılında Cao ve arkadaşları tarafından iki farklı malzeme kullanılarak gerçekleştirilmiştir: bunlar, ortalama parçacık büyülüğu yaklaşık 100 nm olan ZnO tozu ve polikristalin filmdir (Cao vd., 1998, 1999). Toz hem emisyon kaynağı hem de dağılma merkezi olarak görev yapmış ve ışık dağılma ortamında çeşitli kapalı döngüler oluşturmuş ve bu döngülerin yüksek olasılığı ile dalga, birkaç döngü aracılığıyla orijinal konumuna geri dönebilmiştir. Bu, pratikte, tozda güçlü saçılmanın, çeşitli döngülerde koherent geri beslemeye yol açtığı anlamına gelir. Bu şekilde rastgele oluşan mikro rezonatörler, yapıçı girişimi tetikleyerek, belirgin lazer frekanslarının, Şekil 2-3'deki gibi, ayrik lazer piklerinin görünmesini sağlar. Aynı çalışmada geri saçılma konisinin çizgi genişliğini analiz ederek l_t değeri ölçülmüştür. Kazanç ortamı içinde saçılma konisi şu şekildedir

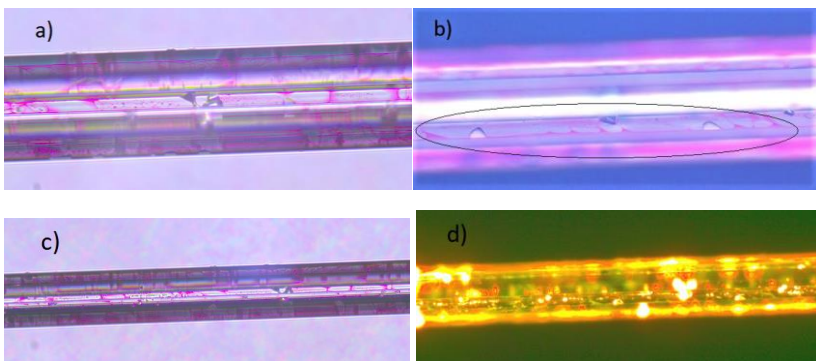
$$\Delta\theta \square \frac{0.7n_e(1-R)}{k_e l_t} \quad (2.1.7)$$

n_e , ZnO parçacıklarının etkin kırılma indeksini, R ise malzeme-hava kombinasyonunun difüzyon yansımaya katsayısını ve k_e , dağılma ortamındaki etkin dalga vektörünü temsil eder. $l_t \square \lambda_e$ durumu fotonların kazanç ortamında içinde güçlü şekilde lokalize olduğunu gösterir. Bu tür lazer modları, kapalı döngülerinde ve rezonans boşluklarında bu modların sürekli bir şekilde tekrarlanmasından dolayı çok dar spektrum genişliğine sahiptir. Koherent geri beslemeye dayalı rastgele lazerleme, genellikle nano ölçekli yapılarının güçlü dağılma merkezleri olarak görev yaptığı ortamlarda meydana gelir. Bu tarz bir konfigürasyonda, fotonların l_t değeri, dalga vektöründen daha kısadır. Bu durum, Ioffe-Regel kriteri olarak bilinir ($k_s l \leq 1$) (Abrahams vd., 1979). Bu rejim ilk olarak P. Anderson tarafından önerilmiş ve elektron geçişlerini açıklamak için Anderson lokalizasyonu olarak adlandırılmıştır (Anderson, 1958).

2.3. β Faktörü

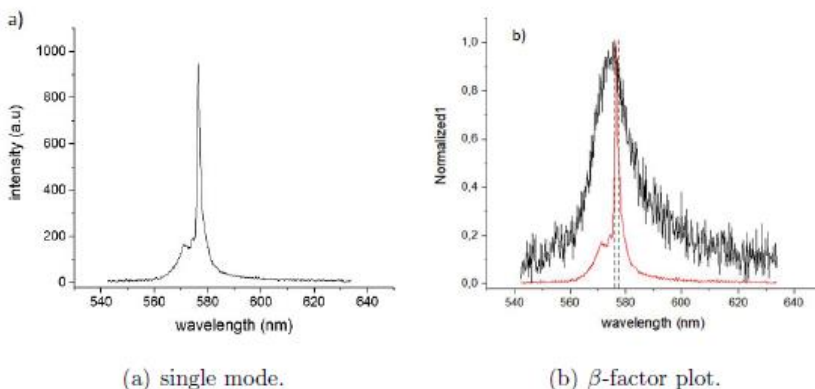
β -faktörünün tanımı, spontan emisyonun lazerleme modlarına oranı olarak yapılır. Başka bir deyişle, bu parametre, spontan emisyonun lazer emisyonuna ne kadar katkıda bulunduğu frekans açısından belirtir. Non-

rezonant bir RL için, β -faktörünün tek katkı kriteri, lazer eşiği öncesi spontan emisyon ile eşik sonrası emisyon arasındaki spektral örtüşmedir. Konvansiyonel lazerde geometrik kısıtlamalardan dolayı sadece kavite modlarının k -vektöryle örtüsen modlar lazer emisyonuna katkıda bulunabilir. Bu durum, neden konvansiyonel lazerlerde β -faktörünün oldukça düşük olduğunu açıklamaktadır. Diğer taraftan, konvansiyonel lazerlerin bazı spesifik türlerinin, örneğin koaksiyel kazanç ortamı (Khajavikhan vd., 2012) için β -faktörü parametresi büyük bir öneme sahiptir çünkü $\beta=1$ olarak ayarlandığında, yani tüm spontan emisyonun lazerleme moduna radyasyon yapması durumunda, eşiği olmayan bir lazerin çalışmasını mümkün kılabılır.



Şekil 2-4 Aynı bölgenin, (a) önden (b) arkadan aydınlatmayla alınan yanal optik görüntüleri. (c) ve (d)'de, aynı fiber bölgesinin 532 nm lazer ile uyarılması. (Yartaş & Inci, 2019)

Şekil 2-4'te dört çekirdekli bir fiberin üçgensel boşluklarında oluşturulan optik aktif kavitelerde çeşitli boyutlarda hava baloncukları oluşmuştur. Kazanç ortamı ile hava baloncukları arasında ciddi kırınım indisi farkı vardır ve bunlar saçılma noktaları işlevi görmektedirler. Şekil 2-4c ve 4d'de fiberin aynı bölgesinin uyarıcı lazer ışığı altında ortaya çıkan RL etkisi görülmektedir.



Sekil 2-5 single mod ile spontane mod spektrumlarının örtüşmesi, kesisen alanın spontane spektrum alanına oranı beta faktörünü verir. (Yartaşı & Inci, 2019)

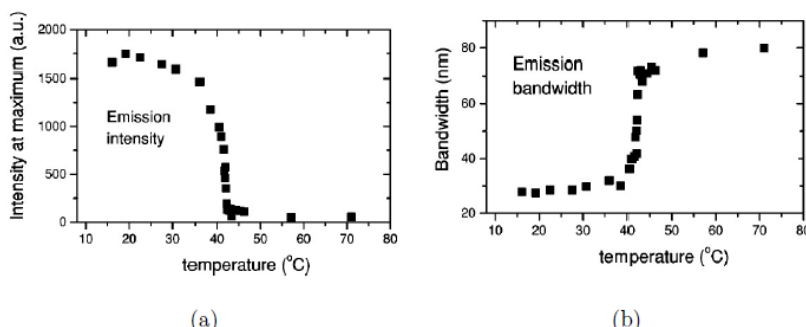
Aynı çalışmada β -faktör %5 olarak hesaplanmıştır ki bu değer geleneksel lazer rezonatörlerine göre oldukça yüksek kabul edilebilir.

2.4. Optimizasyon Özellikleri

Lazerlerin ayarlanabilirliği, kullanıcının çalışma dalga boyunu kontrollü bir şekilde değiştirmesine imkân tanıyan bir cihaz olan ayarlanabilir lazerlerin, spektroskopi, fotokimya ve optik iletişim gibi geniş bir uygulama alanı bulması nedeniyle büyük ilgi görmektedir \cite{duarte1996tunable}. Genel olarak, bir lazerin çalışma dalga boyunun ayarlanması, lazer boşluğunun manipülasyonu ile doğrudan ilişkilidir; bu da boşluktaki uzunlamasına modlar arasında çalışma dalga boyu için bir seçim mekanizması getirir. İlk gösterim, bir boyalı lazeri olarak geliştirilmiş olup, geçtiğimiz on yılda fotonik kristal, dağıtılmış geri besleme gratingli Raman lazer ve mikro disk lazer gibi ayarlanabilir çalışma dalga boyuna sahip çeşitli lazer cihazları bildirilmiştir (Graugnard vd., 2005; Wiersma, 2008). Karmaşık boşluk yapıları, örneğin fotonik kristallerde, rezonans durumlarını oluşturduğu için, yapıların periyodisitesine bağlı olarak kafes sabitliği değiştirilerek ayarlanabilir. Periyodik özelliklerin manipülasyonu, rastgele lazerlerde işe yaramaz, çünkü bu tür lazerlerde periyodik bir yapı yoktur. Bu başlık altında, rastgele lazerlerin ayarlanabilirliği ile ilgili olarak, farklı ve ilginç ayar ilkelerine sahip son dönemde bildirilen bazı çalışmalar ele alınmaktadır.

Daha önce belirtildiği gibi, bir lazerin çalışma dalga boyu üzerinde kontrol sağlamak için, lazer boşluğunun özelliklerini manipüle etmek

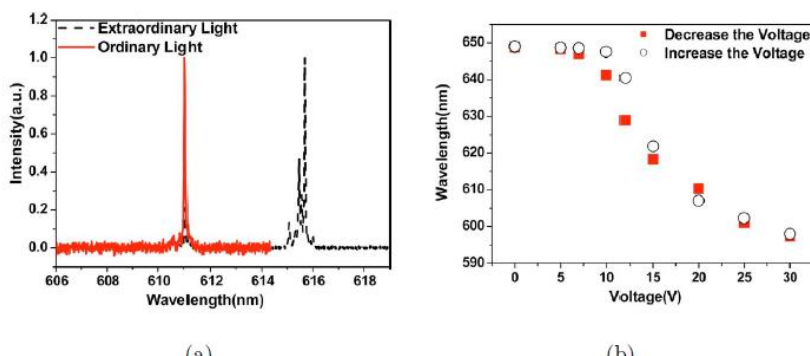
kaçınılmazdır. Wiersma'nın ekibi (Wiersma & Cavalieri, 2002), sinterlenmiş camda yer alan ve cam tozu olarak düşünülebilecek, sıvı kristal (LC) ile doplanmış boyacı içeren bir rastgele lazerde, ısıtılıarak çalışma frekansını ayarlamayı başarmışlardır. Rastgele lazerde, çıkış özelliklerini belirleyen önemli parametrelerden biri, foton difüzyon sabiti ve ortalama serbest yol cinsinden genel olarak ifade edilen saçlığın gücüdür; bu, ardışık iki saçılma olayı arasındaki ortalama mesafedir. LC, farklı sıcaklıklarda farklı kırılma indislerine sahip yarı sıralı fazlara sahip olup, her faz adımında farklı bir kırılma indeksi ortaya çıkar. Bu özellik, ısıtılmadığında gözlemlenirken, ısındığında kaybolur ve izotropik bir yönelim davranışları gelişir. Bu biyo-izotropik özellik, genellikle ışığın polarizasyon yönüne göre farklı bir kırılma indeksi ile kendini gösterir. Wiersma et al., difüzyon sabitini manipüle etmeyi amaçlamışlardır, çünkü sabitin yüksek bir değeri, fotonun, doplanmış LC plakalı sinterlenmiş camdan içeri girdiğinde, verimli bir rastgele lazerleme için yeterince saçılma olayı olmadan ortamdan çıkışacağı anlamına gelir; bu da nispeten uzun bir ortalama serbest yol anlamına gelir. Şekil 2-6'da görüldüğü gibi, sistemin sıcaklığı 10°C ile 70°C arasında değiştirilmiş ve emisyon şiddeti ve bant genişliğinde belirgin değişiklikler gözlemlenmiştir.



Şekil 2-6 sıcaklıkla emisyon şiddeti ve spektrum genişliğinin değişimi (Wiersma & Cavalieri, 2002)

Bir rastgele lazerin emisyon dalga boyunu kontrol etmenin ikinci bir yolu, numuneye elektriksel potansiyel uygulamaktır. Song'un ekibi (Song vd., 2009), Rhodamin B ve rastgele dağıtılmış silika küreler ile doplanmış organik/inorganik bir katman hazırlamış ve bunu, %98'den fazla yansıtıcılığa sahip iki dağıtılmış Bragg yansıtıcı (DBR) katmanı arasına yerleştirmiştirlerdir. Uygulanan gerilim 10 V ile 30 V arasında

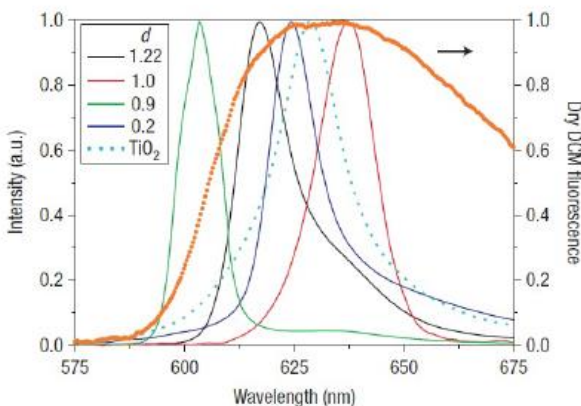
değişmiş ve bu da 648 nm ile 597 nm arasında bir dalga boyu ayar aralığına yol açmıştır. Gerilim uygulanmadığında, LC moleküllerinin yönelimi DBR katmanına paraleldir. Cihazın iki ucu arasında dışarıdan uygulanan potansiyel farkı değiştmeye başladığında, LC moleküllerinin açısal yöneliminin 0 ile 90 derece arasında ayarlanması mümkün olmuştur. Şekil \ref{fig:songselect}'te görüldüğü gibi, daha önce belirtildiği gibi, LC, ışığın kazanç ortamı içindeki polarizasyonuna göre farklı bir davranış sergiler ve lazerleme dalga boyu yaklaşık 50 nm kadar ayarlanabilir ki bu oldukça geniş bir aralıktır.



Şekil 2-7 LC'lin uygulanan voltaj ile çift kırınım özelliğinin değişmesi (Song vd., 2009)

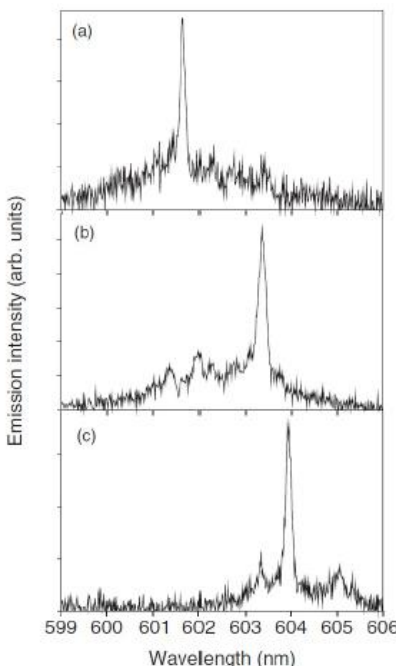
Rastgele lazerin temel prensibi, rastgele dağıtılmış kazanç ortamında güçlü saçılımların meydana gelmesidir. Saçıcıların manipülasyonu ile lazer dalga boyunun ayarlanması, aynı malzeme ile farklı çalışma dalga boylarına sahip rastgele lazer cihazları elde etmek için verimli bir yöntem olabilir (Gaio vd., 2015). Gottardo (Gottardo vd., 2008), fotonik cam formundaki monodispers (tek tip boyutlu) aynı saçıcıları kullanarak dalga boyu seçici bir sistem rapor etmişlerdir. Fotonik cam, cam parçacıklarının birbirine sıkıca bağlandığı yüksek basınç altında şekillendirilmiş bir malzemedendir. Rastgele lazer konfigürasyonu, rastgele dağıtılmış, şekil ve boyutları değişken parçacıklardan oluşan bir ortamda, en az 100 nm l_t olan bir yapıya sahiptir ki bu, olası minimum dalga boyu aralığını temsil eder. Burada ışığın ortam içinde lokalize olduğu düşünülerek, dalga boyuna bağlı kazanç uzunluğu $l_g(\lambda)$ minimum değerini alır. Düşük $l_g(\lambda)$ değeri, keskin bir lazerleme tepe noktası ve yüksek kalite faktörü ile yüksek kazanç sağlandığı için, bu durum geleneksel bir lazerde olduğu gibi gözlemlenir. Ekip aslında, kazanç ortamındaki saçılma

rezonanslarını, saçılma katsayısının boyut bağımlılığı, saçılan işin dalga boyu ve saçıcı boyutları birbirine yakın olduğunda meydana gelen Mie saçılması (Mishchenko vd., 2002) etkisi ile yakalamayı amaçlamışlardır.



Şekil 2-8 fotonik cam malzeme ortamındaki lazerin spektral kayması (Gottardo vd., 2008)

Fotonik camın kullanımının faydalarını göstermek için, hem küresel parçacıklardan oluşan bir boyaya çözeltisi hem de fotonik cam ile iki farklı rastgele ortam hazırlanmış ve her iki örnekte de Mie rezonanslarından faydalanyılmıştır. Parçacık boyutunu değiştirmek gözlemler yapmışlardır. Sıralı çözeltide yaklaşık 10 nm'lik bir dalga boyu kayması gözlemlerken, fotonik cam kullanıldığında 50 nm'lik büyük bir kayma gözlemiştir. Bu fark, Şekil 2-8'de net bir şekilde görülmektedir.



Şekil 2-9 Uyarma alanı değiştirilerek ölçülen lazer emisyon spektrumu: (a) 325 mm, (b) 370 mm ve (c) 410 mm (Yokoyama & Mashiko, 2003)

Rastgele lazer, daha önce belirtildiği gibi, rezonant geri besleme mekanizması ile çalışır ve bu mekanizma, kazanç ortamında ışığın birden çok saçılma olayıyla geri dönmesi sonucu koheren geri besleme olarak açıklanabilir. Eğer ortamda, l_t oldukça kısa olan birden çok saçılma olayı meydana geliyorsa, bu ortamda her biri kendi rezonans frekansına sahip özel birer boşluk (cavity) oluşabilir, dalgaboyu l_t ile karşılaşılabilir boyuttaysa, bu boşluklarda hapsolabilir ve $l \approx \lambda$ durumu olabilir. Yokoyama'nın ekibi (Yokoyama & Mashiko, 2003), bu olasılıkla ilgili farklı boşlukların birbirine yakın yerlerde oluşmasını araştıran bir konfigürasyon kurmuşlardır. Bir lazer boyası ve UV ile kürlenebilen polimer karışımı hazırlamış ve bu karışımı, bir kenarı oldukça ince olan 100 mikron kalınlığında iki mikroskop lامı arasında yerleştirmişlerdir. Bir Nd:YAG lazeri, ince cam taraftan örneğe odaklanmış ve güclü ışınım, cam yüzeyinde bir delik açmıştır; bu süreçte oluşan cam parçacıkları, odak noktasının etrafına dağılmıştır. Polimer ortamındaki cam tozu, lazer örneğinde saçıcı merkezler olarak işlev görür ve bu, rastgele lazer için gerekli bir bileşendir. Ayrıca, örneğin, birden fazla saçılma olayı meydana getirip getirmedini araştırmak amacıyla koheren geri saçılma deneyleri

yapmışlardır. Ölçümler, geri saçılma konisinin $\square 2^\circ$ 'lik bir sivri noktaya sahip olduğunu ve bu durumun koherent geri saçılma için önemli bir olasılığı işaret ettiğini ortaya koymuştur. Kısacası, l_t değerinin dalga boyu ile karşılaşırabilir bir uzunlukta olduğu hesaplanmıştır, yani l_t kısa bir uzunluktadır ve bu da ışığın ortam içinde hapsolmasına yol açar. Şekil 2-9'da görüldüğü gibi, uyarım alanı değiştirilerek, her bir boşluk için özel bir rezonans frekansı aktive edilmiştir. Ayrıca, her uyarım alanı için baskın olan tek bir tepe noktası korunmuş ve ayrı kalmıştır. Bu şekilde, net bir lazer spektrumu ile hassas ayar yapılmıştır.

KAYNAKÇA

- Abrahams, E., Anderson, P., Licciardello, D., & Ramakrishnan, T. (1979). Scaling theory of localization: Absence of quantum diffusion in two dimensions. *Physical Review Letters*, 42(10), 673.
- Anderson, P. W. (1958). Absence of diffusion in certain random lattices. *Physical review*, 109(5), 1492.
- Andreasen, J., Asatryan, A., Botten, L., Byrne, M., Cao, H., Ge, L., Labonté, L., Sebbah, P., Stone, A., Türeci, H., & others. (2011). Modes of random lasers. *Advances in Optics and Photonics*, 3(1), 88-127.
- Cao, H., Zhao, Y., Ho, S., Seelig, E., Wang, Q., & Chang, R. (1999). Random laser action in semiconductor powder. *Physical Review Letters*, 82(11), 2278.
- Cao, H., Zhao, Y., Ong, H., Ho, S., Dai, J. Y., Wu, J. Y., & Chang, R. (1998). Ultraviolet lasing in resonators formed by scattering in semiconductor polycrystalline films. *Applied Physics Letters*, 73(25), 3656-3658.
- Gaio, M., Peruzzo, M., & Sapienza, R. (2015). Tuning random lasing in photonic glasses. *Optics letters*, 40(7), 1611-1614.
- Gottardo, S., Sapienza, R., García, P. D., Blanco, A., Wiersma, D. S., & López, C. (2008). Resonance-driven random lasing. *Nature Photonics*, 2(7), 429.
- Gouédard, C., Husson, D., Sauteret, C., Auzel, F., & Migus, A. (1993). Generation of spatially incoherent short pulses in laser-pumped neodymium stoichiometric crystals and powders. *JOSA B*, 10(12), 2358-2363.
- Graugnard, E., King, J., Jain, S., Summers, C., Zhang-Williams, Y., & Khoo, I. (2005). Electric-field tuning of the Bragg peak in large-pore Ti O₂ inverse shell opals. *Physical Review B*, 72(23), 233105.
- Khajavikhan, M., Simic, A., Katz, M., Lee, J., Slutsky, B., Mizrahi, A., Lomakin, V., & Fainman, Y. (2012). Thresholdless nanoscale coaxial lasers. *Nature*, 482(7384), 204.

- Lagendijk, A., Van Albada, M. P., & van der Mark, M. B. (1987). Localization of light: Quest for the white hole. *International Quantum Electronics Conference*, TUUK1.
- Lawandy, N. M., Balachandran, R., Gomes, A., & Sauvain, E. (1994). Laser action in strongly scattering media. *Nature*, 368(6470), 436.
- Letokhov, V. (1967). Stimulated emission of an ensemble of scattering particles with negative absorption. *ZhETF Pisma Redaktsiiu*, 5, 262.
- Mishchenko, M. I., Travis, L. D., & Lacis, A. A. (2002). *Scattering, absorption, and emission of light by small particles*. Cambridge university press.
- Song, Q., Liu, L., Xu, L., Wu, Y., & Wang, Z. (2009). Electrical tunable random laser emission from a liquid-crystal infiltrated disordered planar microcavity. *Optics letters*, 34(3), 298-300.
- Wiersma, D. S. (2008). The physics and applications of random lasers. *Nature physics*, 4(5), 359.
- Wiersma, D. S., & Cavalieri, S. (2002). Temperature-controlled random laser action in liquid crystal infiltrated systems. *Physical Review E*, 66(5), 056612.
- Wiersma, D. S., van Albada, M. P., Lagendijk, A., & others. (1995). Random laser? *Nature*, 373.
- Yartaşı, E., & Inci, M. N. (2019). A fibre optic wedge type microcavity random laser. *Optik*, 188, 155-161.
<https://doi.org/10.1016/j.ijleo.2019.05.035>
- Yokoyama, S., & Mashiko, S. (2003). Tuning of laser frequency in random media of dye-doped polymer and glass-particle hybrid. *Japanese journal of applied physics*, 42(8A), L970.

RECENT DEVELOPMENTS IN THE APPLICATION AREAS OF LOW TEMPERATURE SUPERCONDUCTOR MgB_2

Özge ERDEM¹

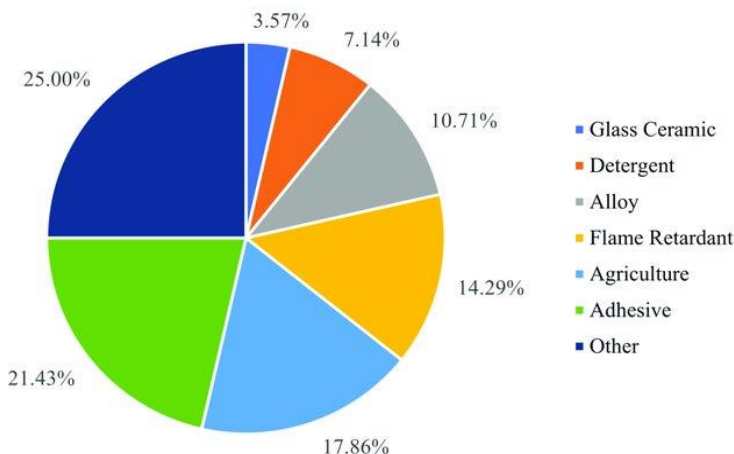
1. INTRODUCTION

The world population and the resulting energy consumption are increasing every year. This leads to the rapid depletion of natural energy resources, increased CO₂ emissions, greenhouse gas effects and climate change. In order to prevent these negativities and to find clean and renewable energy sources for the energy revolution, it has become important. Thus, energy production can be achieved at low cost and energy losses will be minimized. Today, boron mines have a rising strategic importance as an energy source. The use of boron in solar panels (Wang et al., 2021) and lithium-ion batteries (Zhu et al., 2018), which are clean energy sources, increases efficiency. The proportion of boron consumption in various industries is given in Figure 1. Boron (B) mineral has a wide range of uses in medicine (drug production, Boron Neutron Capture Therapy in cancer treatment), cleaning sector (detergent production), glass industry (increasing surface hardness and durability in glass laboratory materials), agriculture (production of artificial fertilizers), metallurgy (melting of copper alloys, increasing the hardness of steel) and nuclear applications. Additionally, boron is used in water purification, in automobiles (airbags, hydraulic brakes, etc.), in the production of air and space vehicles, as missile fuel, in the production of permanent magnets, and in energy storage. According to 2017 data, the three countries with the largest boron reserves in the world are Turkey with 73.4%, Russia with 7.7% and the USA with 6.2% (TENMAK BOREN, n.d.). Considering clean energy sources and energy efficiency, superconductor technology has also become a focus of attention in recent years, along with boron mining. Superconductor materials have an important place in reducing

¹ Assoc. Prof., Bayburt University, Department of Medical Services and Techniques, Vocational High School of Health Services, ozgeerdem@bayburt.edu.tr, ORCID: 0000-0003-4542-941X.

energy losses that are converted into heat and preventing mechanical weathering.

Figure 1. The proportion of boron consumption in various industries



Source: (Liu et al., 2022).

If the resistance of a material becomes zero when the material is cooled below a characteristic temperature (T_c , superconductivity transition temperature/critical temperature), this material is called a superconductor, and this event is called a transition from the normal state to the superconducting state. While the material is in the superconducting state, it expels the magnetic field applied to it (called as Meissner effect) and also conducts the applied DC current without losing energy. Superconducting materials are in their normal state at room temperature and require a cryogenic environment to become superconducting. The branch of science that studies superconductivity at low temperatures is called cryoelectronics. The process of cooling superconducting materials to very low temperatures is done using liquid nitrogen (LN_2 , boiling point: 77 K or -196°C) and liquid helium (LHe , boiling point: 4.2 K or -269°C). Generally, cooling with liquid nitrogen is used for high-temperature superconductors, and cooling using liquid helium is used for low-temperature superconductors.

Superconductors include materials such as chemical elements (such as Pb), alloys (such as NbN), ceramics (such as YBCO), and organic superconductors (such as CNT). For high-temperature superconductors,

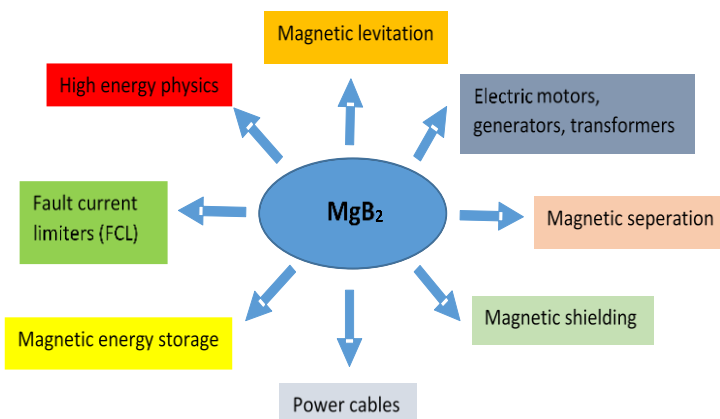
which exhibit superconductivity at temperatures above 77 K and were first discovered in the last quarter of the 20th century (in 1986), superconductivity can be observed at a temperature of 138 K (-135°C) under atmospheric pressure (Dai et al., 1995). This temperature value is the highest T_c value obtained under standard atmospheric pressure. In the studies, high transition temperatures were obtained under high pressure in some superconductors. For example, a 2019 study found T_c to be around 250 K (-23°C) under high pressure of 170 GPa for lanthanum hydride material (Drozdov et al., 2019). But this material is not practically applicable. In a study conducted by a Korean team in 2023 with Cu-doped lead apatite named LK-99, a high T_c value of 370 K was mentioned (Lee et al., 2023). Although researchers have patent applications on this subject, the observations reported in this material were not considered sufficient for superconductivity by experts. Again, a series of studies conducted in 2023 provided significant evidence that the LK-99 material was not a superconductor (Orf, 2023). However, some materials (such as Nb, NbTi, NbZr, NbN, Nb₃Sn, V₃Ga) exhibit superconductivity below 30 K (-243°C) and they are called as low-temperature superconductors (STANFORD Advanced Materials, 2024). For example, T_c for the NbTi alloy used in industrial production of superconducting magnets is about 10 K (Charifoulline, 2006). In 1954, $T_c=18.3$ K was found for the Nb₃Sn intermetallic compound (Matthias et al., 1954). In 1973, $T_c=23.2$ K was observed for the N₃Ge intermetallic compound (WIKIPEDIA The Free Encyclopedia, 2024).

Although there is no superconductor suitable for use at room temperature and cryogenic systems are expensive, superconductors have many applications today. MgB₂ superconductor, which contains boron element (B) (Eremets et al., 2001), which loses its natural resistance to electric current under 250 GP pressure and 11.2 K temperature and becomes a superconductor, is also in an important position with a promising future for technological and industrial applications. In 2001, superconductivity was observed at 39 K in the MgB₂ intermetallic compound (Nagamatsu et al., 2001). This temperature value is the highest T_c value known among metallic superconductors. It should be noted here that MgB₂ is not the first boron-based superconductor. A complex structured boron carbide class with a T_c of 23 K was reported in 1994 (Flükiger, 2016). There are also more than 50 superconducting boride compounds identified in the literature, such as TaB₂ ($T_c=9.5$ K), MoB_{2.5}

($T_c=8.1$ K), ZrB_2 ($T_c=5.5$ K) (Rafieazad et al., 2017). Among all these compounds, MgB_2 stands out with its transition temperature. The T_c value of MgB_2 is almost twice that of Nb_3Ge ($T_c=23.2$ K), which is known to have the highest T_c among all binary superconductors.

Today, MgB_2 superconductor is seen as a rival to high and low temperature superconductors in superconductivity applications due to its many properties. For example, high-temperature superconductors are brittle, whereas MgB_2 superconductor can be produced as wire, strip, ingot and thin film in the desired geometry. MgB_2 is a simple binary compound with high chemical stability. Therefore, it is easy to produce. It has a large coherence length (~7 nm at 0 K and along the boron plane where superconductivity occurs) and a low electromagnetic anisotropy value. Because of this feature, unlike high-temperature superconductors, grain boundaries in MgB_2 do not significantly limit J_c and act as the dominant flux pinning centres (Shimoyama and Motoki, 2024). Its production cost is more affordable than high temperature superconductors. MgB_2 has a density one third of the NbTi alloy used as wire in industry ($\rho = 2.55$ g/cm³). Therefore, it is lighter and suitable for use in large-scale superconductivity applications.

MgB_2 superconductor has potential for use in electric motors, generators, transformers, adiabatic demagnetization refrigerators, low-field and medium-field magnets, magnetic resonance imaging (MRI), magnetic shielding, magnetic sorting, magnetic levitation, magnetic energy storage, RF devices, fault current limiters, and high-energy physics (see Figure 2). A new era of innovation is opening for the energy gap in the world energy sector, with the replacement of low-temperature superconductors cooled with helium, which have high production costs, with new generation MgB_2 -based superconductors, which are in an advantageous position in terms of cost and efficiency. Ongoing scientific studies on this subject aim to optimize the use of MgB_2 in application areas such as energy technologies, engineering, industry and medicine, to discover new application areas and to provide sustainable energy gain. This chapter covers current applications of MgB_2 in superconducting wires, magnets and coils. Other areas of application of MgB_2 will be discussed in future issues of the book.

Figure 2. Potential uses of MgB₂ superconductor

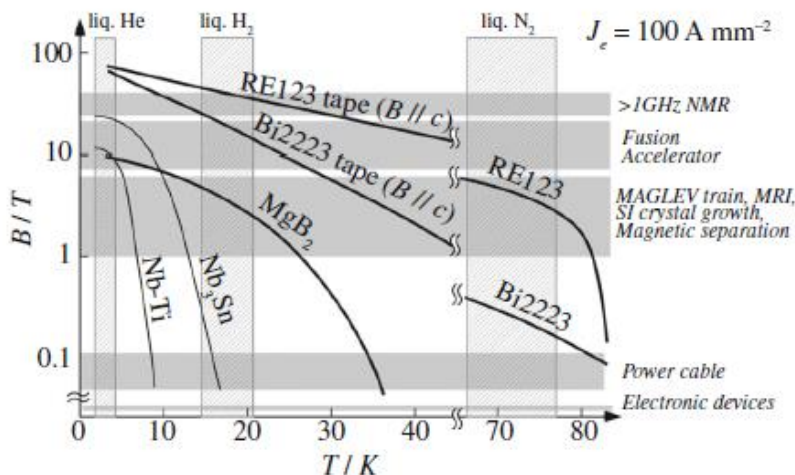
2. MgB₂ WIRE, MAGNET AND COIL APPLICATIONS

Since the discovery of superconductors, superconducting cable applications have continued to increase due to their advantages of high current carrying capacity with a small number of cables and reduced power loss. Until the 1960s, NbTi and Nb₃Sn materials were used to make superconducting wires and superconducting magnets by cooling them to 4.2 K with liquid helium. These wires have a multi-filament structure and are developed on an industrial scale by covering them with copper sheathing for thermal and electrical stabilization (Shimoyama and Motoki, 2024). Generally, the critical current density of NbTi and Nb₃Sn filaments is higher than 1000 A/mm² and due to their critical field values, the applicable magnetic field values at 4.2 K are limited to 9 T and ~23 T, respectively (Shimoyama and Motoki, 2024). Today, these superconducting materials are still used commercially.

With the discovery of high-temperature superconductors, in the late 1990s, Bi2223 superconducting tapes cooled with liquid nitrogen were developed and the first superconducting cable project started in Detroit, USA (Steve et al., 2001). Bi2223 tapes are called “1st generation tapes, 1G” because they pioneered high temperature superconductor applications (Shimoyama and Motoki, 2024). In today's ongoing superconducting cable projects, 1 km long cables are used and the liquid nitrogen temperature is controlled not with a refrigerator, but by heat exchange with unpressurized liquid nitrogen, which has a lower temperature. In the following years, studies on superconducting power cables and superconducting magnets

were also carried out. Nowadays, RE123 tapes have become an important product among high temperature superconductors. Figure 3 shows the applicable conditions of commercial wires and tapes.

Figure 3. Applicable conditions of commercial superconducting wire and tapes. Lines indicate $J_e = 100 \text{ A/mm}^2$ and materials are applicable below these lines (J_e represents the engineering critical current density divided by whole cross section area of tape)

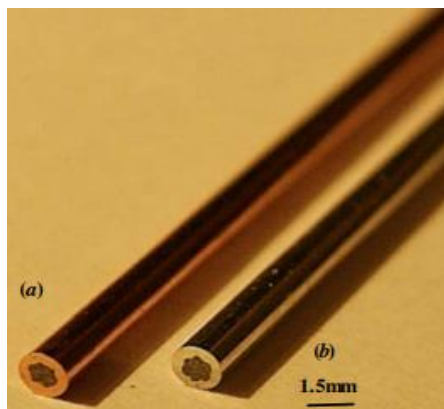


Source: (Shimoyama and Motoki, 2024).

Only 3 years after the discovery of superconductivity in MgB_2 in 2001 (Nagamatsu et al., 2001), as an alternative to the superconductors mentioned above, MgB_2 superconductor wire, coil and magnet began to be produced and used in many applications. One of the most important reasons for this rapid development is that long MgB_2 wires can be produced at affordable prices for various applications without using liquid helium. Major applications of MgB_2 include power cables cooled with liquid hydrogen at 20 K and MRI systems that do not use liquid helium cooled with cryocoolers. High purity polycrystalline MgB_2 exhibits a critical current density of 5000 A/mm^2 at 20 K, regardless of the production method, which is sufficient for power cable applications (Shimoyama and Motoki, 2024). MgB_2 superconductor was first used in the production of superconducting wire by Prof. Bartek Glowacki from Cambridge University (Glowacki et al., 2001). This situation has brought a new perspective to the MgB_2 superconductor, which can be cooled with cheap

and environmentally friendly hydrogen, as a candidate to replace the low-temperature superconductors cooled with liquid helium, which is expensive and whose reserves are increasingly scarce. Strongly grain coupled MgB₂ superconducting filaments can be produced ex-situ or in-situ by the powder-in-tube (PIT) method in a protective gas atmosphere (such as Ar atmosphere) without oxidation, as a single core or multi-filament in a pure copper (Cu) or silver (Ag) tube as shown in Figure 4. It is necessary to coat the MgB₂ superconductor with a metal tube such as Cu or Ag that will not form an insulating oxide barrier at the superconductor interface. This is important both to transfer current to the superconductor and to provide sufficient cryogenic stability (Glowacki et al., 2001). Since the MgB₂ composite wires coated with Cu and Ag tubes produced will be mechanically weak, a material such as stainless steel with high thermal expansion is used to prevent brittleness in the mechanical compression process (Glowacki et al., 2001). Ex-situ Ag/MgB₂ wires and in-situ Cu/Mg+B wires produced by the PIT method, heat treated at 350°C for 48h and 620°C for 48h, respectively, showed magnetic flux densities ($J_{c\text{mag}}$) of 20×10^7 A/m² and 40×10^7 A/m² at 5 K and 0.2 T (Glowacki et al., 2001). Apart from the in-situ and ex-situ PIT methods used in the production of MgB₂ wire, there is also other method called as internal Mg diffusion (IMD) process. In this method, MgB₂ wires are formed as a result of the reaction of Mg in the form of a thin rod and the B powder covering its surroundings at above 800°C (Ye and Kumakura, 2016). From the literature, it can be said that IMD can produce MgB₂ wires with higher J_c values than PIT. In the following years, topics such as the adding/doping effects of carbon nanotubes (CNTs) and nano SiC (Chen et al., 2005) as well as copper and toluene (Wozniak et al., 2012) on MgB₂ wires were investigated. In 2013, Tsinghua University, Cambridge University and MIT designed a cryogenic system using MgB₂ superconductor for DC micro grid applications (Cheadle et al., 2013).

Figure 4. Cross section of the in situ Mg + 2B conductor (a) copper sheath, (b) silver sheath



Source: (Glowacki et al., 2001).

MgB₂ superconducting cables, which have a more affordable production cost than copper cable production, are produced in high quantities and in desired lengths with developing production technologies by many companies such as AGC, Hyper Tech, Hitachi, Sam Dong and EPOCH Wires. MgB₂ wires, which were previously produced with a diameter of 0.5 mm, can now be produced in ultra-thin and more flexible structures with a diameter of 50 µm (Kikuchi et al., 2021).

By using MgB₂ superconductors in wire form, it has become possible to produce wires of desired length and the number of wire joint regions has been reduced. The general features of the MgB₂ wire form include its suitability for operation in high magnetic fields, its operating temperature being between 15 K and 30 K, and its lower operating cost compared to conventional superconducting wires. MgB₂ superconductor wires play a critical role in many magnetic applications. Industrial and engineering applications of MgB₂ superconductor include:

- Medical industry: MRI systems
- Transportation industry: Magnetic levitation (MAGLEV) systems
- Power generation and transmission industry: Generators, transformers, wind turbines, power grids
- High current applications: Superconducting magnets, high current junctions

- High energy physics industry: Nuclear fusion power systems and particle accelerators.

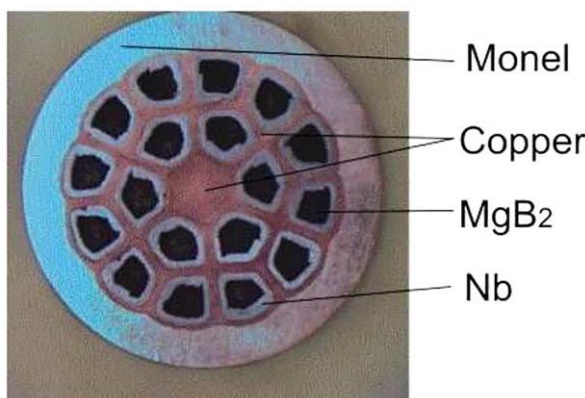
A charged, closed loop of a superconductor, such as an electromagnet, will maintain a current and hence a magnetic field for long periods of time. Superconductors enable the production of high magnetic fields with low power consumption. This property makes superconductors ideal for use in high field magnets. Superconducting magnets with high magnetic field strength are used in MRI to capture detailed images. Superconducting magnets using NbTi wires can produce magnetic fields up to 9 T at 4.2 K, and magnets using Nb₃Sn wires can produce magnetic fields less than 24 T at 4.2 K (Shimoyama and Motoki, 2024). Until the discovery of high-temperature superconductors, the generated magnetic field value was limited by the B_{c2} value of the metallic superconductors. RE123 tapes can be used to generate magnetic fields greater than 30 T as they exhibit strong flux pinning force even at high magnetic fields (Shimoyama and Motoki, 2024). Due to the homogeneous J_c property, polycrystalline MgB₂ bulk superconductors are also candidates for superconducting bulk magnet applications. Since high temperature superconductors are more expensive than low temperature superconductors, hybrid superconducting magnets are used to produce high magnetic fields. For example, the outer part is made of metallic superconducting wires and the inner part is made of copper superconducting tapes (Shimoyama and Motoki, 2024).

Instead of low-temperature superconductors that require the use of expensive liquid helium in MRI devices, the use of MgB₂ coils, which are more suitable for dry operation and can be cooled to the desired operating temperature only with liquid hydrogen or low-cost closed-cycle cryocoolers, reduces the operating costs of MRI systems. Because the life cycle costs of MgB₂ coils are lower due to higher operating temperature and lower cooling cost. Today, the studies in MRI systems are directed towards eliminating liquid cryogen. Considering the temperature tolerance of MgB₂, it is a suitable superconductor for working with cryogenic refrigerators in MRI systems. MgB₂ can replace NbTi in medium magnetic field applications such as MRI systems (EPOCH Wires, n.d.) and allows larger homogeneous magnetic field regions to be obtained (Hyper Tech Research Inc., n.d.). In low magnetic field applications (such as power generation and transmission), MgB₂ is important as it can replace high

temperature superconductors (EPOCH Wires, n.d.). Compared to permanent magnets, magnetic field strengths greater than 0.4 T (up to 1.5-2 T) can be achieved at lower costs by using MgB₂ superconductor (Hyper Tech Research, Inc., n.d.). In 2006, 0.5 T class liquid helium-free MRI systems using MgB₂ wires were developed (Braccini et al., 2007).

An MRI magnet operating in persistent mode using MgB₂ wire requires a permanent and stable current mode with magnetic field stability for high-resolution imaging. One such system consists of a superconducting magnet consisting of multiple coils wound from long MgB₂ wires. Figure 5 shows the multi-filament MgB₂ wire produced by Hyper Tech Research, known as “18+1 Nb/Cu/Monel”, used in the demonstration magnet (DEMO magnet) produced in 2008 for use in the MRI system by cooling it with solid nitrogen (Yao et al., 2008).

Figure 5. Photograph of the cross section of 0.84-mm diameter 18 + 1 multifilament MgB₂ wire, with key components identified

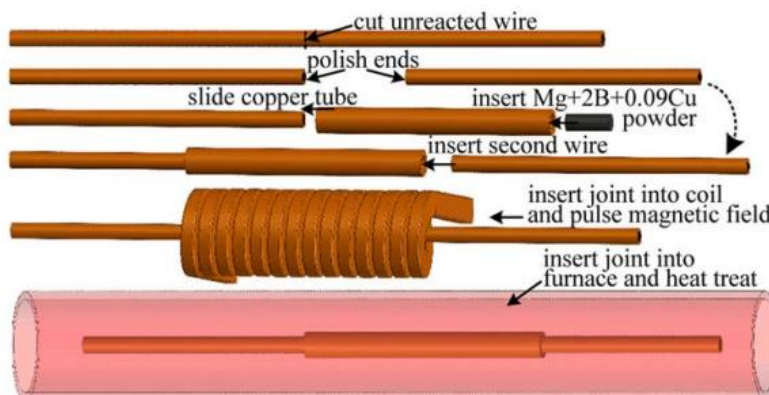


Source: (Tomsic et al., 2007).

To ensure long-term stable magnetic field, the mechanical junctions between MgB₂ wires must be fully superconducting (Yao et al., 2010; Lianga et al., 2023). The total resistance from all joints should not exceed $10^{-10} \Omega$ (Iwasa, 2009). Fortunately, the coherence length of MgB₂ is suitable for fabricating superconducting joints between MgB₂ wires. MgB₂ wire junction studies are still in the research phase. However, for superconducting junction regions, an electrically conductive tube is formed at the wire connections as in Figure 6 and the inside of the tube is filled

with Mg+2B powder. By adding Cu powder to this joint powder, the diffusion between Mg and Cu is minimized (Wozniak et al., 2013). The tube containing the joint powder is compressed into the shape of the joined wires by pulsed magnetic field assisted technique. The current carrying quality of the joint region reached 35% of the transport current value (I_c) of the MgB₂ wire at 4.2 K and 3 T, and 85% at 8 T, according to the study reported in 2013 (Wozniak et al., 2013).

Figure 6. Procedure used for electromagnetically assisted joining of the two segments of the same wire



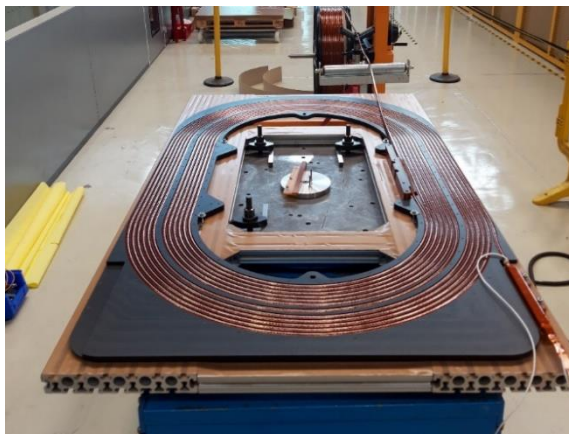
Source: (Wozniak et al., 2013).

MgB₂ coils are used in liquid helium-free MRI systems, reducing system operating costs, and are also used for superconducting power lines and magnet systems in particle accelerators, thus contributing to stability and efficiency in high-temperature operations in these systems.

CERN focuses on MgB₂ coils in various applications such as space exploration and particle physics experiments, such as the European Space Radiation Superconducting Shield (SR2S) project, which aims to develop a superconducting magnet to protect astronauts from cosmic radiation during space missions (Del Rosso, 2015). The use of the MgB₂ superconductor, which can operate at higher temperatures (up to 25 K) than conventional superconductors, could pave the way for innovative shielding technologies against cosmic radiation, a simpler cryogenic system that can reliably manage temperature fluctuations in spacecraft, and long-duration space missions. The superconducting magnets (demonstrator coils) to be used in the SHiP experiment, which aims to detect weakly interacting particles in particle accelerators such as the Large Hadron Collider (LHC)

at CERN, were made using MgB₂ wires (see Figure 7) and successfully tested (Pralavorio, 2024; CERN Courier, 2023). Technical features of MgB₂, such as its high operating temperature, the ability to cool it using gaseous helium instead of superfluid helium, allowing the use of simple cryogenic systems, increasing thermodynamic efficiency, and providing cost efficiency in the production of long superconducting cables, can increase the performance of these magnets in high field applications.

Figure 7. MgB₂ Coil Winding



Source: (CERN Document Server, 2024).

3. CONCLUSIONS

MgB₂ superconductors are preferred over low and high temperature superconductors in many applications today. MgB₂ operates efficiently at high temperatures (up to 39 K), allowing the use of simpler cooling techniques (such as liquid hydrogen or low-cost closed-cycle cryocoolers) than superconductors, which operate at lower temperatures. Given the rarity of helium and the instability of its supply, such superconducting systems that can operate without the need for liquid helium will become more prominent in the future, depending on the equipment and field of application.

MgB₂ shows significant potential in coil applications, especially in MRI technology and particle accelerators, due to its advantageous thermal properties and mechanical stability. MgB₂ magnets play a cost-cutting role for MRI systems operating in persistent mode. Long MgB₂ wires are less costly and simpler to manufacture than high-temperature superconductors. MgB₂ wires and cables have an important place in modern electrical

engineering and medical technology, providing efficient solutions for power transmission, advanced imaging techniques and high-performance superconducting systems. Performance improvement (such as critical current density and mechanical properties of MgB₂ wires) for versatile applications, as well as cost reduction and making the MgB₂ superconductor suitable for a wider range of applications in both industrial and research environments, are important. It is anticipated that the performance of MgB₂ coils will increase with developing production techniques and superconducting junction technologies.

REFERENCES

- Braccini, V., Nardelli, D., Penco, R., & Grasso, G. (2007). Development of ex situ processed MgB₂ wires and their applications to magnets. *Physica C*, 456, 209–217.
- CERN Courier (2023, April 21). *New superconducting technologies for the HL-LHC and beyond*. CERN. <https://cerncourier.com/a/new-superconducting-technologies-for-the-hl-lhc-and-beyond/>
- CERN Document Server (2024, July 11). *Demonstrator coil made of magnesium diboride (MgB₂) superconducting cables (CERN-HOMEWEB-PHO-2024-049-2)*. CERN Accelerating Science. <https://cds.cern.ch/record/2904061>
- Charifoulline, Z. (2006). Residual Resistivity Ratio (RRR) measurements of LHC superconducting NbTi cable strands. *IEEE Transactions on Applied Superconductivity*, 16(2), 1188–1191.
- Cheadle, M. J., Woźniak, M., Bromberg, L., Glowacki, B. A., Jiang, X., Zeng, R., ... & Brisson, J. G. (2013). DC superconducting cable using MgB₂ wires. *IEEE Transactions on Applied Superconductivity*, 23(3), 6200805.
- Chen, S. K., Tan, K. S., Glowacki, B. A., Yeoh, W. K., Soltanian, S., Horvat, J., & Dou, S. X. (2005). Effect of heating rates on superconducting properties of pure MgB₂, carbon nanotube- and nano-SiC-doped in situ MgB₂/Fe wires. *Applied Physics Letters*, 87(18), 182504.
- Dai, P., Chakoumakos, B. C., Sun, G. F., Wong, K. W., Xin, Y., & Lu, D. F. (1995). Synthesis and neutron powder diffraction study of the superconductor HgBa₂Ca₂Cu₃O_{8+δ} by Tl substitution. *Physica C*, 243(3–4), 201–206.
- Del Rosso, A. (2015, August 5). *A superconducting shield for astronauts*. CERN. <https://home.cern/fr/node/4105>
- Drozdov, A. P., Kong, P. P., Minkov, V. S., Besedin, S. P., Kuzovnikov, M. A., Mozaffari, S., ... & Eremets, M. I. (2019). Superconductivity at 250 K in lanthanum hydride under high pressures. *Nature*, 569(7757), 528–531.

- EPOCH Wires (n.d.). *MgB₂ superconductive wires and applications*. Epoch Wires TM. Retrieved September 29, 2024 from <https://www.epochwires.com/mgb2-superconducting-wires>
- Eremets, M. I., Struzhkin, V. V., Mao, H., & Hemley R. J. (2001). Superconductivity in boron. *Science*, 293(5528), 272 – 274.
- Flukiger, R. (Ed.). (2016). MgB₂ superconducting wires: Basics and applications (Vol. 2). *World Scientific*.
- Glowacki, B. A., Majoros, M., Vickers, M., Evetts, J. E., Shi, Y., & McDougall, I. (2001). Superconductivity of powder-in-tube MgB₂ wires. *Superconductor Science and Technology* 14(4), 193.
- Hyper Tech Research Inc. (n.d.). *Wire*. Retrieved September 25, 2024 from <http://www.hypertechresearch.com/wire.htm>
- Iwasa, Y. (2009). Case studies in superconducting magnets: design and operational issues. *Springer science & business media*.
- Kikuchi, A., Iijima, Y., Nimori, S., Yamamoto, M., Kawano, M., Kimura, M., ... & Tsuchiya, K. (2021). Ultra-fine Nb₃Al mono-core wires and cables. *IEEE Transactions on Applied Superconductivity*, 31(5), 1-5.
- Lee, S., Kim, J., Im, S., An, S., Kwon, Y. W., & Auh, K. H. (2023). Consideration for the development of room-temperature ambient-pressure superconductor (LK-99). *Journal of the Korean Crystal Growth and Crystal Technology*, 33(2), 61-70.
- Liang, H., Patel, D., Shahbazi, M., Morawski, A., Gajda, D., Rindfleisch, M., ... & Hossain, M. S. A. (2023). Recent progress in MgB₂ superconducting joint technology. *Journal of Magnesium and Alloys*, 11(7), 2217-2229.
- Liu, X., Xu, C., Chen, P., Li, K., Zhou, Q., Ye, M., ... & Lu, Y. (2022). Advances in technologies for boron removal from water: A comprehensive review. *International Journal of Environmental Research and Public Health*, 19(17), 10671.
- Matthias, B. T., Geballe, T. H., Geller, S., & Corenzwit, E. (1954). Superconductivity of Nb₃Sn. *Phys. Rev.*, 95(6), 1435.

- Nagamatsu, J., Nakagawa, N., Muranaka, T., Zenitani, Y., & Akimitsu, J. (2001). Superconductivity at 39 K in magnesium diboride. *Nature*, 410(6824), 63–4.
- Orf, D. (2023, August 9). *Well, seems like LK-99 isn't a room temperature superconductor after all.* Popular Mechanics. <https://www.popularmechanics.com/science/green-tech/a44764458/lk-99-not-a-superconductor/>
- Pralavorio, C. (2024, July 5). *Less hungry magnets for the experiments of the future.* CERN. <https://home.cern/news/news/engineering/less-hungry-magnets-experiments-future>
- Rafieazad, M., Balci, Ö., Acar, S., & Somer, M. (2017). Review on magnesium diboride (MgB_2) as excellent superconductor: Effects of the production techniques on the superconducting properties. *Journal of Boron*, 2(2), 87 – 96.
- Shimoyama, J., & Motoki, T. (2024). Current status of high temperature superconducting materials and their various applications. *IEEJ Transactions on Electrical and Electronic Engineering*, 19, 292–304.
- Shujun, Y. E., & Kumakura, H. (2016). The development of MgB_2 superconducting wires fabricated with an internal Mg diffusion (IMD) process. *Superconductor Science and Technology*, 29(11), 113004.
- STANFORD Advanced Materials (2024, November 11). *List of low temperature superconducting material.* Oceania International LLC. <https://www.samaterials.com/content/list-of-low-temperature-superconducting-material.html>
- Steve, N., Nassi, M., Bachis, M., Lpdie, P., Kelly, N., & Wakefield, C. (2001). High temperature superconducting cable field demonstration at Detroit Edison. *Physica C*, 354, 49–54.
- TENMAK BOREN (n.d.). *Rezervler.* TENMAK. Retrieved September 22, 2024 from <https://boren.tenmak.gov.tr/tr/calisma-alanlari/rezervler.html>

- Tomsic, M., Rindfleisch, M., Yue, J., McFadden, K., & Phillips, J. (2007). Overview of MgB₂ superconductor applications. *Int. J. Appl. Ceram. Technol.*, 4, 250.
- Wang, Q., Wu, W., Li, Y., Yuan, L., Yang, S., Sun, Y., ... & Ding, J. (2021). Impact of boron doping on electrical performance and efficiency of n-TOPCon solar cell. *Solar Energy*, 227, 273-291.
- WIKIPEDIA The Free Encyclopedia (2024, July 2). *Niobium–germanium*. Wikimedia Foundation, Inc. https://en.wikipedia.org/wiki/Niobium%E2%80%93germanium#cite_note-2
- Wozniak, M., Hopkins, S. C., Gajda, D., & Glowacki, B. A. (2012). Improvement of the critical current of in situ Cu-sheathed MgB₂ wires by copper additions and toluene doping. *Physics Procedia*, 36, 1594-1598.
- Wozniak, M., Glowacki, B. A., Setiadinata, S. B., & Thomas, A. M. (2013). Pulsed magnetic field assisted technique for joining MgB₂ conductors for persistent mode MRI magnets. *IEEE Transactions on Applied Superconductivity*, 23(3), 6200104.
- Yao, W., Bascuñán, J., Kim, W. S., Hahn, S., Lee, H., & Iwasa, Y. (2008). A solid nitrogen cooled MgB₂ “Demonstration” coil for MRI applications. *IEEE Transactions on Applied Superconductivity*, 18(2), 912-915.
- Yao, W., Bascuñán, J., Hahn, S., & Iwasa, Y. (2010). MgB₂ coils for MRI applications. *IEEE Transactions on Applied Superconductivity*, 20(3), 756–759.
- Zhu, Y., Gao, S., & Hosmane, N. S. (2018). Boron-enriched advanced energy materials. *Inorganica Chimica Acta*, 471, 577-586.

Bulk Type Magnetic Field Production Methods and Applications

Murat Abdioglu^{1,2}

Ufuk Kemal Ozturk¹

1. INTRODUCTION

Magnetic fields are at the core of modern technology and play a pivotal role in various industries. From the tiny motors that power our electronic devices to the massive machinery used in manufacturing and healthcare, magnetic fields are integral to the functioning of numerous systems and devices. This chapter aims to explore the diverse methods of producing magnetic fields by bulk-type magnetic field sources and their wide-ranging applications.

Firstly, we will delve into the concept of magnetic moment, a fundamental property of particles that underlies all magnetic phenomena. Understanding magnetic moment is crucial as it forms the basis for the creation and manipulation of magnetic fields. Next, we will discuss the various types of permanent magnets (PMs), their characteristics, and the different methods used in their production. Permanent magnets, such as neodymium, ferrite, and alnico, are essential components in many devices due to their strong and persistent magnetic fields.

We will then focus on bulk superconducting magnets, which are capable of producing extremely high magnetic fields with minimal energy loss. These magnets utilize the principles of superconductivity, a phenomenon observed at very low temperatures, to achieve their remarkable performance. The advantages and challenges associated with high-temperature superconducting magnets (HTS) will be explored.

¹ Electromagnetic Guidance and Acceleration Research Group (EMGA), Department of Physics, Faculty of Science, Karadeniz Technical University, 61080, Trabzon, Türkiye.

² Department of Mathematics and Science Education, Faculty of Education, Bayburt University, 69000, Bayburt, Türkiye.

Finally, we will highlight the diverse application areas for these magnetic field production methods. Permanent magnets find applications in electric motors, generators, sensors, and more, while the bulk superconducting magnets are critical in magnetic bearings, and levitation applications.

This chapter is designed to be a comprehensive resource for both academic researchers and industry professionals. By providing a broad overview of magnetic field production methods and their applications, we aim to enhance your understanding of the innovative developments and technological advancements in this field.

2. MAGNETIC MOMENT

The magnetic moment or magnetic dipole moment is a vector quantity that signifies the magnetic strength and orientation of a magnetic source, such as a magnet or a current loop. It plays a crucial role in determining how an object will interact with an external magnetic field.

In essence, a magnetic moment arises from the motion of electric charges. For instance, in atoms, electrons moving around the nucleus and spinning about their own axes generate magnetic moments. These moments can align in a material, creating a net magnetic moment and thus, making the material magnetic.

The magnetic moment is also crucial in the context of current loops (see Figure 1), where it can be calculated as the product of the current and the area of the loop. This is often represented as $\vec{m} = I\vec{A}$, where I is the current and A is the area of the current loop. As can be seen in Figure 1, the direction of a magnetic moment is easily determined by the right-hand rule.

The physical significance of the magnetic moment is seen in its interaction with magnetic fields. According to (1) it experiences a torque when placed in an external magnetic field, which tends to align the magnetic moment with the field. One can understand that the objects with larger magnetic moments experience larger torques under the same applied magnetic field. This is the principle behind many magnetic devices and applications, from simple compasses to advanced MRI machines. The

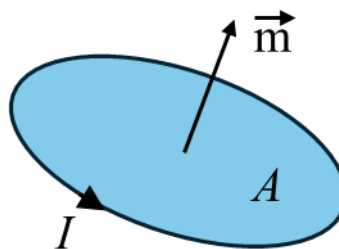


Figure 1. Magnetic moment (\mathbf{m}), created by a current “ I ”, flowing through a loop that encloses an area “ A ”.

strength of a magnetic moment is measured in ampere-square meters ($\text{A} \cdot \text{m}^2$) in the International System of Units (SI). This measurement helps in understanding and comparing the magnetic properties of different materials and devices.

$$\vec{\tau} = \vec{m} \times \vec{B} \quad (1)$$

The magnetic moment is a fundamental property that determines the strength and orientation of a PM's magnetic field. The magnetic moment directly influences the intensity of the magnetic field a PM can generate. A larger magnetic moment corresponds to a stronger magnetic field, which is crucial for applications requiring high magnetic strength, such as in motors, generators, and magnetic resonance imaging (MRI) machines. On the other hand, the magnetic moment defines the orientation of the magnetic field. This is essential for the magnet's interaction with external magnetic fields and other magnetic materials. Proper alignment ensures the magnet functions effectively in its intended application. Since the magnetic moment directly affects the torque, it is important for the stability and performance of rotating machinery and devices that rely on precise magnetic alignment. The magnetic moment is influenced by the material composition and structure of the magnet. Understanding the

magnetic moment helps in designing and selecting materials with optimal properties for specific applications, such as high-temperature resistance or corrosion resistance. Overall, magnetic moment is a fundamental concept in physics and engineering, underlying many technologies that we use daily. Its understanding is essential for developing new magnetic materials and improving existing technologies.

Having explored the concept of magnetic moment, we now delve into the specific types of PMs, followed by an examination of electromagnets and superconducting magnets. Each of these magnetic field sources showcases unique properties and applications, illustrating the diverse ways in which magnetic principles are harnessed in technology and industry. We shall now commence with an exploration of the various forms of PMs.

3. TYPES OF PERMANENT MAGNETS

Permanent magnets are materials that generate a consistent magnetic field without the need for an external power source. They are integral to many modern technologies due to their ability to maintain magnetization over long periods. Here's a detailed look at different types of PMs and their production methods:

i. Neodymium-Iron-Boron ($NdFeB$) Magnets:

Neodymium-iron-boron ($NdFeB$) magnets are the strongest type of PMs available commercially, consisting of neodymium, iron, and boron. They exhibit exceptionally high magnetic properties. $NdFeB$ magnets have the highest magnetic field strength among all permanent magnets, making them ideal for applications requiring powerful magnets. Their maximum energy product ranges from 35 to 52 Mega-Gauss Oersteds (MGoe), indicating the density of magnetic energy and being the highest among permanent magnets.

These magnets tend to lose their magnetic properties at high temperatures, with Curie temperatures between 310 to 400°C. To improve temperature stability and resistance to demagnetization, coatings or additional materials are often used. $NdFeB$ magnets are also prone to corrosion, especially in humid environments, typically coated with protective layers such as nickel, zinc, epoxy, or gold.

The primary method of producing NdFeB magnets involves powder metallurgy, where raw materials are finely ground and pressed into molds to form a dense green compact. This compact is then sintered at high temperatures, causing the particles to bond and form a solid piece, followed by heat treatment to enhance magnetic properties. The final magnet is magnetized by exposing it to a powerful magnetic field. The workflow and main fabrication process of an NdFeB PM are schematically illustrated in Figure 2 and Figure 3, respectively.

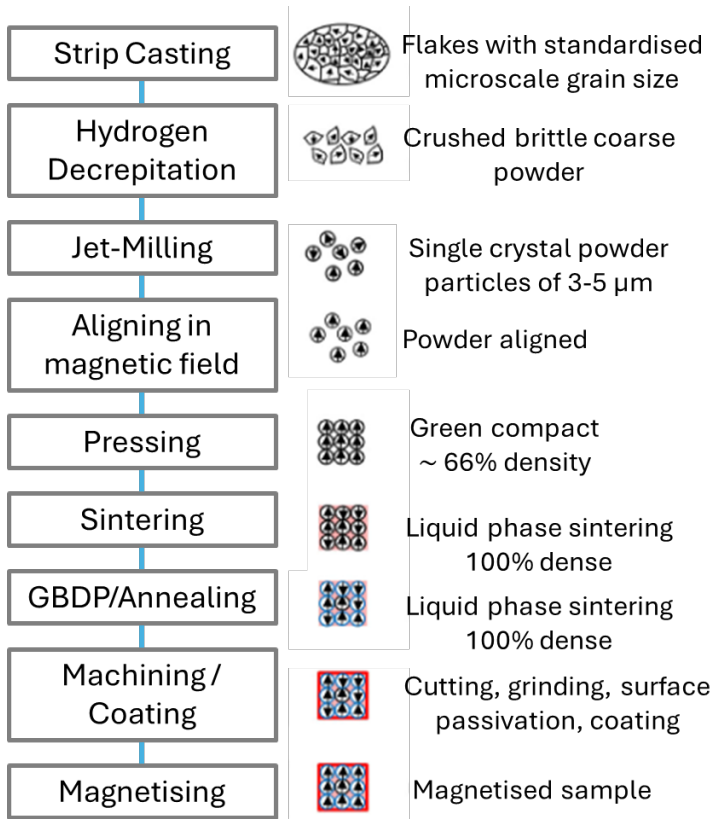


Figure 2. The workflow of an NdFeB PM production [1].

Another production method involves creating bonded magnets, where the magnetic powder is mixed with a polymer binder to form a composite material, which is then pressed or injected into a mould and cured. These bonded magnets have lower magnetic strength but can be made into complex shapes with better mechanical properties. Rapid

solidification involves melt-spinning the alloy to form thin ribbons, which are then crushed into powder and moulded into the desired shape.

NdFeB magnets are essential in designing high-performance electric motors used in hybrid and electric vehicles, drones, and industrial machinery. They are used in hard disk drives to position the read/write heads with high precision, in wind turbine generators to convert wind energy into electrical energy efficiently, in MRI machines and other medical equipment, and in consumer electronics like smartphones, headphones, and loudspeakers for superior performance.

ii. Samarium-Cobalt (SmCo) Magnets:

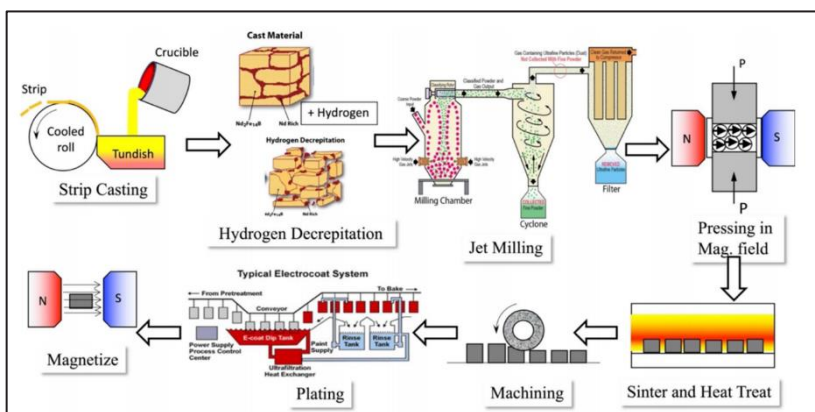


Figure 3. The schematic illustration of the main fabrication process of a NdFeB PM [2].

Samarium-Cobalt (SmCo) magnets are high-performance permanent magnets known for their exceptional strength and durability, particularly in high-temperature environments. Here's a detailed exploration of their characteristics, production methods, and applications:

Samarium-Cobalt magnets are composed primarily of samarium and cobalt, often with other rare-earth elements added to enhance specific properties. They are classified into two main types: SmCo₅ (samarium cobalt 1:5) and Sm₂Co₁₇ (samarium cobalt 2:17). Sm₂Co₁₇ magnets typically offer better magnetic performance and temperature stability compared to SmCo₅ magnets.

One of the defining features of SmCo magnets is their high

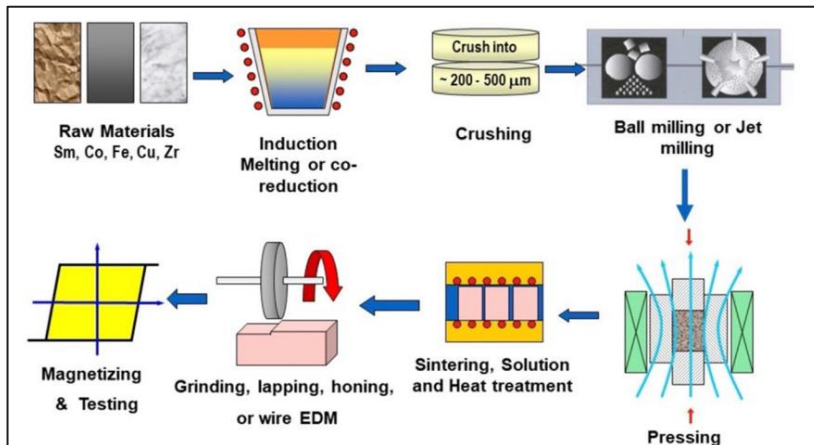


Figure 4. The schematic illustration of the main fabrication process of a SmCo PM [2].

magnetic strength. They possess a strong resistance to demagnetization and maintain their magnetic properties at temperatures up to 300°C (572°F) and even beyond, making them ideal for applications involving high thermal stress. SmCo magnets have a high resistance to corrosion and oxidation, eliminating the need for additional surface treatments or coatings, unlike some other types of permanent magnets.

The main process of SmCo magnet production is illustrated in Figure 4. The overall process involves preparing the alloy, producing the powder, aligning and pressing the particles, sintering and heat treating, machining, and finally, magnetizing it by exposing it to a strong external magnetic field.

Samarium-Cobalt magnets find applications in various demanding environments due to their unique properties. In the aerospace industry, they are used in components that must withstand extreme temperatures and harsh conditions. In the medical field, SmCo magnets are employed in

devices such as magnetic resonance imaging (MRI) machines and surgical instruments, where high performance and reliability are crucial. These magnets are also used in military applications, including precision-guided munitions and other defense technologies.

In the automotive sector, SmCo magnets are utilized in sensors, electric motors, and other components that operate under high thermal conditions. Their stability and strong magnetic properties make them suitable for high-performance motors used in electric vehicles and hybrid cars. Additionally, SmCo magnets are found in various industrial applications, including robotics, instrumentation, and high-temperature actuators.

A comparison between the NdFeB and SmCo magnets is needed in this step. Figure 5 shows the remanent flux density (B_r) in relation to temperature across various magnet materials and grades. In this figure, N42EH and N38AH are NdFeB magnets while R35E and R33E are SmCo

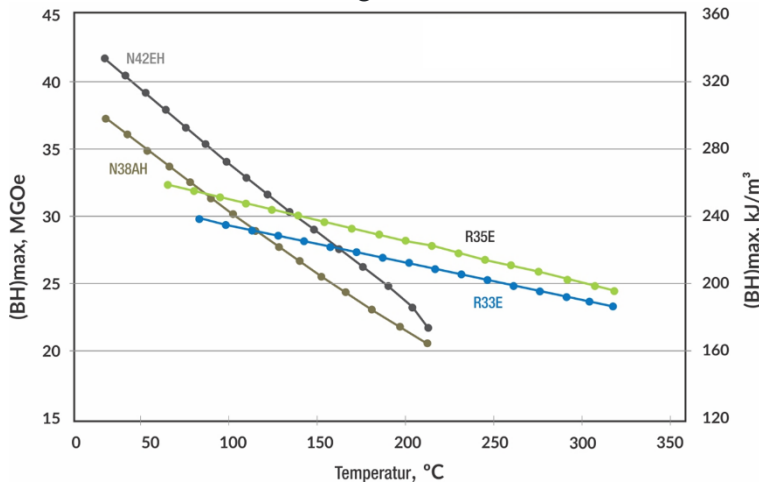


Figure 5. Remanent flux density (B_r) in relation to temperature across various magnet materials and grades [3].

magnets. Choosing between SmCo and NdFeB magnets is frequently driven by temperature considerations. Vehicle drivetrains operating at high temperatures demand magnets that resist demagnetization, typically making SmCo magnets the preferred option. SmCo magnets exhibit significantly lower thermal demagnetization compared to traditional neodymium-based magnets, as evidenced by the reversible temperature coefficient of 0.035%/°C for SmCo versus 0.10%/°C for NdFeB PMs [3].

In summary, Samarium-Cobalt magnets are valued for their exceptional strength, thermal stability, and resistance to demagnetization and corrosion. These properties make them indispensable in numerous high-performance and high-temperature applications across various industries. Advances in production techniques continue to enhance their performance, expanding their use in cutting-edge technologies.

iii. Alnico Magnets (Aluminum, Nickel, and Cobalt):

Alnico magnets are composed primarily of aluminium, nickel, and cobalt, along with iron and small amounts of other elements like copper and titanium. These magnets are renowned for their durability, high magnetic flux density, and resistance to thermal demagnetization, making them one of the oldest and most versatile types of permanent magnets.

Alnico magnets exhibit excellent temperature stability, retaining their magnetic properties over a wide range of temperatures, from -200°C to 550°C . They have a high Curie temperature, meaning they can operate effectively at higher temperatures than many other types of magnets. These magnets possess high residual induction, allowing them to produce strong magnetic fields. However, they have relatively low coercivity, meaning they can be demagnetized by external magnetic fields more easily compared to newer magnet types like NdFeB and SmCo.

The primary methods for producing Alnico magnets are casting and sintering. The casting process involves melting raw materials and pouring the molten metal into molds to form the desired shape. Once solidified, the cast material undergoes heat treatment to optimize its magnetic properties. This method is schematically illustrated in Figure 6 and allows the production of complex shapes and large sizes, making it

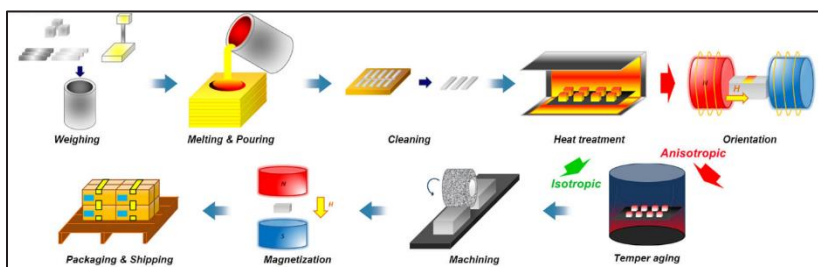


Figure 6. Schematic illustration of the main fabrication process of cast AlNiCo Magnet [4].

suitable for various applications. Sintering, on the other hand, involves grinding raw materials into a fine powder, pressing them into molds, and heating them in a furnace below their melting points. The fabrication process of sintered Alnico magnets is shown in Figure 7. Sintered Alnico magnets are typically more uniform in structure and have slightly different magnetic properties compared to cast Alnico magnets.

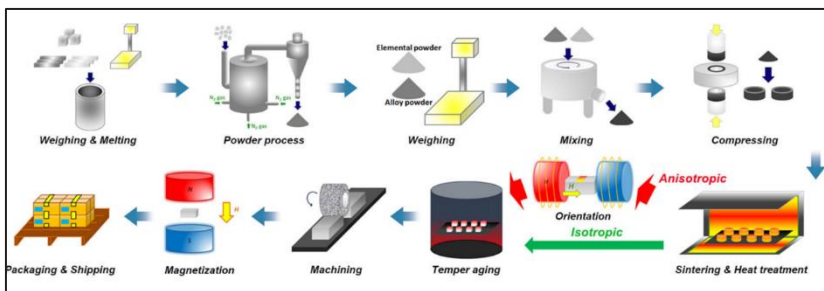


Figure 7. Schematic illustration of the main fabrication process of sintered AlNiCo Magnet [5].

Alnico magnets are used in a wide range of applications due to their unique properties. They are commonly found in electric guitar pickups, where their strong and stable magnetic fields help capture the vibrations of the guitar strings. In sensors and instrumentation, Alnico magnets provide reliable and consistent performance. They are also used in loudspeakers, where their magnetic properties contribute to the quality and efficiency of sound production. Additionally, Alnico magnets are utilized in various industrial applications, such as magnetic separators, clamping devices, and holding magnets.

One of the main advantages of Alnico magnets is their excellent temperature stability, making them suitable for use in high-temperature environments. They are also highly resistant to corrosion, eliminating the need for protective coatings in most applications. However, their relatively low coercivity means that they are more susceptible to demagnetization compared to modern rare-earth magnets like NdFeB and SmCo. This limitation requires careful consideration in applications where exposure to external magnetic fields is likely.

In summary, Alnico magnets are a versatile and durable type of permanent magnet with a long history of use in various applications. Their unique combination of high magnetic flux density, temperature stability, and resistance to corrosion makes them a valuable choice in many industries. Advances in production techniques continue to enhance their performance, ensuring their relevance in today's technological landscape.

iv. Ferrite (Ceramic) Magnets:

Ferrite, or ceramic magnets, are a type of permanent magnet made from iron oxide mixed with other metallic elements. These magnets are known for their affordability, corrosion resistance, and widespread usage in various applications.

Ferrite magnets are composed primarily of iron oxide (Fe_2O_3) combined with barium carbonate (BaCO_3) or strontium carbonate (SrCO_3). These materials are abundant and relatively inexpensive, making ferrite magnets one of the most cost-effective types of permanent magnets available. Ferrite magnets are generally classified into two main types: hard ferrites (permanent magnets) and soft ferrites (used in electromagnetic applications).

One of the key characteristics of ferrite magnets is their high resistance to corrosion. Unlike many other magnetic materials, ferrite magnets do not require protective coatings to prevent rust and degradation. They also exhibit good magnetic properties, though their magnetic strength is generally lower than that of rare-earth magnets like NdFeB or SmCo. Ferrite magnets have a high coercivity, meaning they are resistant to demagnetization, and a relatively high Curie temperature, which allows them to maintain their magnetic properties over a wide range of temperatures.

The primary method for producing ferrite magnets is through a process called sintering. The production process begins with raw materials being finely ground into a powder. This powder is then pressed into molds to form the desired shape. The shaped material, known as a green compact, is subsequently sintered at high temperatures, typically between 1,000°C and 1,300°C. During sintering, the particles bond together, forming a dense and solid structure with strong magnetic properties. The final step involves magnetizing the material by exposing it to a strong magnetic field.

Ferrite magnets find applications in a wide range of industries due to their durability and cost-effectiveness. They are commonly used in consumer electronics, such as speakers, headphones, and microwave ovens, where their magnetic properties contribute to the efficiency and performance of these devices. In the automotive industry, ferrite magnets are used in various components like sensors, motors, and generators. They are also utilized in magnetic separators, holding devices, and in educational and scientific experiments due to their affordability and ease of handling.

One of the main advantages of ferrite magnets is their excellent resistance to corrosion and chemical stability, which makes them suitable for use in harsh environmental conditions. They are also economically advantageous due to the low cost of raw materials and production processes. However, their magnetic strength is lower compared to rare-earth magnets, which limits their use in applications requiring very high magnetic fields.

In summary, ferrite (ceramic) magnets are a versatile and cost-effective type of permanent magnet with a wide range of applications. Their unique combination of corrosion resistance, high coercivity, and affordability makes them a valuable choice in many industries. Despite having lower magnetic strength than some other magnet types, their advantages in durability and cost continue to drive their extensive use in various technological applications.

v. Key Concepts Characterizing Permanent Magnets

Permanent magnets are characterized by several fundamental concepts that define their performance, strength, and applications. Permanent magnets are materials that retain their magnetism without needing an external power source. They generate a consistent magnetic field and interact with other magnetic and non-magnetic materials. This interaction is determined by the magnetic field strength, which indicates the intensity of the magnetic field produced by the magnet. The most common characteristic of a PM is described by the B-H curve, as shown in Figure 8. This curve is also known as the hysteresis loop which demonstrates that a material's response is influenced by its previous state of magnetization. The energy consumed while traversing a hysteresis loop

corresponds to the area enclosed by the loop. The magnetic hysteresis loop illustrates the relationship between magnetic field strength and magnetic flux density. This loop provides insights into the magnet's performance, including its ability to retain magnetism and its resistance to demagnetization over multiple cycles of magnetization and demagnetization.

Let's consider a demagnetized sample with an isotropic distribution of preferred orientations with domination fields having isotropic directions, as shown at point 0 in Figure 8. When we apply an increased magnetic field, H (weak field), in the positive direction, the domains aligned with H grow while the domains anti-aligned with H shrink due to the motion of the domain walls. With further increase of H (moderate field), the magnetic moments in the unaligned domains rotate (or flip) into alignment along preferred axes which are in the general direction of H . When H reaches a sufficiently high level, the magnetic moments along the preferred axes in domains not strictly aligned with H will rotate away from these axes and align with H (point S). At this point, the material reaches the saturation induction B_{\max} [6].

Remanence magnetization (B_r) refers to the residual magnetic moment of a material after an external magnetic field is removed. This value signifies the permanent strength of the magnet and its ability to

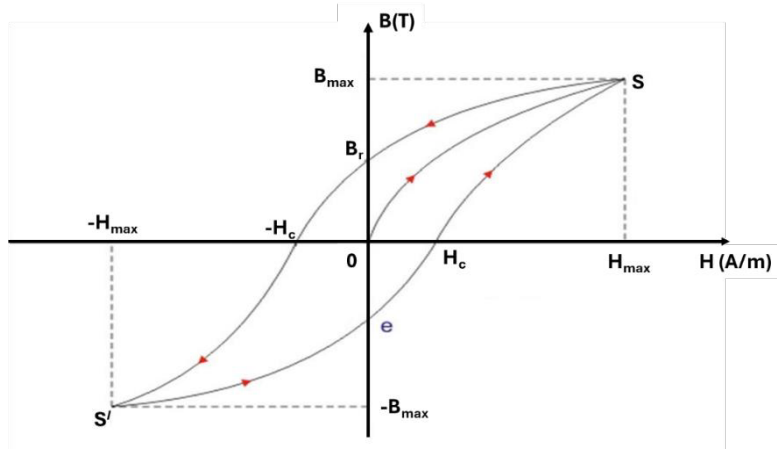


Figure 8. The B-H curve or hysteresis loop of a PM

produce a strong, lasting magnetic field. A high remanence indicates a

magnet that remains highly magnetized even after the external field is no longer present.

Coercivity (H_c) measures a material's resistance to becoming demagnetized by an external magnetic field. Higher coercivity means the magnet is less susceptible to losing its magnetism when exposed to opposing magnetic fields. This property is crucial for maintaining the magnet's performance in environments with varying magnetic influences.

The maximum energy product (BH_{max}) is a measure of the maximum magnetic energy density that can be stored in a unit volume of the magnet. Expressed in Mega-Gauss Oersteds (MGOe), this value indicates the overall strength and efficiency of the magnet. Higher energy products mean that the magnet can produce more powerful magnetic fields in a compact size.

Curie temperature is the temperature at which a magnetic material loses its permanent magnetic properties and transitions to a paramagnetic state. A high Curie temperature allows a magnet to operate effectively at elevated temperatures without losing its magnetism. This property is essential for applications in high-temperature environments.

Anisotropic magnets have optimized magnetic properties in a specific direction, making them stronger and more efficient. This directional alignment enhances their performance in applications requiring precise and strong magnetic fields. In contrast, isotropic magnets possess equal magnetic properties in all directions but generally exhibit lower performance compared to anisotropic magnets.

Understanding these key concepts is crucial for determining the suitable applications and optimal performance of permanent magnets across various industries. Whether for use in electric motors, sensors, medical devices, or consumer electronics, these properties help engineers and designers select the right type of magnet for their specific needs.

4. Bulk Superconducting Magnets

i. Basic Principles of Superconducting Magnets

Superconducting magnets (SMs) rely on the phenomenon of superconductivity, where certain materials exhibit zero DC electrical resistance below a critical temperature (T_c).

Superconductivity is a phenomenon where certain materials exhibit zero electrical resistance when cooled below a critical temperature. This allows them to conduct large currents without energy losses resulting in highly efficient energy transfer and creating exceptionally strong magnetic fields. Additionally, superconductors expel magnetic fields, a property known as the Meissner effect, which enables them to maintain a stable and powerful magnetic field. The key to their operation is maintaining the superconducting material at temperatures below its critical threshold, achieved using cryogenic cooling systems. In addition to the critical temperatures, superconducting materials have two other critical parameters: critical magnetic field and critical current.

The superconductivity is destroyed when the applied current density and applied field exceed the critical values of J_c and H_c , respectively, as shown in Figure 9. Therefore, so as to maintain the

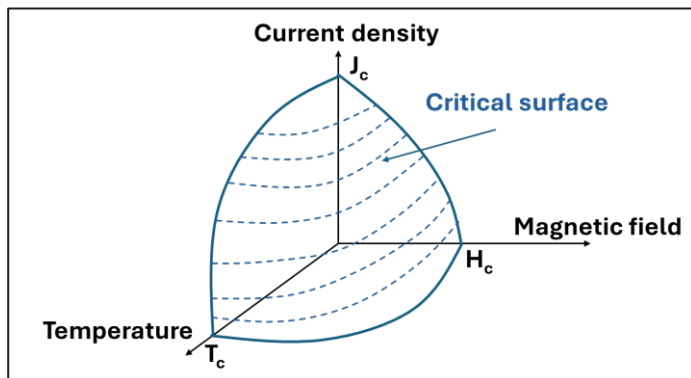


Figure 9. Superconducting state-normal state transition

superconductivity, the material should be in the region surrounded by the critical surface.

ii. High-Temperature Superconducting (HTS) Magnets

HTS magnets can be classified into three main categories based on their structure: bulk, tape, and wire. This chapter focuses on bulk-type HTS magnets.

HTS magnets use materials that become superconducting at higher temperatures, typically above 77 Kelvin (the boiling point of liquid nitrogen). ReBCO (Re: rear earth materials) materials are the most common HTS materials. In this family, bulk yttrium barium copper oxide (YBCO) superconductors have various application areas. The higher operating temperature of HTS magnets simplifies cooling requirements, reducing operational costs and complexity. Figure 10 shows YBCO materials in different geometries and dimensions, fabricated by ATZ GmbH in Germany [7].

iii. Advantages and Challenges of Bulk Superconducting Magnets

Bulk Superconducting magnets offer several advantages but also

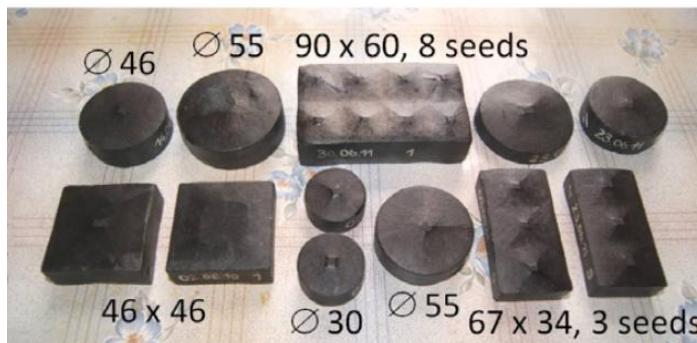


Figure 10. Bulk YBCO HTS materials [7].

present some challenges:

Advantages: Bulk superconducting magnets have a great flux trapping ability of up to 17 T and thus can provide much stronger magnetic fields compared to conventional permanent magnets, making them ideal for applications requiring intense magnetic fields. With zero electrical resistance, superconducting magnets can operate with minimal energy losses, making them highly efficient in all industrial applications. Due to their flux pinning ability, bulk HTS magnets can provide passive levitation which is crucial in Maglev applications.

Challenges: Bulk HTS magnets must be cooled down to their critical temperature and thus need liquid nitrogen to maintain the superconducting state. Maintaining these low temperatures required for superconductivity is a significant challenge. Superconducting materials can be brittle and difficult to work with, posing challenges in manufacturing and maintenance.

5. Applications

In this section, we will give some information about the applications of different magnetic field sources of respectively PMs, EMs and SMs.

i. *Applications of Permanent Magnets*

Permanent magnets are essential in various applications due to their ability to generate a consistent magnetic field without the need for external power. Here are some key areas where permanent magnets are commonly used:

In electronics and electrical devices, PMs help convert electrical signals into sound and vice versa in speakers and microphones. They are used in electric motors and generators to create motion and generate electricity. PMs are integral in various household appliances such as refrigerators, vacuum cleaners, washing machines and dishwashers. Medical devices also use PMs. For example, strong PMs are used in Magnetic Resonance Imaging (MRI) devices to create detailed images of organs and tissues. Hearing aids also use small PMs to convert sound into an electrical signal.

The most common and increasing usage area of the PMs is transportation technology. They are used in the motors [8] that drive electric and hybrid vehicles and provide frictionless support in high-speed rotors and Maglev vehicles. PMs are also used in the energy sector, including wind turbines and magnetic couplings [9].

PMs play a vital role in modern technology and everyday life, offering reliable and efficient solutions across a wide range of applications beyond those mentioned above. Mohapatra et al. reviewed the role of high-performance PMs in different sectors in a topical review paper [10]. The distribution of the consumption % of PMs in different sectors is shown

in Figure 10. As can be seen in this figure, the PMs have a wide range of usage areas. One can say that the most common usage area of the PMs is

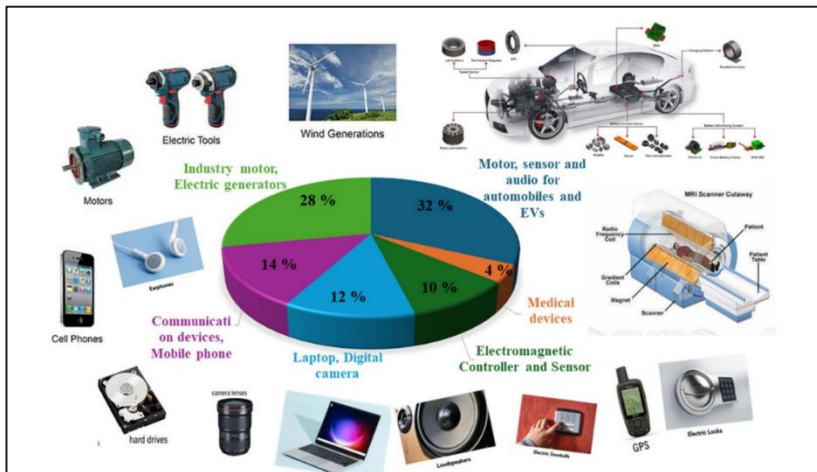


Figure 10. The distribution of the consumption % of PMs in different sectors [10].

motors since the motors are used in electric tools, transportation technology, household appliances, hard drives, MRI machines, etc.

ii. Applications of Bulk Superconducting Magnets

Bulk superconducting magnets are essential in various high-tech and scientific applications due to their ability to provide extremely strong and stable magnetic fields. SMs are used in scientific research on the Maglev trains and their real-scale applications to achieve frictionless travel at high speeds by levitating the train [11-16].

The other most common application area of bulk HTS magnets is magnetic bearings [17-19]. Magnetic bearings incorporating bulk YBCO (Yttrium Barium Copper Oxide) superconductors leverage the unique properties of superconductivity to achieve frictionless, high-efficiency support for rotating machinery. In a magnetic bearing system, bulk YBCO superconductors are used to create powerful and stable magnetic fields that precisely levitate and stabilize the rotor without physical contact. This setup significantly reduces friction and wear, enabling higher rotational speeds, lower energy losses, and reduced maintenance. The real-time control systems in these bearings adjust the magnetic fields to maintain optimal rotor position, enhancing performance and reliability in applications such as high-speed turbines and flywheel energy storage

systems. Bulk YBCO magnetic bearings are crucial for achieving efficient and reliable operation in next-generation machinery.

6. Conclusions

In conclusion, magnetic fields are fundamental to modern technology, with wide-ranging applications spanning various industries. This chapter has provided an in-depth exploration of the diverse methods for producing magnetic fields by bulk magnets and their significance in powering numerous systems and devices.

Understanding the magnetic moment is crucial as it lays the foundation for generating and manipulating magnetic fields. Permanent magnets, with their enduring magnetic properties, are essential in countless devices, offering reliability and strength. Bulk superconducting magnets, despite their cooling requirements, offer unparalleled magnetic field strengths, making them indispensable in advanced scientific research and magnetic levitation applications such as Maglev trains and magnetic bearings.

By covering the fundamental principles and practical uses of magnetic fields, this chapter serves as a comprehensive resource for researchers and professionals. It underscores the ongoing innovations and technological progress in the field of magnetism, pointing to a future where magnetic fields continue to drive development and innovation across multiple domains.

References

- [1] Yang, Y., Walton, A., Sheridan, R., Güth, K., Gauß, R., Gutfleisch, O., ... & Binnemans, K. (2017). REE recovery from end-of-life NdFeB permanent magnet scrap: a critical review. *Journal of Sustainable Metallurgy*, 3, 122-149.
- [2] Cui, J., Ormerod, J., Parker, D., Ott, R., Palasyuk, A., Mccall, S., ... & Lograsso, T. (2022). Manufacturing processes for permanent magnets: Part I—sintering and casting. *Jom*, 74(4), 1279-1295.
- [3] <https://www.arnoldmagnetics.de/blog/neodymium-vs-smco-magnets-for-hybrid-electric-vehicles/>
- [4] <https://www.magnet-sdm.com/cast-alnico-magnet/>
- [5] <https://www.magnet-sdm.com/sintered-alnico-magnet/>
- [6] Furlani, E. P. (2001). Permanent magnet and electromechanical devices: materials, analysis, and applications. Academic press.
- [7] Werfel, F. N., Floegel-Delor, U., Rothfeld, R., Riedel, T., Goebel, B., Wippich, D., & Schirrmeyer, P. (2011). Superconductor bearings, flywheels and transportation. *Superconductor Science and Technology*, 25(1), 014007.
- [8] Bianchi, N., Bolognani, S., & Luise, F. (2004). Potentials and limits of high-speed PM motors. *IEEE Transactions on Industry Applications*, 40(6), 1570-1578.
- [9] Abdallah, M. E., Arafa, O. M., Shaltot, A., & Aziz, G. A. A. (2018). Wind turbine emulation using permanent magnet synchronous motor. *Journal of Electrical Systems and Information Technology*, 5(2), 121-134.
- [10] Mohapatra, P. P., Li, G., Alagarsamy, P., & Xu, X. (2024). Advances in grain-boundary diffusion for high-performance permanent magnets. *Materials Futures*, 3(4).
- [11] Savaskan, B., Guner, S. B., Yamamoto, A., & Ozturk, K. (2020). Trapped magnetic field and levitation force properties of multi-seeded YBCO superconductors with different seed distance. *Journal of Alloys and Compounds*, 829, 154400.
- [12] Abdioglu, M., Guner, S. B., Ozturk, K., Yang, C., Chen, I., & Celik, S. (2022). Magnetic levitation force and trapped field properties of multiseeded YBCO with triangular arrangement of seeds. *International Journal of Applied Ceramic Technology*, 19(1), 459-466.
- [13] Guner, S. B., Celik, S., Cansız, A., & Ozturk, K. (2017). Lateral force measurements for (Gd123) 1-x:(Gd211) x superconductors at different temperatures. *Journal of Superconductivity and Novel Magnetism*, 30, 1335-1343.
- [14] Jiang, S., Deng, Z., Liang, L., Wang, Y., Liu, J., & Zhang, H. (2023). Novel method to detect the speed and position of the HTS Maglev train by using the TMR sensor and the magnet arrays. *Measurement*, 219, 113280.

- [15] Dong, F., Park, D., Huang, Z., Wang, M., & Iwasa, Y. (2024). On the future sustainable ultra-high-speed maglev: A superconductor magnet technology enabling high energy efficiency and robustness. *Energy Conversion and Management*, 314, 118725.
- [16] Abdioglu, M., Ozturk, K., Guner, S. B., Celik, S., & Kucukomeroglu, T. (2019). Investigation of magnetic force properties between different PMGs and multi-seeded YBCO superconductors with different seed distances. *Physica C: Superconductivity and its Applications*, 565, 1353519.
- [17] Sivrioglu, S., Basaran, S., & Yildiz, A. S. (2016). Multisurface HTS-PM levitation for a flywheel system. *IEEE Transactions on Applied Superconductivity*, 26(8), 1-6.
- [18] Yıldız, A. S., & Sivrioglu, S. (2019). Superconducting levitation analysis of a flywheel system using H-formulation. *Physica C: Superconductivity and its Applications*, 561, 64-70.
- [19] Werfel, F. N., Floegel-Delor, U., Riedel, T., Rothfeld, R., Schirrmeister, P., Wippich, D., & Koenig, R. (2014). Technical progress in HTS magnetic bulk application development. *IEEE Transactions on Applied Superconductivity*, 25(3), 1-4.

Coil Type Magnetic Field Production Methods and Applications

Ufuk Kemal Ozturk¹

Murat Abdioglu^{1,2}

1. INTRODUCTION

The importance of magnetic fields spans across numerous scientific and technological applications, from everyday electronic devices to advanced medical imaging and industrial processes. This chapter delves into the various methods of producing magnetic fields using coil-type technologies, highlighting their principles, design considerations, and diverse applications. The aim is to provide a comprehensive understanding of how coil-type magnetic fields are generated, optimized, and applied in different fields.

Magnetic fields are fundamental to the operation of many devices and systems that shape our modern world. From the smallest sensors in mobile devices to large-scale industrial machinery and cutting-edge medical equipment, the ability to generate and manipulate magnetic fields is crucial. The versatility and efficacy of coil-type magnetic field production methods make them an indispensable tool in numerous domains.

The study of magnetic fields and their production methods has a rich history, intertwined with the development of electromagnetism as a key area of physics. Early experiments by pioneers like Faraday and Ampère laid the groundwork for understanding how electric currents can generate magnetic fields. This foundation has led to significant technological advancements, allowing us to harness magnetic fields in increasingly sophisticated ways.

In this chapter, we will first explore conventional electromagnets, which are magnets that generate a magnetic field through the flow of

¹ Electromagnetic Guidance and Acceleration Research Group (EMGA), Department of Physics, Faculty of Science, Karadeniz Technical University, 61080, Trabzon, Türkiye.

² Department of Mathematics and Science Education, Faculty of Education, Bayburt University, 69000, Bayburt, Türkiye.

electric current. Electromagnets are highly versatile and can be switched on and off, making them invaluable in a range of applications from industrial machinery to medical devices. Different types of electromagnets, including direct current (DC) and alternating current (AC) electromagnets, will be covered in detail.

The next focus will be on superconducting magnets, which are capable of producing extremely high magnetic fields with minimal energy loss. These magnets utilize the principles of superconductivity, a phenomenon observed at very low temperatures, to achieve their remarkable performance. The advantages and challenges associated with both high-temperature superconducting magnets (HTS) and low-temperature superconducting magnets (LTS) will be explored.

Finally, we will highlight the diverse application areas for these magnetic field production methods. This chapter is designed to be a comprehensive resource for both academic researchers and industry professionals. By providing a broad overview of magnetic field production methods and their applications, we aim to enhance your understanding of the innovative developments and technological advancements in this field. As we delve into these topics, we will uncover the principles, designs, and practical uses that make coil-type magnetic fields so essential in today's technological landscape.

2. Conventional Electromagnets and Their Types

Conventional electromagnets (EMs) are devices that create a magnetic field through the application of an electric current in a coil of wire. A schematic illustration of a simple electromagnet is shown in Figure 1. The key principle behind electromagnets is that an electric current flowing through a conductor produces a magnetic field around it. This phenomenon was first observed by Hans Christian Ørsted in 1820. When a current passes through a coil of wire, the magnetic fields generated by each turn of the wire combine to create a strong, unified magnetic field along the axis of the coil.

The strength of this magnetic field is directly proportional to the amount of current and the number of turns in the coil. From starting the Biot-Savart law, the magnetic flux density (in Tesla unit) in the centre (B_{core}) of a solenoid-type electromagnet is defined by (1), respectively. Where μ_0 is the permeability of the free space ($4\pi \times 10^{-7}$ H/m), μ_r is the relative permeability, i is the transport current, N and l are the turn number and length of the electromagnet and I is the current flowing through the coil. If the solenoid is long enough, the magnetic flux density at the ends (B_{end}) can be defined by (2).

$$B_{core} = \mu_0 \mu_r \frac{NI}{L} \quad (1)$$

$$B_{end} = \frac{1}{2} \mu_0 \mu_r \frac{NI}{L} \quad (2)$$

The key advantage of electromagnets is their controllability: the magnetic field can be turned on or off and adjusted by varying the current. Conventional electromagnets can be broadly categorized into direct current (DC) electromagnets and alternating current (AC) electromagnets.

i. DC Electromagnets

These electromagnets are powered by a steady direct current, which flows in one direction. As a result, the magnetic field produced is constant and unidirectional. DC electromagnets are commonly used in applications where a stable magnetic field is required, such as in motors, relays, and lifting magnets.

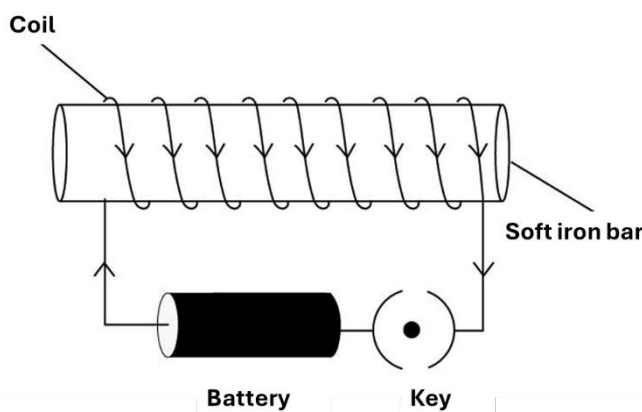


Figure 1. Schematic illustration of a simple electromagnet

ii. AC Electromagnets

In contrast, AC electromagnets are powered by an alternating current, which changes direction periodically. This results in a magnetic field that oscillates in strength and direction. AC electromagnets are used in applications where the magnetic field needs to vary, such as in transformers, inductors, and certain types of motors.

iii. Design and Performance Optimization of Electromagnets

The design of electromagnets involves several key considerations to optimize their performance:

Core Material: The choice of core material significantly impacts the magnetic field strength and efficiency. Soft iron and other ferromagnetic materials are commonly used because of their high magnetic permeability, which allows them to concentrate and enhance the magnetic field produced by the coil. Soft iron is often used due to its high magnetic permeability and low retentivity, which means it can easily gain and lose magnetism.

Coil Design: The number of turns in the wire coil and the current passing through it directly affect the strength of the magnetic field. From (2) and (3), it is easy to conclude that increasing the number of turns or the current will enhance the magnetic field. On the other hand, this will cause an increase in power consumption and potential heating. Therefore, these parameters should be taken into account while designing an electromagnet.

Cooling Systems: Electromagnets can generate significant heat during operation, especially in high-power applications. Effective cooling systems, such as air or liquid cooling, are essential to maintain performance and prevent overheating.

Power Supply: The stability and capacity of the power supply are crucial for the consistent operation of electromagnets. For DC electromagnets, a stable DC power source is needed, while for AC electromagnets, the frequency and voltage of the AC supply must be carefully controlled.

iii. Optimization Techniques

Advanced optimization techniques, including computational modelling and simulation, can be used to fine-tune the design of electromagnets. These techniques help in predicting the performance and

identifying areas for improvement, ensuring that the electromagnets operate efficiently and effectively for their intended applications.

3. Superconducting Magnets

Superconductivity is a phenomenon observed in specific materials where electrical resistance vanishes, and magnetic fields are expelled when cooled below a certain critical temperature. This state allows for the flow of electric current without any energy loss. As different from normal conductors, superconductors exhibit zero electrical resistance against direct current (DC) below a critical temperature, as depicted in Figure 2. This means that an electric current can flow indefinitely without dissipating energy as heat. Superconductors expel magnetic fields from their interior, a phenomenon known as the Meissner effect. This leads to the levitation of magnets above superconductors, showcasing their unique magnetic properties. Superconducting magnets utilizing coils made of High-Temperature Superconducting (HTS) and Low-Temperature Superconducting (LTS) tapes or wires represent significant advancements in the field of magnet technology. HTS tapes, such as those made from Yttrium Barium Copper Oxide (YBCO), and LTS wires, like those made from niobium-titanium (NbTi) and niobium-tin (Nb₃Sn), allow for the production of extremely strong magnetic fields. This section explores the principles, benefits, and applications of superconducting magnets using both HTS tapes and LTS wires.

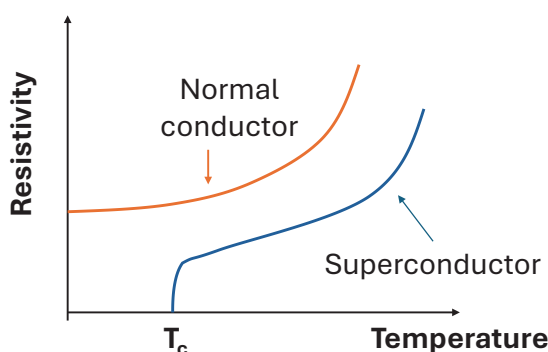


Figure 2. Schematic depiction of resistance as a function of temperature for normal conductors and superconductors.

iv. High-Temperature Superconducting Magnets (HTS) and Low-Temperature Superconducting Magnets (LTS)

Superconducting magnets can be classified into two main categories based on their operating temperatures:

High-Temperature Superconducting Magnets (HTS):

HTS tapes are constructed with materials like YBCO, which become superconducting above 77 Kelvin, the boiling point of liquid nitrogen. This higher operational temperature reduces cooling requirements and costs. HTS tapes typically feature a multi-layer architecture, including a superconducting layer, a stabilizing layer, and a mechanical support substrate. The most common HTS tapes are 2G (second generation) YBCO tapes with different widths from 2 mm to 12 mm. A Schematic illustration of a standard 2G HTS tape fabricated by SuperPower [1] and a photograph of a double pancake coil wound of 2G HTS tape [2] is shown in Figure 3.

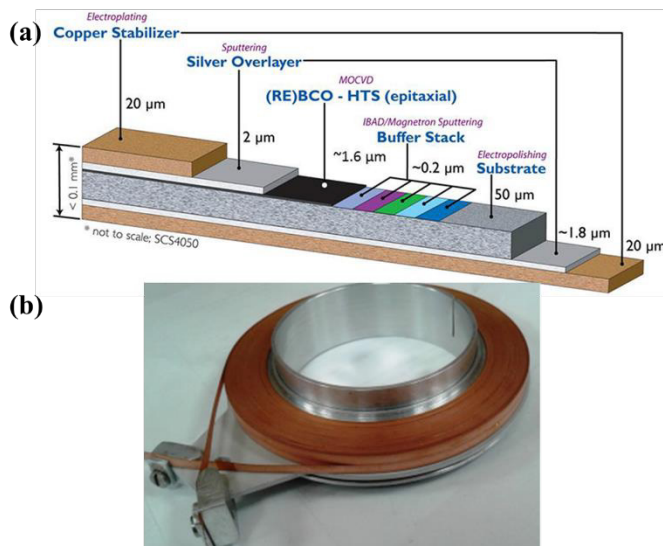


Figure 3. Schematic illustration of a standard 2G HTS tape fabricated by SuperPower [1] and photograph of a double pancake coil wounded of 2G HTS tape [2].

Low-Temperature Superconducting Magnets (LTS):

LTS magnets operate at much lower temperatures, often below 4.2 Kelvin (the boiling point of liquid helium). Common LTS materials include niobium-titanium (NbTi) and niobium-tin (Nb₃Sn). These magnets are widely used in applications where extremely high magnetic fields are necessary, such as in MRI machines and particle accelerators. Figure 4 illustrates the cross-section of the Nb₃Sn [3] and NbTi [4] superconducting cables.

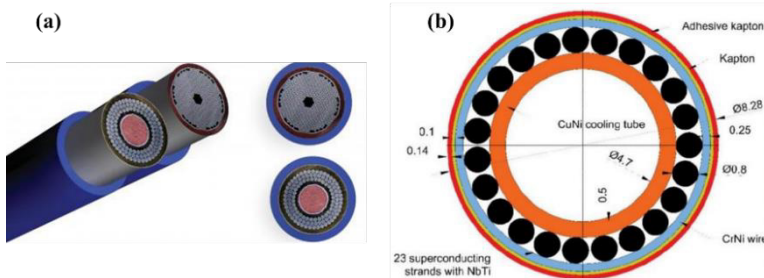


Figure 4. Cross-section of the Nb₃Sn (a) [3] and NbTi (b) [4] superconducting cables.

v. ***Advantages and Challenges of Coil-Type Superconducting Magnets Compared to Conventional Electromagnets***

a) **Advantages**

Higher Magnetic Field Strength: Superconducting magnets can generate much stronger magnetic fields compared to conventional electromagnets. This is crucial for applications that require intense magnetic fields, such as MRI machines and particle accelerators.

Zero Electrical Resistance: Superconductors have zero electrical resistance when operating below their critical temperature. This means they can carry large currents without energy losses, leading to highly efficient magnetic field generation.

Stable Magnetic Fields: Superconducting magnets provide extremely stable and uniform magnetic fields, which is essential for applications requiring precise and consistent magnetic environments, like NMR spectroscopy and certain scientific research experiments.

Energy Efficiency: Due to the lack of electrical resistance, superconducting magnets consume significantly less power during operation compared to conventional electromagnets, especially for maintaining strong magnetic fields over extended periods.

Compact Design: The high current density and efficiency of superconducting materials allow for the design of smaller and lighter magnets that can still produce very powerful magnetic fields. This is beneficial in applications where space and weight are critical factors.

b) Challenges

Cryogenic Cooling Requirements: Superconducting magnets require extremely low temperatures to maintain their superconducting state, typically necessitating the use of cryogenic coolants such as liquid helium or liquid nitrogen. This adds complexity and cost to their design and operation.

Material Challenges: Superconducting materials can be brittle and difficult to work with, posing challenges in manufacturing and maintaining the coils. This can lead to higher production costs and more intricate maintenance procedures.

Quenching: If the superconducting state is disrupted (due to a local increase in temperature, magnetic field, or current), the magnet can suddenly lose its superconductivity and revert to a normal resistive state. This phenomenon, known as quenching, can lead to rapid heating and potential damage to the system.

Fabrication Cost: The fabrication cost of superconducting magnets is higher than that of conventional electromagnets, due to the complexity of materials and the need for specialized cooling systems. This can be a barrier to adoption in cost-sensitive applications.

Operational Complexity: The need for precise temperature control and cryogenic systems makes the operation of superconducting magnets more complex compared to conventional electromagnets. This requires specialized knowledge and infrastructure, which can limit their widespread use.

In summary, while coil-type superconducting magnets offer significant advantages in terms of magnetic field strength, efficiency, and stability, they also present challenges related to cooling requirements, material properties, and operational complexity. These factors must be carefully considered when choosing between superconducting and conventional electromagnets for specific applications.

4. Applications

In this section, we explore the diverse and significant applications of coil-type magnetic field production methods, focusing on conventional electromagnets and superconducting magnets. These technologies are integral to a wide array of fields, from industrial machinery to cutting-edge scientific research.

i. Applications of Electromagnets

Conventional electromagnets are incredibly versatile and are used in various applications across different fields. Here are some key areas where electromagnets are commonly utilized:

Medical Equipment: EMs generate the powerful magnetic fields needed for magnetic resonance imaging in MRI devices. They are used in magnetic therapy devices for pain relief and healing purposes [5].

Industrial Applications: EMs are used in cranes to lift and move heavy metal objects in scrapyards and manufacturing plants. They are used to separate magnetic materials from non-magnetic ones in recycling and mineral processing.

Transportation: Conventional electromagnets are used in Maglev trains, providing the lift and propulsion of the trains, allowing them to travel at high speeds with minimal friction [6]. Electric and hybrid vehicle motors use EMs to drive the wheels [7].

Communication Devices: EMs convert electrical signals into sound and thus are used in speakers and headphones. They are used in the read/write heads for data storage and retrieval in hard drives. Relays and switches use EMs to control circuits and manage signal flow. EMs also have a wide range of usage areas that are not mentioned above, such as home appliances, scientific research, the automotive industry, security systems, etc. These applications illustrate the wide-ranging utility of electromagnets in modern technology and everyday life, making them indispensable components in various devices and systems.

ii. Applications of Superconducting Magnets

Superconducting magnets, particularly those made with HTS tapes and LTS wires, are capable of producing extremely high magnetic fields with minimal energy loss. These magnets are indispensable in various high-tech and scientific applications:

Medical Imaging: Superconducting magnets are crucial in MRI machines, providing the powerful and stable magnetic fields needed to create detailed images of organs and tissues in the body [8].

Particle Physics and Research: Superconducting magnets are used to steer and focus particle beams in facilities like CERN's Large Hadron Collider (LHC), enabling the study of fundamental particles and forces [9]. They are used in experimental fusion reactors, such as tokamaks and stellarators, to confine the plasma needed for nuclear fusion research [10].

Energy Applications: Superconducting magnets are used in superconducting magnetic energy storage systems (SMESS) to store and release large amounts of electrical energy quickly and efficiently [11]. High-performance superconducting magnets are being explored for use in wind turbines to improve efficiency and reduce weight [12].

Transportation: Superconducting magnets are used in scientific research on the Maglev trains and their real-scale applications to achieve frictionless travel at high speeds by levitating and propelling the train [13-14]. The superconducting Maglev in Japan and LTS and HTS magnets used in this vehicle are shown in Figure 5.

Superconducting magnets play a pivotal role in advancing technology and scientific research, offering unparalleled performance in generating and maintaining strong magnetic fields.

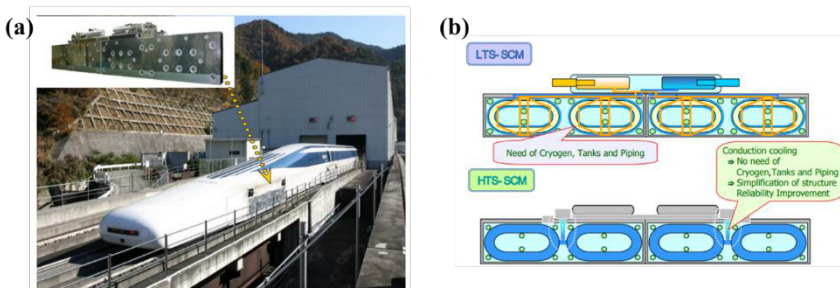


Figure 5. The superconducting Maglev in Japan (a) and LTS and HTS magnets used in this vehicle (b) [14]

5. Conclusions

In conclusion, coil-type magnetic field production methods represent a cornerstone of modern technology, playing an essential role across a wide spectrum of applications. This chapter has provided a comprehensive exploration of the principles, types, and applications of both conventional electromagnets and superconducting magnets, shedding light on their unique advantages and challenges.

Conventional electromagnets are versatile devices that harness the relationship between electricity and magnetism to generate controllable magnetic fields. They are integral to numerous industrial processes, medical devices, transportation systems, and everyday electronic applications. Their ability to be precisely controlled and switched on or off makes them indispensable in both practical and research settings.

Utilizing the remarkable properties of superconductivity, superconducting magnets can generate exceptionally strong and stable magnetic fields with zero electrical resistance. The development of HTS tapes and LTS wires has enabled their use in high-performance applications, such as medical imaging, particle accelerators, energy storage systems, maglev trains, and fusion reactors. Despite the challenges posed by cooling requirements and material properties, the benefits they offer in terms of efficiency and field strength are unparalleled.

The diverse applications of coil-type magnetic field production methods underscore their critical role in advancing technology. From medical imaging and scientific research to industrial processes and energy systems, electromagnets and superconducting magnets are foundational to numerous innovations and improvements in various fields.

By delving into the underlying principles and practical implementations of these technologies, this chapter has aimed to enhance understanding and appreciation of coil-type magnetic field production methods. As research and development continue, the potential for further innovation in this field remains immense, promising significant contributions to science, industry, and everyday life.

In summary, coil-type magnetic field production methods are not only fundamental to current technological advancements but also hold the promise of driving future innovations. Their continued development and

application will undoubtedly play a pivotal role in addressing the challenges and opportunities of tomorrow's technological landscape.

References

- [1] <https://www.superpower-inc.com/Technology.aspx>
- [2] Krasnoperov, E. P., Sychugov, V. V., Guryev, V. V., Shavkin, S. V., Krylov, V. E., & Volkov, P. V. (2020). 2G HTS tape and double pancake coil for cryogen-free superconducting magnet. *Electrical Engineering*, 102, 1769-1774.
- [3] <https://www.supercon-wire.com/content/nb3sn-superconducting-wires>
- [4] Iluk, A. (2021). Investigation of mechanical strains in thermal compensation loop of superconducting NbTi cable during bending and cyclic operation. *Materials*, 14(5), 1097.
- [5] Franz, A. M., Haidegger, T., Birkfellner, W., Cleary, K., Peters, T. M., & Maier-Hein, L. (2014). Electromagnetic tracking in medicine—a review of technology, validation, and applications. *IEEE transactions on medical imaging*, 33(8), 1702-1725.
- [6] Ding, J., Yang, X., & Long, Z. (2019). Structure and control design of levitation electromagnet for electromagnetic suspension medium-speed maglev train. *Journal of Vibration and Control*, 25(6), 1179-1193.
- [7] Chau, K. T., Jiang, C., Han, W., & Lee, C. H. (2017). State-of-the-art electromagnetics research in electric and hybrid vehicles. *Progress in electromagnetics research*, 159, 139-157.
- [8] Manso Jimeno, M., Vaughan, J. T., & Geethanath, S. (2023). Superconducting magnet designs and MRI accessibility: A review. *NMR in Biomedicine*, 36(9), e4921.
- [9] Dam, M., Battiston, R., Burger, W. J., Carpentiero, R., Chesta, E., Iuppa, R., ... & Rossi, L. (2020). Conceptual design of a high temperature superconducting magnet for a particle physics experiment in space. *Superconductor Science and Technology*, 33(4), 044012.
- [10] Bruzzone, P., Fietz, W. H., Minervini, J. V., Novikov, M., Yanagi, N., Zhai, Y., & Zheng, J. (2018). High temperature superconductors for fusion magnets. *Nuclear Fusion*, 58(10), 103001.
- [11] Adetokun, B. B., Oghorada, O., & Abubakar, S. J. A. (2022). Superconducting magnetic energy storage systems: Prospects and challenges for renewable energy applications. *Journal of Energy Storage*, 55, 105663.
- [12] Balachandran, T., Yoon, A., Lee, D., Xiao, J., & Haran, K. S. (2021). Ultrahigh-field, high-efficiency superconducting machines for offshore wind turbines. *IEEE Transactions on Magnetics*, 58(2), 1-5.
- [13] Dong, F., Park, D., Huang, Z., Wang, M., & Iwasa, Y. (2024). On the future sustainable ultra-high-speed maglev: A superconductor magnet technology enabling high energy efficiency and robustness. *Energy Conversion and Management*, 314, 118725.
- [14] Nishikawa, Y., Igarashi, M., & Kusada, S. (2006). Development of New-Type Superconducting Magnets for the Superconducting Maglev.

STEROID İÇEREN BİR BİLEŞİĞİN MOLEKÜLER MODELLEME ÇALIŞMASI

Dr. Öğr. Üyesi Gonca Özdemir Tari¹

1. GİRİŞ

Steroidler, vücutta doğal olarak bulunan veya sentetik olarak üretilen hormon benzeri bileşiklerdir. Önemli biyolojik düzenleyiciler olup vücuttaki inflamasyonu azaltmak, üreme ve cinsiyet özelliklerini belirlemek gibi önemli görevlere sahiptirler. Birbiriyle kaynaşmış dört halkadan oluşmuş karbon iskeletli bir lipit türündür. Şekil 1'de bu çalışmada kullanılan steroid halkanın X-ışınları çözümünden elde edilmiş ortep şekli gösterilmektedir (Marc Uedingen vd., 2001). Çalışmanın temeli ise moleküller yapısı deneySEL olarak karakterize edilmiş steroid bir bileşığın moleküller modelleme teknikleri ile fizikal kimyasal ve elektronik özelliklerini belirleyip. Moleküller yapıya ait etkileşimler ve yük analizleri yapılarak sonuçlar tartışılmıştır.

2. MATERİYAL-METOT

Moleküle ait yapılan optimize çalışmalarının tamamı Gaussian 03W (Frisch ve ark., 2004) programı ile yapılmıştır. Hesaplamlar için B3LYP yöntemi, baz seti seçimi ise 6-31G(d,p) uygun bulunmuştur. Tüm hesaplamlar Gaussian 03W programı kullanılarak YFK'nın karma modeli olan B3LYP yöntemi ile 6-31G(d,p) temel baz seti kullanılarak yapılmıştır. Moleküller yapının görselleştirilmesi, GaussView 4.1 (Dennington, 2007) arayüz programı aracılığıyla gerçekleştirilmiştir. İlk olarak optimizasyon yapılarak molekülün en kararlı hali belirlenmiş ve diğer tüm teorik hesaplamlar belirlenen optimize yapının üzerinden ilerlemiştir. Molekülün HOMO-LUMO enerji diyagramları, sınır orbitalerine bağlı olarak belirlenen kimyasal aktivite parametreleri, Moleküler Elektrostatik Potansiyel (MEP)

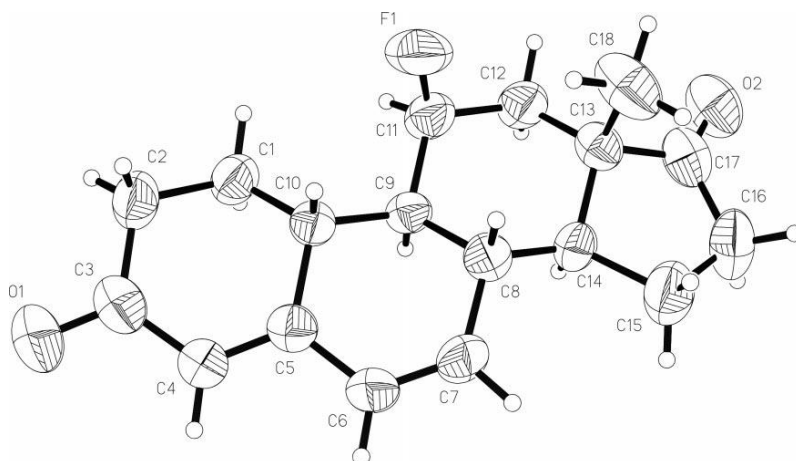
¹ Gonca Özdemir Tari, Ondokuz Mayıs Üniversitesi, Vezirköprü Meslek Yüksekokulu), gozdemir@omu.edu.tr, ORCID: 0000-0001-5919-1778

haritalarına ve yük analizlerine bağlı olarak nükleofilik ve elektrofilik bölgeler belirlenmiştir. İlave olarak moleküle ait optik özellikler (NLO) belirlenmiş ve sonuçlar tartışılmıştır. Bu araştırmalar, hem deneyel çalışmalar desteklemek hem de deneyel yöntemlerle erişilemeyen fizikal ve kimyasal özelliklere ulaşmak amacıyla gerçekleştirilen moleküller modelleme çalışmalarını içermektedir. Özellikle son yıllarda bu tür moleküller modelleme çalışmalarına literatürde oldukça yer verilmiştir. (B. Kosar Kırca vd., 2017; W. Koch, 2001; E. Ermiş, 2018; S.Uzun vd., 2019; A. Eşme, 2014; M.G. Papadopoulos vd., 2006)

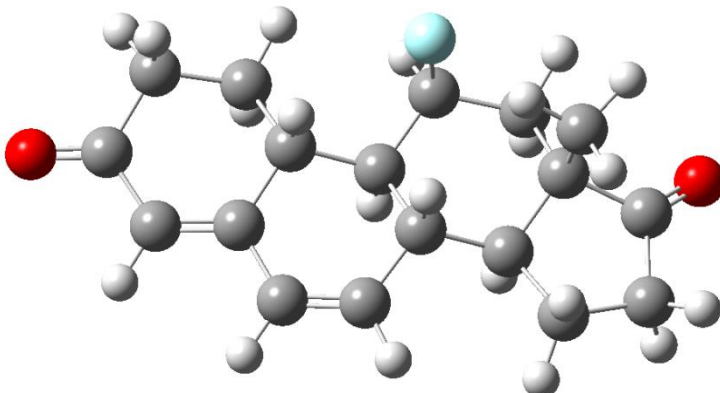
3. BULGULAR VE TARTIŞMA

3.1. Optimize Yapı ve Geometrik Parametreler

Geometrik parametreleri ve moleküller yapısı daha önce Uerdingen tarafından belirlenmiş olan molekülün ortep şekli şekil 1'de verilmektedir. Molekülün minimum enerjili optimize durumuna ise kuantum mekaniksel yöntemlerden YFK/B3LYP hibrit fonksiyoneli ve 6-31G(d,p) temel seti kullanılarak ulaşılmıştır. Molekülün optimize şekli şekil 2'de verilmiştir.



Şekil 1. Moleküle ait X-ışını kırınımından elde edilmiş Ortep görüntüsü (Marc Uedingen vd., 2001).



Şekil 2. Moleküle ait teorik hesaplamalardan elde edilmiş optimize görüntüsü.

Elde edilen sonuçlar ise bağ uzunluğu ve bağ açılarının karşılaştırıldığı tabloda verilmiştir. Tablodaki verilere bakıldığında X-ışını deneysel çalışması (Marc Uedingen vd., 2001) ile teorik hesaplamalardan gelen geometrik parametreler arasında iyi bir uyumun olduğu görülmektedir.

Tablo 1. Moleküle ait bazı deneysel ve kuantum mekaniksel hesaplamalara ait geometrik parametreler.

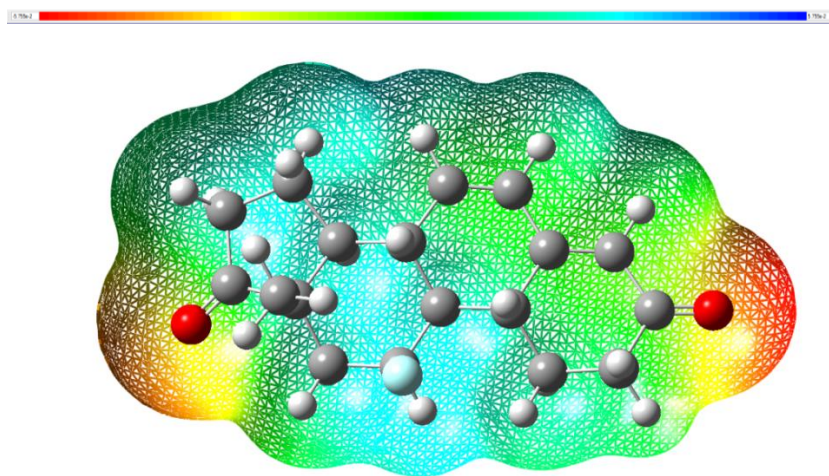
X-ışını Uedingen 2001).	(Marc vd., 2001)	YFK/B3LYP/ 6-31G(d,p)
Bağ uzunluğu		
C1-C2	1.529(4)	1.53192
C1-C10	1.526(5)	1.53693
C3-O1	1.230(4)	1.21849
C5-C6	1.442(5)	1.45669
C9-C10	1.535(4)	1.54763
C11-F1	1.399(4)	1.41914
C11-C12	1.530(4)	1.53273
C14-C15	1.532(6)	1.54148
C13-C17	1.521(5)	1.53278
C17-O2	1.212(4)	1.20462

Bağ açısı

O1-C3-C4	121.4(4)	121.785
O1-C3-C2	120.4(4)	122.108
C2-C1-C10	112.1(3)	111.575
C1-C10-C9	114.9(3)	113.918
C7-C8-C14	114.8(3)	114.310
F1-C11-C9	108.3(3)	108.353
C14-C15-C16	101.7(3)	102.571
C12-C13-C18	112.1(3)	111.214
O2-C17-C16	125.9(4)	125.727
C14-C13-C18	113.3(3)	114.033

3.2. Moleküler Elektrostatik Potansiyel (MEP)

Moleküllerdeki atomlar arası kısmi yük dağılımını incelemek ve bulmak için kullanılan bir yöntemdir. Moleküllerin elektron yoğunluklarının atomlar arası paylaşımını ve dağılımını bir haritalamayla gösterir ve molekülün kimyasal davranışları ve reaktivitesi hakkında çok önemli bilgiler sağlar. Molekülün zayıf hidrojen bağlarından ($\text{C}-\text{H}..\text{O}$) oluştugunu gösteren X-ışını verilerini (Marc Uedingen vd., 2001) ise moleküler elektrostatik potansiyel haritalarına bakarak yorumlayabilmekteyiz. Molekülün hemen hemen tamamında elektron yoğunluğunun düzgün bir dağılıma sahip olduğu gözlenirken, elektrona zengin bölgelerin kırmızı zayıf bölgelerin ise mavi ile gösterilmektedir. Molekülün moleküler elektrostatik potansiyel haritasına bakıldığında elektron yoğunluğunun yüksek olduğu oksijen atomlarının etrafının kırmızı ile renklendirdiğini, elektron yoğunluğunun zayıf olduğu hidrojen atomlarının ise mavi ile kodlandığını görmekteyiz.



Şekil 3. Moleküle ait MEP haritası

3.3. Moleküle Ait Yük Analizi

Moleküllerdeki atomlar arası kısmi yük dağılımını incelemek ve bulmak için kullanılan yöntemlerdir. Moleküllerin elektron yoğunluklarının atomlar arası paylaşımını ve dağılımını bir haritalamayla gösterir. Moleküle ait net yükler Mulliken (R. S. Mulliken, 1955) ve Doğal Yük Analizi (NPA) ile B3LYP yöntemi ile hesaplanmış olup sonuçlar Tablo 2'de verilmiştir.

Tablo 2. Moleküle ait Mulliken ve Doğal popülasyon yük miktarları.

	B3LYP	
	Mulliken	NPA
C1	-0.46461	0.030655
C2	-0.54831	0.038940
C3	0.53579	0.198148
C4	-0.30777	0.006155
C5	0.01858	-0.028516
C6	-0.24951	0.062140

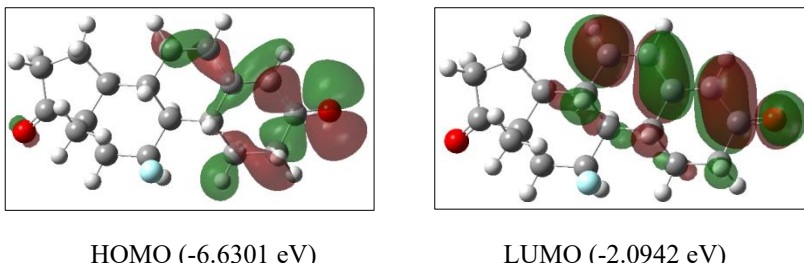
C7	-0.16142	0.038118
C8	-0.28192	0.053549
C9	-0.28106	-0.111232
C10	-0.27794	-0.001976
C11	0.21275	0.329661
C12	-0.49533	0.145948
C13	0.14548	-0.316911
C14	-0.25096	-0.065178
C15	-0.46704	0.070630
C16	-0.56558	0.066019
C17	0.61979	0.261520
C18	-0.69277	0.135547
O1	-0.54775	-0.312077
O2	-0.53724	-0.291410
F1	-0.39840	-0.3097731

Elde edilen sonuçların, MEP haritasındaki verilerle uyumlu olduğu görülmektedir. MEP analiziyle benzer şekilde, en negatif bölgeler yüksek elektronegatifliğe sahip oksijen atomları üzerinde, en pozitif bölgeler ise hidrojen atomları üzerinde yer almaktadır. Moleküllerin Mulliken ve Doğal Yük Analizleri incelendiğinde, her iki yöntemde de elde edilen net yük miktarlarının genel olarak uyumlu olduğu, ancak bazı bölgelerde farklı dağılımlar sergilediği tespit edilmiştir. Bu durumu, atomların elektronegatiflik özelliklerine dayanarak açıklayabiliriz. En negatif yüke sahip atomların, molekülli bir arada tutan hidrojen bağlarının oluşumunda rol oynadığı ve molekül içerisindeki tepkimelerin bu atom ya da atom gruplarının özellikleriyle bağlantılı olduğu sonucuna varılabilir.

3.4. Sınır Orbitalleri

Moleküler orbital tiplerinden HOMO (en yüksek dolu moleküller) ve LUMO (en düşük dolu olmayan orbital) orbitalleri bir moleküler sistemin sınır orbitalleri olarak adlandırılırlar ve moleküler sistemde gerçekleşen tüm tepkimeler bu orbitallerde

gerçekleşir. Moleküle ait bu sınır orbitaleri hesaplanmış olup Şekil 4'de gösterilmektedir. HOMO ve LUMO şekillerine bakıldığından HOMO ve LUMO orbitalerinin O₂'nin bağlı bulunduğu halka üzerinde dağılım gösterdiği görülmektedir.



Şekil 4. Moleküle ait HOMO ve LUMO orbitaleri.

Table 3. Moleküle ait farklı baz setleri kullanılarak hesaplanmış kuantum kimyasal parametreler.

6-311G(d,p)	
İyonizasyon enerjisi, I	6.6301
Elektron ilgisi, A	2.0942
B3LYP Enerji aralığı, ΔE	4.5359
Elektronegatiflik, χ	4.3621
Kimyasal sertlik, η	2.2679
Kimyasal yumuşaklık, S	0.2204
Elektrofilik indeks, ω	-4.1950

$$I = -E_{HOMO}, A = -E_{LUMO}, \Delta E = |E_{HOMO} - E_{LUMO}|, \chi = \frac{I + A}{2}, \eta = \frac{I - A}{2},$$

$$S = \frac{1}{2\eta}, \omega = -\frac{\chi^2}{2\eta},$$

Kimyasal olarak sert atomların, yüksek iyonlaşma enerjisine sahip olmaları ve düşük elektron ilgileri ile karakterize olduğu bilinmektedir. Bir atomun sertlik ya da yumuşaklık durumu, çevresindeki atomlar ve elektronlarla olan etkileşimlerini belirler.

Enerji aralığının küçük olması, atomların daha kolay etkileşim kurmasını sağlarken, yük yoğunluğunun fazla olması kimyasal sertliği, az olması ise kimyasal yumuşaklığını ifade eder. Molekülün geniş bir enerji aralığına sahip olması ise yüksek kimyasal sertlik değeri taşıdığı anlamına gelmektedir. Tablo 3'de ise molekülün sınır orbitalinden türetilmiş nicelikler bulunmaktadır.

3.5. İkinci Dereceden Çizgisel Olmayan Optik Özellikler

Lazer teknolojileri, optik haberleşme, malzeme bilimi gibi birçok alanda son yıllarda oldukça yaygın kullanılan optik özellikler maddenin güçlü elektrik alana maruz kaldığında ortaya çıkmakta olup, ikinci dereceden çizgisel olmayan optik özellikler (NLO) olarak adlandırılmaktadır. Optik özellikler polarize edilebilirlik (α) ile ifade edilirken, doğrusal olmayan optik özellikler hiperpolarizebilite (β) ile tanımlanır. Moleküle ait dipol moment (μ), doğrusal polarize edilebilirlik (α), yönelime bağlı polarize edilebilirlik ($\Delta\alpha$) ve birinci mertebeden polarizebilite (β) değerleri hesaplanmış olup, bu değerler Tablo 3'te sunulmuştur.

Tablo 3. Moleküle ait doğrusal olmayan optik özelliklerin hesaplamaları sonucunda elde edilen parametreler.

Dipol Moment (Debye)	Doğrusal kutuplanabilirlik, Yönelime bağlı kutuplanabilirlik (esu)		1. mertebeden kutuplanabilirlik (esu)	
μ_x	-1.1969131	α_{xx}	276.5355444	β_{xxx}
μ_y	0.7248549	α_{xy}	-8.4094284	β_{xxy}
μ_z	0.211296	α_{xz}	173.9026415	β_{xyy}
μ	1.4151	α_{yy}	-7.1240119	β_{yyy}
		α_{yz}	2.6022665	β_{xxz}
		α_{zz}	126.1437775	β_{xyz}
		α	28.4516	β_{yyz}
		$\Delta\alpha$	173.6817	β_{xzz}
				21.3816214
				-3.3792152,
				20.398757
				-27.6425783
				-31.1625032
				0.906033
				-28.3234177
				β 3.4840x10⁻³⁰

4. SONUÇ-YORUM

Molekülün optimizasyonu sonucunda elde edilen geometrik parametreler, X-ışını kırınım verileriyle karşılaştırılmış ve elde edilen sonuçlar analiz edilmiştir. Bunun yanı sıra, molekülün HOMO-LUMO orbitalleri, MEP haritaları ve yük analizleri gerçekleştirilmiş; bu analizlerin de moleküldeki mevcut etkileşimleri desteklediği tespit edilmiştir. Ayrıca, molekülün doğrusal olmayan optik özelliklerini incelemiştir ve bu sayede deneysel olarak elde edilmesi zor olan fizikal ve kimyasal özelliklerine ulaşılmıştır. Molekülün elde edilmiş olan birinci mertebeden polarizebilite değerleri, gelecekte optik materyal olarak kullanılma potansiyelini göstermektedir.

5. KAYNAKÇA

- Dennington R. II, T. Keith, J. Millam, GaussView, Version 4.1.2, Semichem, Inc., Shawnee Mission, KS, 2007.
- Frisch M. J. et al., Gaussian 03, Revision E.01, Gaussian, Inc., Wallingford CT, 2004.
- Marc Uerdingen, Markus SchuÈrmann, Hans Preut* and Norbert Krause Fachbereich Chemie, Universita Èt Dortmund, Otto-Hahn-StraÙe 6, 44221 Dortmund, Germany. DOI: 101107/S1600536801000484. *Acta Cryst. (2001). E57, o10-o107.*
- B. Kosar Kırca, G. Özdemir Tarı, Ç. Albayrak Kaþtaþ, M. Odabaþoðlu, Orhan Büyükgüngör, Macedonian Journal of Chemistry and Chemical Engineering, Vol 36, No 2 (2017).
- W. Koch, M.C. Holthausen, A Chemist's Guide to Density Functional Theory, second ed., WILEY/VCH Verlag GmbH, Weinheim, 2001.
- E. Ermis, Journal of Mol. Struct. **1156** 91-104 (2018).
- S. Uzun, Z. Esen, E. Koç, N. C. Usta, M. Ceylan, Journal of Mol. Struct. **1178** 450-457 (2019).
- A. Eşme, S. G. Sa˘dinç, Journal of Mol. Struct. **1075** 264-278 (2014). Reactions, (Wiley, London, 1976).
- M.G. Papadopoulos, A.J. Sadlej, J. Leszczynski, Non-linear Optical Properties of Matter Publication Series Challenges and Advances in Computational Chemistry and Physics, vol. 1, Springer, Berlin, Germany, 2006).
- R. S. Mulliken, J. Chem. Phys. **23**, 1883-1840 (1955).

FİZİKTE İLERİ ARAŞTIRMALAR

yaz
yayınları

YAZ Yayınları
M.İhtisas OSB Mah. 4A Cad. No:3/3
İscehisar / AFYONKARAHİSAR
Tel : (0 531) 880 92 99
yazyayinlari@gmail.com • www.yazyayinlari.com